Experimental Studies of Novel Accelerator Structures at 11 GHz and 17 GHz

by

Brian J. Munroe

B.A., Williams College (2007)

Submitted to the Department of Physics
in partial fulfillment of the requirements for the degree of

Doctor of Philosophy in Physics

at the

MASSACHUSETTS INSTITUTE OF TECHNOLOGY

February 2015

Author ..... Signature redacted
Department of Physics
October 31, 2014

Certified by ..... Signature redacted
Richard J. Temkin
Senior Scientist, Department of Physics
Thesis Supervisor

Accepted by ..... Signature redacted
Krishna Rajagopal
Associate Department Head for Education

Experimental Studies of Novel Accelerator Structures at 11 GHz and 17 GHz

by

Brian J. Munroe

Submitted to the Department of Physics
on October 31, 2014, in partial fulfillment of the
requirements for the degree of
Doctor of Philosophy in Physics

Abstract

Photonic band-gap (PBG) structures are promising candidates for electron accelerators capable of high-gradient operation because they have the inherent damping of high order modes required to avoid beam breakup due to instabilities. A key challenge for PBG structures is high-gradient operation without structure damage due to rf-field-induced breakdowns. This thesis reports theoretical results on the design of PBG structures and the generation of wakefields in such structures. It also reports experimental results on PBG structure breakdown testing at high power at both 11 and 17 GHz.

A single-cell photonic band-gap (PBG) structure was designed with an inner row of elliptical rods (PBG-E) to reduce ohmic heating relative to a round-rod structure. The PBG-E structure was built and tested at high power at a 60 Hz repetition rate at X-Band (11.424 GHz) at the SLAC accelerator test stand, achieving a gradient of 128 MV/m at a breakdown probability of 3.6×10^{-3} per pulse per meter at a pulse length of 150 ns. The PBG-E structure showed major improvement in breakdown rate relative to a round-rod PBG structure designed at MIT and previously tested at SLAC.

A test stand was designed and built at MIT for testing single-cell structures at 17.1 GHz, a frequency 50% higher than the SLAC frequency. This test stand provides comparable diagnostics to those used at SLAC, adding optical diagnostic access which can be used for open PBG structures. A conventional disc-loaded waveguide structure, MIT-DLWG, was tested at MIT at up to a 2 Hz repetition rate. This structure reached a maximum gradient of 87 MV/m at a breakdown probability of 1.19×10^{-1} per pulse per meter. A round-rod PBG structure, MIT-PBG-2, has also been tested at MIT at up to a 2 Hz repetition rate and 100 ns pulse length, demonstrating operation up to 89 MV/m at a breakdown probability of 1.09×10^{-1} per pulse per meter.

These test results show that a PBG structure can simultaneously operate at high gradients and low breakdown probability, while also providing wakefield damping. This makes PBG structures viable candidates for future collider applications.

Thesis Supervisor: Richard J. Temkin
Title: Senior Scientist, Department of Physics

Acknowledgments

I would like to thank my advisor, Dr. Richard Temkin, for his help and guidance throughout my career at MIT. Without his support this thesis would not have been possible. I would also like to thank Ivan Mastovsky for keeping everything working in the lab. I have also benefited from the support and assistance from my fellow students past and present; Dr. Roark Marsh and Dr. Emilio Nanni, as well as Elizabeth Kowalski, Jason Hummelt, JieXi Zhang, and Haoran Xu. Our collaborators, Jake Haimson at Haimson Research, Valery Dolgashev, Sami Tantawi, Dian Yeremian, and Lisa Laurent at SLAC, have also provided invaluable advice and expertise throughout my research.

None of this would have been possible without the support of my mother and father throughout my entire academic career. Most importantly of all, I want to thank my wonderful wife Alison, who supported me through late nights, long weekends, and weeks away. And of course Dewey, whose puppy-like enthusiasm reminds us that sometimes we just need to relax and enjoy the simple things.

Contents

1 Introduction **19**

1.1 High-Gradient Accelerators 21

1.1.1 Electric Field 21

1.1.2 Magnetic Field 22

1.1.3 Wakefields 22

1.2 Metamaterials and Photonic Band-gaps 23

1.3 Motivated Research 25

1.4 Outline of Thesis 26

2 Theory **27**

2.1 Accelerator Limits 27

2.1.1 The Kilpatrick Limit and Loew-Wang Scaling 27

2.1.2 Fowler-Nordheim Field Emission and Breakdown 29

2.1.3 Surface Temperature Rise 33

2.1.4 Cyclic Fatigue 36

2.1.5 Pulsed Heating Damage 38

2.1.6 Alternative Theories of Breakdown 39

2.2 Photonic Band Gaps 41

2.2.1 The Band Gap 42

2.2.2 Defect Modes 46

2.2.3 Magnetic Field Enhancement 48

3 Wakefield Simulations **49**

3.1 Wake Potential Theory 49

3.2 Photonic Band-gap Simulation 51

3.3 Dipole Mode Analysis 55

3.4 Comparison of Wake Potential in PBG and DLWG Structures 58

3.5 Multi-Bunch Simulation and Beam Loading Calculation 60

3.6 Conclusion 64

4 Breakdown Structure Design and Modeling **67**

4.1 Overview 67

4.2 Structure Parameters 69

4.3 Structure Modeling 70

4.3.1 High-Gradient Cell Design 71

4.3.2 Periodic Structure 71

4.3.3 Breakdown Test Structure 73

4.4 Modeling for Data Analysis 74

4.4.1 Resonator Fields 74

4.4.2 Pulse Fields 76

4.4.3 Cavity Fields 76

5 Experimental Testing at 11 GHz **79**

5.1 Introduction 79

5.2 Design of Photonic Band-gap (PBG) Structure 80

5.2.1 Structure Tuning 81

5.2.2 PBG Cell Design 84

5.2.3 Design Results 85

5.2.4 HFSS Simulations for Data Analysis 87

5.2.5 Surface Temperature Rise Calculation 88

5.3 Cold Test 89

5.3.1 Bead Pull Measurements 90

5.3.2 Coupling and Q 90
5.4 Experimental Setup 91
5.5 Testing Methodology 92
5.5.1 Experience with First PBG Structure 92
5.5.2 Revised Testing Methodology 95
5.6 Data Analysis 96
5.6.1 Scope Traces 96
5.6.2 Peak Power Meter Traces 99
5.6.3 Combining Results 100
5.7 Experimental Results 102
5.8 Autopsy 106
5.9 Discussion 107

6 Experimental Testing at 17 GHz: Design and Setup 113
6.1 Introduction 113
6.2 Structure Design 114
6.2.1 Common Modifications 114
6.2.2 Design of the Photonic Band-Gap Structure 118
6.3 Design of the Disc-Loaded Waveguide Structure 121
6.4 Cold Test Setup 124
6.5 Experimental Setup 126
6.5.1 Modulator and Klystron 126
6.5.2 Diagnostics 128
6.6 Data Analysis 131
6.7 Sample Traces 132

7 Experimental Testing at 17 GHz: Results 135
7.1 Cold Test Results 135
7.1.1 PBG Structure 136
7.1.2 DLWG Structure 137
7.1.3 Second PBG Structure 140

7.2 First PBG Experimental Results . . . 142
7.2.1 Testing Methodology . . . 142
7.2.2 Optical Diagnostics . . . 143
7.2.3 Testing Summary . . . 144
7.2.4 Phase 1 . . . 145
7.2.5 Phase 2 . . . 147
7.2.6 Phase 3 . . . 148
7.2.7 Comparison with Haimson 17 GHz Accelerator Structure . . . 151
7.2.8 Dark Current . . . 152
7.2.9 Post-Testing Imaging . . . 153
7.3 DLWG Experimental Results . . . 158
7.3.1 Testing Methodology . . . 158
7.3.2 Testing Summary . . . 159
7.3.3 Phase 1 . . . 160
7.3.4 Phase 2 . . . 161
7.3.5 Post-Testing Imaging . . . 165
7.4 Second MIT PBG Structure Experimental Results . . . 165
7.4.1 Testing Methodology . . . 165
7.4.2 Testing Results . . . 168
7.4.3 Post-Testing Imaging . . . 170
7.5 Comparison With SLAC Data . . . 171
7.6 Conclusion . . . 172

8 Discussion and Future Work **175**
8.1 Summary of Results . . . 175
8.2 Discussion of Relevance . . . 177
8.3 Future Work . . . 179
8.3.1 Continued MIT-DLWG Structure Testing . . . 179
8.3.2 Continued MIT-PBG-2 Structure Testing . . . 179

List of Figures

1-1 One, two, and three dimensional photonic band-gap structures 24

2-1 Fundamental unit cell for triangular PBG lattice. 42
2-2 Reciprocal lattice for triangular PBG. 44
2-3 Dispersion for first seven modes in triangular PBG structure. 45
2-4 Band gap map for triangular PBG lattice 46
2-5 Metallic lattice and resulting mode for PBG cavity with $\alpha/\beta = 0.18$. 47

3-1 Schematic of a seven cell PBG structure. 51
3-2 Calculation of longitudinal wake potential and impedance 53
3-3 Calculation of transverse wake potential and impedance 54
3-4 Transverse wake potential as a function of time for each mode in the PBG structure 56
3-5 Comparison of transverse wake potential between DLWG and PBG structures 59
3-6 Comparison of transverse wake potential impedances between PBG and DLWG structures 61

4-1 Section view of TM_{01} mode launcher 68
4-2 Solid model showing a cutaway view of the elliptical PBG structure . 69
4-3 Fixed and tuning parameters for breakdown structure 70
4-4 Sample electric field in the periodic model used for gradient calculation 72
4-5 Difference in the on-axis electric field in the periodic and full breakdown structures 72

4-6 Sample electric field profile in breakdown structure 73
4-7 Cavity response and incident pulse spectrum 75
4-8 Artificial incident power, coupled power, and gradient 77

5-1 Solid model showing a cutaway view of the elliptical PBG structure . 80
5-2 Axisymmetric views of the vacuum space of the PBG-E structure showing the fixed parameters 82
5-3 Rod lattice for elliptical-rod PBG structure 83
5-4 Normalized electric field profile on axis in PBG-E structure 85
5-5 Calculated reflection as a function of frequency for the PBG-E structure. 86
5-6 Electric and magnetic field amplitudes looking at a radial cut of the structure through an inner rod 86
5-7 Electric and magnetic field amplitudes looking at top-down view of the structure 87
5-8 S_{11} of PBG-E structure 90
5-9 π mode field profile 91
5-10 Schematic view of SLAC diagnostics 93
5-11 Calculated peak surface temperature in the PBG-R structure 95
5-12 A sample set of scope traces showing a non-breakdown shot 97
5-13 A sample set of scope traces showing a breakdown shot 98
5-14 Sample traces from the peak power meter for a 150 ns pulse at a gradient of 126 MV/m 99
5-15 Sample traces from the peak power meter for a 150 ns pulse at a gradient of 126 MV/m 100
5-16 Accumulated breakdowns and gradient during the majority of testing. 101
5-17 Calculated peak surface temperature rise due to pulsed heating in the PBG-E structure. 101
5-18 Breakdown probability per pulse per meter of structure vs. gradient at 150 ns pulse length for the PBG-R, PBG-E, and a DLWG structure 102

5-19 Breakdown probability per pulse per meter of structure vs. gradient for PBG-E at pulse lengths of 150 ns and 600 ns. 104
5-20 Breakdown probability vs. peak surface temperature rise for PBG-E at 150 ns and 600 ns 104
5-21 Breakdown probability vs. peak surface temperature rise for PBG-E, PBG-R, and DLWG structures at a pulse length of 150 ns 105
5-22 SEM micrograph of damage on the iris on the input side of the PBG-E cell 107
5-23 SEM micrograph looking directly at high-field side of an inner rod . . 108
5-24 Detail micrograph of the high-field side of the inner rod of the PBG-E 108
5-25 Comparison of inner rods of the PBG-R and PBGE structures 109

6-1 Solid model showing a cutaway view of the 17 GHz PBG structure . . 114
6-2 The MIT PSFC accelerator research lab. Key components relevant to the standing wave structure test are indicated. 115
6-3 Axisymmetric assembly drawing showing fixed 17 GHz structure fixed parameters 117
6-4 Axisymmetric views of the assembly drawing of the 17 GHz PBG structure showing the tuning parameters for the structure. 118
6-5 Calculated reflection as a function of frequency for the 17 GHz PBG structure. 120
6-6 Normalized electric field profile on axis in PBG structure 120
6-7 Electric and magnetic field amplitudes for a radial cut of the PBG structure. 121
6-8 Electric and magnetic field amplitudes for a top-down view of the PBG structure. 122
6-9 Axisymmetric assembly drawing of 17 GHz DLWG structure showing additional fixed parameters and one tuning parameter. 123
6-10 Calculated reflection as a function of frequency for the 17 GHz clamped DLWG structure. 123

6-11 Normalized electric field profile on axis in DLWG structure 124
6-12 Electric and magnetic field amplitudes for a radial cut of the DLWG structure. 125
6-13 Electric and magnetic field amplitudes for a top-down view of the DLWG structure. 125
6-14 Sample traces for klystron voltage, current, and drive. 127
6-15 Sample output power trace for klystron. 128
6-16 Schematic view of MIT standing-wave test stand 129
6-17 Sample diagnostic traces with calculated structure power trace. . . . 133
6-18 Sample diagnostic traces with calculated structure power trace. . . . 133

7-1 Photograph showing the disc-loaded waveguide structure undergoing a bead pull measurement to determine the axial field profile. 136
7-2 S_{11} of PBG structure showing resonance for the π mode. 137
7-3 Comparison of the simulated and measured axial field profiles for the π mode of the PBG structure. 138
7-4 Photograph showing the dielectric perturber in the central PBG cell. 138
7-5 S_{11} of DLWG structure showing resonances for the $\pi/2$ and π modes at increasing frequency. 139
7-6 Comparison of the simulated and measured axial field profiles for the π mode of the DLWG structure. 140
7-7 S_{11} of the MIT-PBG-2 structure showing resonance for the π mode. . 141
7-8 Comparison of the simulated and measured axial field profiles for the π mode of the MIT-PBG-2 structure. 141
7-9 Summarized results showing the gradient and pulse length for the duration of PBG structure testing at MIT. 145
7-10 Breakdown probability as a function of gradient for Phase 1 of MIT-PBG testing. 146
7-11 Breakdown probability as a function of gradient for Phase 3 of MIT-PBG testing. 149

7-12 Breakdown probability as a function of gradient for all 3 phases of MIT-PBG testing. 150
7-13 Breakdown probability as a function of pulsed heating for all 3 phases of MIT-PBG testing. 151
7-14 Dark current versus gradient for MIT-PBG structure. 152
7-15 Optical microscope image showing cavity mating surface. 153
7-16 Photographs showing discoloration of PBG mating iris and fillet to cutoff waveguide. 154
7-17 Optical microscope images of PBG cell showing tool marks and possible breakdown damage. 155
7-18 Optical microscope comparison of an iris of the PBG structure after testing with an untested iris. 155
7-19 A comparison of optical microscope images of one of the high-gradient irises of the 17 GHz PBG and 11 GHz PBG-E structures. 156
7-20 Optical microscope image of high-field side of an inner rod of the MIT-PBG structure. 157
7-21 Optical microscope image of high-field side of an inner rod of the 11 GHz PBG-E structure. 158
7-22 Summarized results showing the gradient for the duration of DLWG structure testing at MIT. 160
7-23 Breakdown probability versus gradient for MIT-DLWG. 162
7-24 Dark current versus gradient for MIT-DLWG structure. 163
7-25 Dark current and gradient versus pulse number for MIT-DLWG structure. 163
7-26 Breakdown probability as a function of gradient for MIT-PBG and MIT-DLWG structures. 164
7-27 Before and after images of DLWG input coupling cell. 166
7-28 Post-testing image of DLWG central cell. 167
7-29 Summarized results showing the gradient, temperature rise, and total number of breakdowns for the MIT-PBG-2 testing. 169
7-30 Breakdown probability versus gradient for MIT-PBG-2. 170

7-31 Breakdown probability as a function of gradient for MIT-PBG, MIT-DLWG, SLAC PBG-R, SLAC PBG-E, and SLAC DLWG structures. 173

List of Tables

2.1 Surface electric fields and gradients predicted from Loew-Wang scaling laws. Gradients are calculated assuming a ratio of $E_{surf}/E_{grad} = 2.5$. 29

2.2 Field emission current as a function of local surface electric field, βE. 31

2.3 Material properties of copper for ohmic heating calculations. 32

2.4 Calculated perturbation height h and field enhancement factor β assuming perturbation melting 33

2.5 Material properties of copper for surface temperature rise calculations. 34

2.6 Mechanical properties of fully-annealed OFHC copper for calculating the yield temperature. 37

3.1 Dimensions of the PBG structure 52

3.2 Comparison of $1/e$ distances calculated from HFSS and CST simulation results. 57

3.3 Dimensions of the DLWG structure 58

5.1 Fixed parameters for PBG-E structure. Final design values for Fig. 5-2 (A). 82

5.2 Tuning parameters for PBG-E structure. Final design values for Fig. 5-2 (B). 83

5.3 Surface field values from HFSS simulations for PBG-E structure, PBG-R structure, and disc-loaded waveguide structure 88

5.4 Calculated peak surface temperature rise for both PBG structures at 100 MV/m accelerating gradient 89

5.5 Q values for the various structure modes 91

6.1 Common fixed parameters for 17 GHz standing-wave structure. Final design values for parameters shown in Fig. 6-3. 117
6.2 Tuning parameters for the 17 GHz PBG structure. Final design values for Fig. 6-4. 119
6.3 The operating parameters of the MIT rf system used for high-gradient structure testing. 126

7.1 Q values for the π mode of the PBG structure. Note that this frequency is measured in air. The resonant frequency in vacuum is 5 MHz higher. 137
7.2 Q values for the π mode of the DLWG structure. Note that this frequency is measured in air. The operational value is 5 MHz higher in frequency. 139
7.3 Q values for the π mode of the MIT-PBG-2 structure. Note that this frequency is measured in air. The resonant frequency in vacuum is 5 MHz higher. 140

Chapter 1

Introduction

Advancement in the study of High Energy Physics (HEP) is, and has historically been, tied to advancement in the study of accelerator physics. As accelerators and the associated technologies such as superconducting magnets have improved, higher energy scales have become available to particle physicists. These higher energies have led to the discovery or confirmation of new particles. The most recent discovery is of a Higgs boson at 125 GeV by the Large Hadron Collider (LHC) [1, 2]. Because the LHC is a hadron collider, detailed study of this particle there is difficult; a more precise study of the particle would be better carried out by a lepton collider.

The options for a lepton collider to study the Higgs boson are limited. To date all lepton colliders have used some combination of electrons and positrons. The energies of circular lepton colliders have been limited by the comparatively large radiation losses of light particles relative to heavy particles such as the protons used at the LHC. The use of the next heavier lepton family, muons, has been considered to reduce the radiation losses in circular lepton colliders, however the short lifetime of muons introduces many other challenges. These radiation losses make linear colliders good candidates for high energy lepton colliders.

The energy achievable in a linear collider is limited by the total length of the collider and the accelerating gradient in the device, i.e. the energy gain per unit length. The limit on the total length of a collider is a practical limit imposed by the realities of building large structures with precise alignment requirements. As such,

it is independent of improvements in accelerator design. Improvements in gradient, however, depend on both the material used for the accelerating structure, i.e. superconducting or normal conducting, and the design of the structure itself. This makes improvements in gradient a key area of accelerator research for HEP applications.

Superconducting technology provides a very low loss option for accelerator structures, reducing the rf power demands for a given gradient. Because superconductors exclude magnetic fields, and sustaining accelerating fields in a structure requires a surface magnetic field, the maximum gradient in a superconducting structure is limited by the critical magnetic field of the superconductor used. Although structure designs can be adjusted to reduce the surface magnetic field for the same gradient, superconducting structures cannot support gradients above approximately 45 MV/m. This makes superconducting structures not an option for future collider designs requiring high gradients over 100 MV/m.

In order to achieve high gradients, future colliders need to look to either normal conducting accelerating structures or novel acceleration techniques. These technologies include plasma wakefield-based or dielectric wakefield acceleration, and offer gradients over 1 GV/m, an order of magnitude or more higher than metallic structures. These advanced technologies are still in development, however, and have not been proven in collider settings. Conventional metallic structures have the advantage of being a mature technology, and ongoing research is focused on achieving higher gradients in metallic structures.

The current gradient limit in metallic structures is the breakdown rate or breakdown probability, which increases with gradient. This is a measure of how likely an accelerator is to have a breakdown, i.e. a vacuum arc. Colliders need low breakdown probability to operate; this can be achieved by operating at a low gradient relative to the maximum value achieved in a structure. The maximum gradient for an accelerator structure is the gradient above which the breakdown probability becomes large enough that the resulting collider operation is unsatisfactory, either due to decreases in luminosity or due to the possibility for damage. Attempts to reach gradients above this level will be limited by breakdowns resulting in a reflection of the incident power.

High-gradient accelerator research focuses, therefore, on increasing the gradient at a given breakdown probability.

1.1 High-Gradient Accelerators

Most conventional metallic accelerating structures are made from oxygen-free high-conductivity (OFHC) copper. This material provides good electrical and thermal conductivity and is relatively easy to machine and join. The material properties of OFHC copper, combined with the design of the accelerating structure, limit the gradient which can be achieved.

1.1.1 Electric Field

Surface electric fields provide the most obvious avenue for limiting gradient via breakdown. Following experiments with DC potentials, sufficiently large surface electric fields can elicit field emission of electrons from the structure walls. At low values this field-emitted current is referred to as dark current; it is present during normal accelerator operation. It is possible, however, for the field-emitted current to become large and trigger a breakdown arc. The surface field at which this breakdown occurs was given in early studies as a frequency-dependent value, scaling either as $\propto f^{1/2}$ [3] or $\propto f^{1/3}$ [4]. In either case increasing the frequency is believed to increase the maximum surface electric field achievable without breakdown, thereby increasing the gradient. Because electric field breakdown is a surface phenomenon and acceleration occurs in the vacuum volume of the structure, the gradient can also be increased by decreasing the ratio of surface electric field to gradient. This ratio is a function of the geometry of the accelerating structure, however values of E_{surf}/E_{grad} below 2 are difficult to achieve.

1.1.2 Magnetic Field

Recent studies have indicated that the surface magnetic field plays an important role in the limitation of gradient through the mechanism of pulsed heating [5]. As the rf fields in the structure drive surface magnetic fields on the structure walls, the associated surface currents ohmically heat a thin layer of copper. This layer of hot copper cools very rapidly as the heat diffuses into the bulk material, resulting in rapid thermal cycling during rf operation. This in turn produces cyclic fatigue in the surface, which ultimately serves to limit the gradient in two ways.

The more conventional limit on gradient due to pulsed heating is the lifetime of the structure subject to cyclic fatigue. Accelerator structures are designed to run for tens of millions of pulses or more without failing. Larger temperature rises and longer pulse lengths increase the fatigue in the copper and decrease the lifetime of the structure [6]. Because gradient correlates with surface magnetic fields, this leads to a limitation on gradient in a given structure provided the requirements for pulse length and operating lifetime of the design.

Pulsed heating can also limit gradient, however, by interacting with the surface electric field and causing breakdown. This phenomenon is less well understood and will be discussed further in Ch. 2, but pulsed heating has been observed to negatively affect breakdown performance [5, 7].

1.1.3 Wakefields

In addition to mitigating breakdowns and cyclic fatigue, high-gradient accelerator structures must also account for the interaction of the charged particles in the structure. This interaction is caused by the fields induced by the beam as it passes through the structure, i.e. wakefields. These fields can be short-range, where fields from the particles at the head of a bunch interact with those at the tail of the bunch, or long-range, where fields from one bunch interact with later bunches. Short-range wakefields can lead to energy spread and transverse momenta within the bunch. Long-range wakefields can excite cavity modes with significant transverse fields, disturbing the

trajectories of following bunches. The effect of these long-range wakefields can combined in the wake potential as a sum over the n eigenmodes of the cavity, as given by Eq. 1.1.

$$W(s) = \sum_n a_n f_n(\vec{x}) e^{-i\omega_n s/c} e^{-i\omega_n s/2Q_n c} \tag{1.1}$$

Here the wake potential, W, is given as a function of the distance behind the lead bunch, s, for relativistic particles satisfying $s = ct$. This sum over the eigenmodes is dependent on the coupling to each mode, a_n, the field pattern of the mode as a function of transverse coordinate, $f_n(\vec{x})$, an oscillatory term with angular frequency ω_n, and a damping term with time constant $\tau_n = 2Q_n/\omega_n$, where Q_n is the quality factor of the nth mode. This expression shows that the effects of wakefields on later bunches can be reduced by any of the following: reducing the coupling to the mode, increasing the distance between bunches, increasing the frequency of the higher-order cavity modes, or decreasing the quality factor of the higher-order cavity modes without decreasing the quality factor of the accelerator mode. Of these options reducing the quality factor of the higher-order modes is both straightforward and does not affect the luminosity in collider applications.

The effectiveness of the damping of higher-order modes can be investigated computationally via the use of a particle-in-cell simulation code. The results of these wakefield calculations will be presented in Chapter 3.

1.2 Metamaterials and Photonic Band-gaps

In order to decrease the quality factor of higher-order modes in an accelerator cavity without decreasing the quality factor of the accelerator mode, i.e. decrease the ratio Q_n/Q_0 for all $n \geq 1$, the accelerator structure must have frequency dependent properties. This is a perfect application for an electromagnetic metamaterial structure. Electromagnetic metamaterials are artificial materials displaying properties not available in natural materials, created using structures with typical scale length smaller than the wavelength of the radiation being guided. The properties of these materials

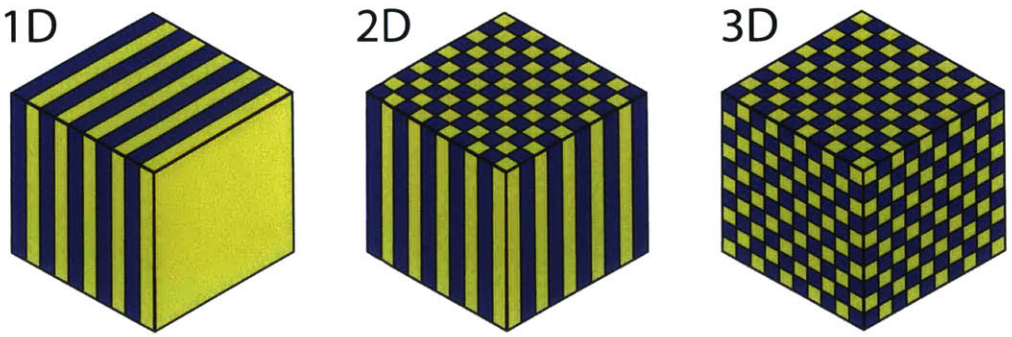

Figure 1-1: This figure shows a simple example of one, two, and three dimensional photonic band-gap structures. In these figures the different colors represent materials with different dielectric constants. The properties of these structures can be controlled by changing the dimensions and dielectric constants of the materials used.

are frequency-dependent and may exhibit such properties as a negative permittivity or permeability.

Sub-wavelength structures can also be used to create a material with a frequency-dependent reflectivity. By creating a void within such a material a cavity which confines a single frequency but is effectively transparent to higher frequencies can be constructed. Such a cavity would have a high-Q accelerator mode while reducing the Q of higher-frequency wakefields by allowing them to radiatively dissipate by passing through the structure walls. If such a frequency-selective structure is created via a periodic array of reflective elements it is called a photonic band-gap or PBG structure.

The periodic variation of the dielectric constant in a PBG structure can be in one, two, or three dimensions, as seen in Figure 1-1. The band gap referred to in photonic band-gap structures refers to frequency ranges at which the structure exhibits total reflection, i.e. gaps in the transmission band of the material. In multi-dimensional PBG structures these gaps can depend on the direction of propagation, or they can be complete band gaps where the material reflects electromagnetic waves regardless of direction of propagation. By creating a two-dimensional variation of reflective elements, either metallic or dielectric, with a complete band gap a frequency-selective waveguide can be formed, as discussed in Section 2.2. This waveguide can then be used to provide the transverse confinement in an accelerator structure, providing the simultaneous high-Q accelerator mode and low Q for higher-order modes required for

wakefield damping.

1.3 Motivated Research

Previous research has shown that an accelerator cavity can be constructed using a photonic band-gap design. Computational results have shown that structures with complete band gaps can be formed using square or triangular lattices of cylindrical metal rods. A six-cell traveling wave PBG accelerator structure with a triangular lattice was designed and tested at MIT, showing acceleration of electrons at a gradient of 35 MV/m [8, 9, 10]. While this original proof-of-principle experiment demonstrated confinement of the accelerator mode, wakefield damping was not investigated, and the structure was impractical for high-gradient operation.

While the design used for the proof-of-principle experiment had a complete band gap, the infinite lattice theory used to design that structure does not predict wakefield damping in finite lattices. In the case of a finite lattice modes propagating in the transverse direction have a finite group velocity. This leads to a finite transit time for radiation at these frequencies to exit the lattice, meaning finite quality factors for these modes. Because wakefield damping is a primary motivation for the use of photonic band-gap structures, investigation of the higher-order mode quality factors was a key focus of later research.

Investigation of the wakefield damping in the original six-cell, 17 GHz traveling wave PBG structure was presented in [11]. This work found good agreement between experimental results and theory for the power radiated by the beam at the fundamental frequency. It was also found that radiation in the accessible higher-order modes scaled according to theory, although the overall magnitude did not agree. Because the beam used for these experiments was bunched at 17.14 GHz, only harmonics of that frequency were observed, making agreement with theory more difficult.

While the results presented in [11], and discussed further in Ch. 3, validated wakefield damping in photonic band-gap structures, neither investigated, either experimentally or computationally, high-gradient operation of a PBG structure. Re-

search on high-gradient operation was conducted in collaboration with SLAC, as presented in [12]. For these experiments a standing-wave PBG structure with a single high-gradient cavity was designed. This structure was subjected to high-power rf testing to investigate the probability of breakdowns occurring in the structure during high-gradient operation. The structure was compared with an un-damped DLWG structure, and was found to have a much higher breakdown probability at a given gradient, owing in large part to the PBG structure's larger peak surface temperature rise at the same gradient. Because future collider designs seek to operate at high gradients, the understanding of how breakdown probability affects high-gradient operation of a PBG structure is a major motivation of this thesis research. The research presented here seeks to demonstrate experimental verification of high-gradient, low breakdown probability operation of an improved PBG structure at 11 GHz, the design of which is presented in [12]. This thesis will also present the design and experimental verification of breakdown physics in a PBG structure tested at 17 GHz.

1.4 Outline of Thesis

This thesis will present the development of PBG structures for high-gradient breakdown probability testing from previous research through improved testing methodologies and into adaption of the design to testing at higher frequencies. The theory behind accelerator cavity performance limitations and photonic band-gap structure design will be presented in Chapter 2. Computational results showing wakefield damping in photonic band-gap structures will be shown in Chapter 3. The basic design principles for, and the theory for analysis of, the single-cell structures used in breakdown probability testing will be presented in Chapter 4. Chapter 5 covers the cold test, hot test, and results of the testing of an elliptical-rod PBG structure at SLAC. The design variation and experimental setup of the experiments conducted at MIT is presented in Chapter 6. The cold test and hot test results for testing at MIT of two PBG structures and a DLWG structure will be presented in Chapter 7. Conclusions, discussions, and future work will be presented in Chapter 8.

Chapter 2

Theory

This chapter will serve to discuss in more detail the theoretical rigor needed to understand the motivation for and analysis of the experiments presented in this thesis. Many of the concepts were introduced in Chapter 1, and will be referenced in later chapters.

2.1 Accelerator Limits

As discussed in Chapter 1, the maximum surface fields, and therefore maximum gradient and pulse length, which can be sustained in an accelerator structure have been studied both experimentally and theoretically.

2.1.1 The Kilpatrick Limit and Loew-Wang Scaling

The simplest theory limiting the gradient in an accelerating structure is an empirical observation of the surface electric field at which electrons can be pulled off the surface in sufficient quantity that breakdown occurs. This theory was developed by Kilpatrick in the case of DC electric fields across a gap. By extending these spark gap experiments to oscillating voltage sources a frequency-dependent behavior was observed, with the breakdown field satisfying Eq. 2.1

$$f(MHz) = 1.64E_k^2 e^{-8.5/E_{crit}} \tag{2.1}$$

This equation must be solved numerically for the critical field, E_{crit} in MV/m, at each frequency f, in MHz. The surface field E_{crit} represents the maximum field that can be reached without breakdown occurring. Given that the ratio of the surface electric field to the gradient in an accelerating structure does not vary significantly from 2, this sets a limit on the highest gradient that can be achieved. For an rf frequency of 10 GHz this Kilpatrick limit predicts a maximum surface electric field of 82 MV/m; observed breakdown fields with the same order of magnitude frequency have been found to exceed this value by approximately a factor of seven [13].

This difference can be explained by looking at how the Kilpatrick limit was derived. The model used by Kilpatrick to explain the sparking behavior was to assume secondary electron emission due to ion bombardment. Assuming a linear relationship between ion energy and secondary electron yield, an empirical formula relates the ion energy, W, to the applied electric field, E. This expression is given in Eq. 2.2 [13].

$$WE^2/exp\left[-1.7 \times 10^3 E^-1\right] = 1.8 \times 10^{10} \tag{2.2}$$

By assuming a parallel plate gap an expression for W as a function of E and frequency, f, can be found. Given a single value of E at a known frequency f, a maximum allowable ion energy, W_{max}, can be found. This value of W_{max} is assumed to apply at all frequencies, giving the expression for f in terms of E_{crit} in Eq. 2.1. Among the reasons that this process fails to predict the observed field values are the fact that the data point used by Kilpatrick to calibrate the ion energy at the SLAC frequency of 2.856 GHz was approximately a factor of seven below the current observed value of breakdown field at that frequency and the fact that the geometry of an accelerator structure is not well-modeled by a parallel plate geometry.

The empirical results of Kilpatrick can, however, be extended to relevant frequencies by observing breakdown thresholds in modern accelerator cavities. This work was conducted by Loew and Wang at the Stanford Linear Accelerator Center. They

Table 2.1: Surface electric fields and gradients predicted from Loew-Wang scaling laws. Gradients are calculated assuming a ratio of $E_{surf}/E_{grad} = 2.5$.

Frequency	11.424 GHz	17.136 GHz
Peak Surface Electric Field, E_{crit}, (MV/m)	660	807
Accelerating Gradient, E_{grad}, (MV/m)	264	323

took data on breakdown threshold at frequencies of 2.856, 4.998, and 9.303 GHz. This data confirmed the $E_{crit} \propto f^{1/2}$ scaling present in the Kilpatrick limit. These experiments also looked at the breakdown threshold as a function of applied rf pulse length, t. These two results can be summarized in Eq. 2.3

$$E_{crit} \propto \frac{f^{1/2}}{t^{1/4}} \tag{2.3}$$

Given the values found by Loew and Wang, this scaling allows for the prediction of breakdown threshold at higher frequencies, including four and six times the original SLAC frequency, i.e. 11.424 and 17.136 GHz. The predicted values at these frequencies are given in Table 2.1 [13].

Further experimental work has failed to verify the high surface fields predicted by Loew-Wang scaling, including work at MIT on an rf photocathode [14, 15]. These results were confirmed by Next Linear Collider testing by Adolphsen et al. [16] and CLIC testing at 21, 30, and 39 GHz by Braun et al. [17]. The failure of further experiments to support the frequency scaling observed in early breakdown testing by Kilpatrick may be explained by the ion-initiated breakdown model used in that theory. In modern vacuum systems the ion density is very low, 10^{10} hydrogen atoms per cubic cm at 10^{-6} torr. This is in contrast to field emission current densities as high as 10^8 A/cm^2, the theory for which will be presented in the following section.

2.1.2 Fowler-Nordheim Field Emission and Breakdown

Given the high surface electric fields observed at breakdown, field emission is likely the dominant source of breakdown electrons. This current can be predicted by the theory of Fowler and Nordheim.

Assume a flat metal surface at x = 0 with an applied electrostatic potential. If the electrons within the metal surface have an energy W_a the potential, as a function of x, can by given by Eq. 2.4, where the electrostatic potential is modified by the space charge of the emitted electrons.

$$V(x) = \begin{cases} -W_a & \text{if} x < 0 \\ -eEx - e^2/4x & \text{if} x > 0 \end{cases} \tag{2.4}$$

This results in a potential barrier of finite thickness. Modeling the conduction electrons as a Fermi gas gives a population of electrons that can tunnel through the barrier. The value of this field emission current, in A/m^2, depends on the work function of the metal, ϕ in eV, and the magnitude of the applied electric field, E in V/m, as given by Eq. 2.5 [4].

$$j_{FN} = \frac{1.54 \times 10^{-6} \times 10^{4.52\phi^{-1/2}} E^2}{\phi} \exp\left(-\frac{6.53 \times 10^9 \phi^{3/2}}{E}\right) \tag{2.5}$$

This expression gives a frequency-independent prediction for the current emitted by a given applied field. Measurement of the field emitted current at which breakdown occurs, therefore, provides a prediction for the maximum surface fields which can be sustained in accelerator structures. The model of a perfectly smooth metal surface fails to predict the observed field emission current in experiments with a known surface electric field. This can be confirmed by plotting $\log(j_{FN}/E^2)$ versus $1/E$; the slope of this plot is proportional to $\phi^{3/2}$. Observed values of the slope, however, are 40-100 times smaller than ϕ. This is explained by the introduction of a geometry-dependent, dimensionless surface field enhancement factor, β, which models the field concentration at surface imperfections and modifies the electric field in Eq. 2.5, giving a new expression, Eq. 2.6.

$$j_{FN} = \frac{1.54 \times 10^{-6} \times 10^{4.52\phi^{-1/2}} (\beta E)^2}{\phi} \exp\left(-\frac{6.53 \times 10^9 \phi^{3/2}}{\beta E}\right) \tag{2.6}$$

The value of β can be calculated exactly for certain geometries, such as a cylinder of height h topped by a hemisphere of radius r [4], where $\beta \cong h/r$. While real surface

Table 2.2: Field emission current as a function of local surface electric field, βE.

βE(GV/m)	j_{FN} (A/μ m^2)
3	4×10^{-7}
6	5×10^{-2}
10	9

perturbations are not necessarily cylindrical, the aspect ratio (i.e. ratio of height over transverse dimension) of a real perturbation provides a reasonable estimate of beta. This means that beta can be calculated in two distinct ways: direct observation of surface perturbations via electron microscopy and indirect calculation of beta from plots of $\log(j_{FN}/E^2)$ versus $1/E$ from field emission experiments.

These two methods of calculating beta provide very different answers for accelerator structures. Analysis of surface perturbations observed via microscopy gives values of beta in the range of 5-10, while measurements of field emitted dark current gives values of beta in the 40-100 range [4]. These large values of beta are typically used to explain the breakdown fields observed in accelerator structures: surface fields of 300 MV/m are enhanced by beta values of order ten up to fields at the GV/m level, at which point the field emission current is sufficient to trigger a breakdown. The field emission currents for different values of βE are given in Table 2.2. While Fowler-Nordheim theory predicts the field emission current, it does not provide a prediction for why this current causes breakdowns.

A simple explanation for predicting breakdown from field emission is presented by Grudiev [18]. Assuming that the breakdown is the result of current flowing along a perturbation of height h and radius r, and that this current Ohmically heats the metal, the steady state current needed to heat the perturbation to a temperature T_m is given by Eq. 2.7.

$$j_m = \sqrt{\frac{k\ T_0}{h^2 \rho_{E0}}} \arccos T_0/T_m \tag{2.7}$$

This equation gives the current needed to go from an initial temperature T_0 to a steady state temperature T_m for a material with a thermal conductivity k and a

Table 2.3: Material properties of copper for ohmic heating calculations.

Quantity	Value
Thermal Conductivity k	400 W m^{-1} K^{-1}
Heat Capacity C_V	3.45 MJ m^{-3} K^{-1}
Resistivity at 300 K ρ_E	17 nΩm
Melting Temperature T_m	1358 K

conductivity ρ_E satisfying $\rho_E = \rho_{E0}T/T_0$ where ρ_{E0} is the resistivity at temperature T_0. The heat flux generated by this ohmic heating must satisfy the heat conduction equation in one dimension, Eq. 2.8, which can be solved to first order to give an approximate time constant τ_m given by Eq. 2.9, depending on k, T_0, T_m, the height of the perturbation h, and the heat capacity of the material C_V.

$$C_V \frac{\partial T}{\partial t} = k\frac{\partial^2 T}{\partial x^2} + j_{FN}^2 \rho_E \tag{2.8}$$

$$\tau_m = \frac{C_V T_0}{j_m^2 \rho_{E0}} \ln \frac{T_0}{T_m} \tag{2.9}$$

Equations 2.7 and 2.9 can be combined to give an equation relating the time it takes to heat a perturbation to the final temperature of the perturbation, as shown in Eq. 2.10.

$$\tau_m = \frac{C_V}{k} h^2 \ln \frac{T_0}{T_m} / \arccos^2 \frac{T_0}{T_m} \tag{2.10}$$

This equation contains multiple unknowns, and so must be solved by assuming some values to be known; the most useful approach is to assume a time and final temperature and solve for perturbation height. Using the values for copper given in Table 2.3, where T_m has been taken to be the melting temperature of copper and the pulse length is assumed to be 100 ns, the resulting perturbation height and melting current are given in Table 2.4. The value of β assuming a 200 - 300 MV/m surface electric field required to produce a field emission current equal to the melting current, and the corresponding perturbation radius are also given, assuming $\beta \cong h/r$.

Because the values for perturbation radius in Table 2.4 are less than the skin

Table 2.4: Calculated value of perturbation height h and field enhancement factor β assuming that the perturbation heats up from room temperature to the melting temperature of copper in 100 ns and surface electric fields of 200-300 MV/m. The perturbation radius r is calculated from β assuming the scaling $\beta \cong h/r$.

Quantity	Value for Copper
τ_m	100 ns
h	1μm
j_m	36A/μ m^2
β	40-60
r	17-25 nm

depth of copper at 17 GHz the electrostatic approximation used in the derivation of the Fowler Nordheim current is applicable. Because the field emission current required for a perturbation to melt in a time on the order of magnitude of the rf pulse lengths used in accelerator applications can only be generated by an enhanced surface electric field on the order of 10 GV/m, large surface enhancement factors are needed to explain the observed breakdown at surface electric fields of 200-300 MV/m.

The idea of breakdown as a result of field emission due to local surface field enhancement at surface perturbations does explain the processing seen in rf structures; as the applied surface field increases with applied power, high-β perturbations are melted and removed, resulting in lower peak values of β and increasing the power required for breakdown. The value of β required is, however, much larger than any value observed from pre- or post-processing imaging of high-gradient structures.

2.1.3 Surface Temperature Rise

The previous sections discussed limitations on the achievable gradient as the result of electric field effects, this section considers the effects of the surface magnetic field on the achievable gradient. This is an area of particular interest for photonic band-gap structures, as will be discussed in Section 2.2.3.

The large surface magnetic fields required to support the accelerating gradient in accelerator structures are concentrated on the walls of the cavities and input couplers. These surface magnetic fields drive large currents in the walls, which in turn create

Table 2.5: Material properties of copper for surface temperature rise calculations.

Quantity	Value
Thermal Conductivity k	400 W m^{-1} K^{-1}
Density ρ	8.95×10^3kg m^{-3}
Resistivity at 300 K ρ_E	17nΩ m
Specific Heat at Constant Strainc_ϵ T_m	385 J kg^{-1} K^{-1}
Thermal Diffusivity α_d	$1.1 \times 10^{-4}m^2s^{-1}$

ohmic heating. Unlike in the case of the Fowler-Nordheim current, this heating is not enhanced by surface perturbations. A more detailed analysis of the heat conduction and associated mechanical strain is presented in [19]; a brief derivation of the surface temperature rise will be presented here.

In three dimensions the heat conduction equation is given by Eq. 2.11, where k is once again the thermal conductivity and $\alpha_d = k/\rho_E c_\epsilon$ is the thermal diffusivity in terms of k, the density ρ, and c_ϵ is the specific heat at constant strain. The values for these parameters for copper are given in Table 2.5.

$$\nabla^2 T(\vec{r},t) + \frac{1}{k} g(\vec{r}t) = \frac{1}{\alpha_d} \frac{\partial T(\vec{r}t)}{\partial t} \tag{2.11}$$

The temperature rise on the surface of the material at an infinite vacuum-material interface can be approximated by Eq. 2.12, where $dP(t)/dA$ is the power dissipation per unit area. For the case of heating due to rf, the power dissipation is due to the magnetic fields, given by Eq. 2.13 for a surface magnetic field $H(t)$ and a surface resistivity R_s.

$$\Delta T = \frac{1}{\rho c_\epsilon \sqrt{\pi \alpha_d}} \int_0^t \frac{dt'}{\sqrt{t-t'}} \frac{dP(t')}{dA} \tag{2.12}$$

$$\frac{dP(t)}{dA} = \frac{1}{2} R_s |H(t)|^2 \tag{2.13}$$

These two equations can be combined to give the surface temperature rise due to rf magnetic fields given in Eq. 2.14. This equation will be used in conjunction with the time-dependent fields in the cavity calculated in Ch. 4 to determine the peak

surface temperature rise during rf testing.

$$\Delta T = \frac{R_s}{2\rho c_\epsilon \sqrt{\pi \alpha_d}} \int_0^t \frac{dt'}{\sqrt{t-t'}} |H(t')|^2 \tag{2.14}$$

For a theoretical rf pulse of length t measured in microseconds, constant magnetic field $|H|$ in MA/m, at a frequency f measured in GHz, the formula reduces to: $\Delta T = 430\sqrt{f/11.424}\sqrt{t}\,|H|^2$. The factor of $\sqrt{f/11.424}$ arises from the frequency scaling of the surface resistivity. This formula can be used to quickly estimate the temperature rise for a constant power pulse of a given length, however the actual temperature rise in such a pulse will always be less than the value given by this formula due to the filling time of the cavity. The peak surface temperature rise in a real structure, as calculated by numerical integration of Eq. 2.14, is typically on the order of tens, to at most 100-200, Kelvin. While this temperature rise is not enough to cause instantaneous damage to the copper surface, the repeated temperature rise with every rf pulse does affect the surface.

Note that Eq. 2.14 assumes that the surface resistivity is a constant. The resistivity of copper increases with temperature, with the dependence given by Eq. 2.15 [19]. This can result in runaway behavior where the increased resistivity causes the structure temperature to increase more, which increases the resistivity further, resulting in continuous increase in the structure temperature rise.

$$\rho_{res}(T) = 7.012 \times 10^{-11} T - 3.865 \times 10^{-9} (\Omega m) \tag{2.15}$$

Because the cavity Q also changes with R_S, this change in resistivity affects the temperature rise both due to R_S directly and due to the decrease in Q. The full equation for the peak temperature rise in the structure is therefore given by Eq. 2.16, where the magnetic field $H(t', T)$ is evaluated at the peak location, which is assumed to be constant [19].

$$\Delta T = \frac{1}{2\rho c_\epsilon \sqrt{\pi \alpha_d}} \int_0^t \frac{dt'}{\sqrt{t-t'}} R_S(T)\,|H(t', T)|^2 \tag{2.16}$$

This is now an integral equation for the pulsed heating temperature rise in the

cavity. This expression is known in the literature and, for simple geometries such as those considered in [19], can be solved. For the complex geometries and mode structure in PBG structures an exact solution is not practical. From [19] neglecting this change in surface resistivity will result in an underestimation of the temperature rise on the order of 10% for a temperature rise of 100 K.

2.1.4 Cyclic Fatigue

It is the cyclic nature, and not the peak value, of the surface temperature rise due to rf fields that causes accelerating structures to fail. Once again a more detailed discussion of cyclic fatigue is available in [19]; the material presented here will be a summary. Under cyclic stress or strain the material quickly undergoes cyclic hardening. After this the material undergoes crack nucleation, where cracks are observed to form on the surface of the material, typically at locations of lattice defects or locally increased strain. Finally the cracks propagate along the surface. The number of cycles to material damage or failure depends on whether failure is defined in terms of a density of cracks formed or a typical length of cracks formed. For the purposes of describing the lifetime of an accelerator structure, the structure can be considered damaged when the electrical properties of the surface change; this occurs during crack nucleation as the cracks increase the surface resistivity of the copper.

In order for thermal cycling of the material to cause damage, the temperature rise must be large enough that the induced stress is larger than the yield stress of the material. This occurs when the temperature increases quickly enough that the bulk material is inertially confined, and the surface subject to the heating is deformed. The temperature rise, ΔT_y, at which this stress level is reached is given by Eq. 2.17 in terms of the yield stress of the material, σ_y, Poisson's ratio, ν, the elastic modulus, E, and the coefficient of linear thermal expansion, α [20]. Continuous damage will not occur until the stress exceeds the yield stress in both tension and compression, meaning that the actual temperature rise above which continuous damage to the material will occur is $2\Delta T_y$. Using the values for copper listed in Table 2.6 gives a damage threshold of $2T_y = 40$ K. For temperature rises above this values damage is

Table 2.6: Mechanical properties of fully-annealed OFHC copper for calculating the yield temperature.

Quantity	Value for Copper
Yield Stress σ_y	$62MPa$
Poisson's Ratio ν	0.345
Elastic Modulus E	$123GPa$
Coefficient of Linear Thermal Expansion α	$1.65 \times 10^{-5}K^{-1}$

predicted to occur, but the severity of the damage and resulting structure lifetime is not predicted by this simple model. Uncertainties in the material properties used to calculate ΔT_y, as well as variation in these properties due to different surface preparations, means that this value is approximate.

$$\Delta T_y = \frac{(1-\nu)\sigma_y}{E\alpha} \tag{2.17}$$

Multiple experimental efforts have sought to quantify the actual acceptable temperature rise and lifetime of an accelerator structure. Work by Pritzkau presented in [20] found that for operation at 60 Hz repetition rate, a surface temperature rise of $120K \pm 10K$ for 5.6×10^7 1.25 μs pulses or 82K±3K for 8.6×10^7 1.5 μs pulses was enough to cause obvious damage to the copper surface of a cavity designed for high surface magnetic fields. This work also found that for the same pulse length and repetition rate a surface temperature rise of 250 K for 5.6×10^7 1.25 μs pulses at a coupler into the structure will cause enough surface damage to observe local melting of the copper that is qualitatively different than the damage observed at lower heating values. In all cases these are observations of damage after a known number of pulses and so do not represent the minimum number of pulses or minimum temperature rise for cyclic fatigue damage to occur.

The theory for thermal fatigue presented thus far assumes stress from thermal expansion of a uniform metal surface. Observations of surfaces damaged by pulsed heating show clear signs of grain boundaries [20, 21], which are a product of the non-uniform surface in an accelerator cavity. While Pritzkau notes that grain boundaries are a likely site for crack nucleation due to the increased stress at the boundary,

neither [20] or [19] treat the enhanced fatigue due to grain boundaries theoretically.

In order to account for this grain-grain interaction, Kuzikov and Plotkin, [6], developed a model for the number of pulses of a given pulse length and temperature rise required to damage the surface of an accelerator cavity. This model considers the probability of irreversibly breaking the bond between atoms in neighboring grains, and derives an equation for the number of pulses such that the probability of breaking all of the bonds between grain boundaries, i.e. surface fracture; this expression is given in Eq. 2.18.

$$N_f = \frac{C}{\exp(\zeta\sqrt{\tau}\Delta T^2) - 1} \tag{2.18}$$

This condition relies on experimental data to fit the free parameters C and ζ given the number of pulses at a pulse length τ and pulsed heating ΔT that were required to fracture the surface of the structure under test. Once C and τ are found Eq. 2.18 can be used to predict the lifetime of the structure. This condition can alternatively be expressed as, for a given structure lifetime, the product $\Delta T^2\tau^{1/2}$ must be a constant.

Equation 2.18 could be used to predict the lifetime of the photonic band-gap structures whose testing is presented here. Because, however, these structures are also used for breakdown rate testing they will not be subject to constant temperature rise, constant pulse length operation.

2.1.5 Pulsed Heating Damage

An important component of determining structure lifetime is assessing pulsed heating damage after testing. This can be done both through microwave measurements and through visual inspection. As discussed in Sec. 2.1.4, the cracks that form during cyclic fatigue cause the surface resistivity of the copper to increase, which in turn decreases the quality factor of the structure. This can be measured directly with a vector network analyzer. In the case where the external quality factor can be assumed constant, this can also be inferred during testing by measuring $\beta = Q_0/Q_E$. These changes in Q_0 represent the integrated effect of the changes in surface resistivity in

the cavity, and must be combined with assumptions about what surface area suffered pulsed heating damage to extract the effects of pulsed heating on the structure.

In order to accurately identify the location and severity of pulsed heating damage, structures are routinely autopsied, i.e. cut into pieces and imaged. This imaging can be done both visually and using scanning electron microscopy. In typically copper structures damage from pulsed heating is manifested as obvious grain boundary formation, slip bands, and crack formation on the surface. Qualitative comparisons can be made between the severity of damage from these images. These images can also be used to determine what areas of the structure suffered pulsed heating damage. This data can then be used to infer upper and lower bounds on the change in surface resistivity due to crack formation [20].

Visual inspection of the structure after testing can also be used to evaluate how different materials withstand cyclic fatigue due to high-power rf heating [21]. The work by Laurent et al. at SLAC extended upon the work of Pritzkau by using an improved cavity design to test a variety of materials under the same conditions, that is same temperature rise and number of pulses at that temperature rise, in an effort to determine what materials would best sustain pulsed heating operation. The majority of samples tested in this experimental program were subject to pulsed heating of approximately 100 K for 10^7 pulses, and the results were analyzed via imaging of the surfaces. This provides a large number of reference images for comparing pulsed heating damage. This work also showed that both grain size and material hardness affected resistance to cyclic fatigue damage, which is consistent with the theory presented in Sec. 2.1.4.

2.1.6 Alternative Theories of Breakdown

In addition to the theory presented above explaining the processes by which accelerator structure gradient is limited, other related theories have been presented. One such theory is presented by Norem et al. in [22]. This theory assumes a similar model of local field enhancement due to surface perturbations, but with two significant variations in the assumptions. The first is that breakdown initiation is the result

of local field stress at the location of a surface variation, regardless of whether that variation is a tip extending from the surface, a dislocation in the material, or a grain boundary. The second variation is the assumption that these surface perturbations are very small, potentially on the order of a few atomic radii.

Because the local field enhancement at the surface should be proportional to the radius of curvature of any surface variation, atomic-scale surface variations at perturbations, grain boundaries, and other defect regions can result in very large surface field enhancements without requiring very tall, narrow perturbations as considered in Sec. 2.1.1. This local field enhancement leads to field stresses greater than the atomic binding forces, which results in evaporation of both single atoms and small clusters of atoms. These evaporated atoms, which are subsequently heated, represent the initiation of breakdowns. This is in contrast to the earlier section, which assumes that local heating of perturbations results in melting that triggers a breakdown. In [22], breakdown at locations where the surface magnetic field is large are similarly assumed to be the result of local field enhancement at grain boundaries that form due to cyclic fatigue damage resulting from the large surface magnetic fields.

An additional alternative theory is presented by Nordlund and Djurabekova in [23], which attempts to explain the observed breakdown probability using a defect formation model. This represents a first-principles calculation of the scaling of breakdown probability with gradient and surface temperature rise, as opposed to the purely descriptive scaling presented in other sources, e.g. [18].

This model assumes that breakdown probability is proportional to the concentration of defects formed within the material as the result of applied electric and magnetic field stresses, assuming that both these stresses are proportional to the accelerating gradient. The mechanism by which field stress creates defects in the material is presented in more detail in [24]. This results in a model of breakdown probability with an exponential dependence on E_{acc}^2, where E_{acc} is the accelerating gradient, which is shown to fit well to existing breakdown probability data. The model also predicts that surface perturbations of the approximate dimension assumed in [18] and presented in Table 2.4, i.e. with transverse dimension of 10 - 100 nm, can be formed

from a smooth surface as the result of the formation of dislocation loops within the material[23]. This explains why large-β perturbations are not observed in SEM imaging of structures; the tips are only present under large applied rf fields which produce dislocations. While this model provides a good fit to existing data, and suggests that reducing defect density in the material through annealing or other processes would reduce breakdown probability, it does not simultaneously apply the effects of both surface electric and magnetic fields. This makes the model very promising, but it has not been applied to PBG structures, where the combined effects of both fields is presumed to be important.

2.2 Photonic Band Gaps

In order to achieve the frequency-selective mode confinement desired for wakefield suppression in high-gradient, high-frequency accelerators, photonic crystal cavities can be used. These cavities operate in the TM mode configuration to provide the axial electric field necessary for particle acceleration. In this thesis only structures operating in the TM_{01} mode will be considered. This mode is often referred to as the fundamental mode, accelerator mode, or design mode of the cavity. Because the TM_{01} mode is the lowest frequency mode of a cylindrical cavity all other modes can be referred to as higher order modes (HOMs). It is these HOMs that are responsible for wakefields, so minimizing the HOM Q relative to the fundamental Q is a fundamental objective of photonic crystal cavity design.

The frequency-selective nature of a photonic band-gap structure is dependent on the periodic array of reflective elements in the material. As shown in Figure 1-1 this variation can occur in one, two, or three dimensions. In the case of the accelerator structures presented here a two dimensional variation is used to provide mode confinement transverse to the direction of beam propagation. These accelerator structures also use a periodic array of metallic rods instead of materials of differing dielectric constant. The rods must be arranged in a regular tiling of the plane in order to apply periodic boundary conditions, meaning that the same polygon must

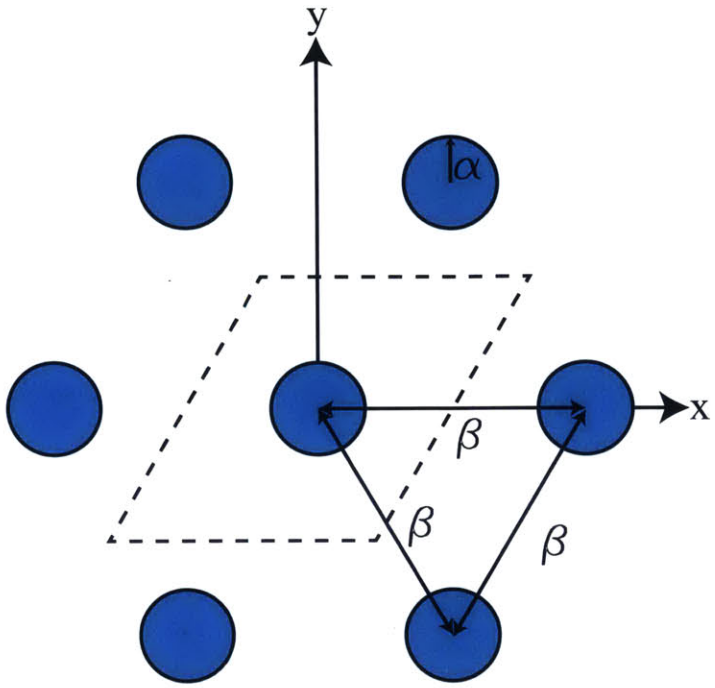

Figure 2-1: The fundamental unit cell of the triangular PBG lattice is shown. The metallic rods, with rod radius α and rod spacing β, are shown in blue, and the unit cell is the dashed area.

be used to cover the entire plane. This limits the rods to be placed at the vertices of either equilateral triangles or squares. Although both lattices can be solved, the quadrupole symmetry of the square lattice means it is less desirable for the damping of higher order modes in accelerator structures [8]. This work will therefore focus on the triangular lattice. Of primary interest in the discussion of a photonic crystal is calculation of the frequency ranges at which propagation is forbidden by the lattice, i.e. the band gap of the lattice.

2.2.1 The Band Gap

Once a lattice geometry has been chosen, the performance of that lattice can be parameterized into the filling factor or ratio of rod radius to diameter, α/β and the normalized frequency, $\omega\beta/c$. A lattice can be designed for a given ratio of α/β and then scaled to the frequency of choice by changing β. The fundamental unit cell for

the triangular lattice is shown in Figure 2-1, where the rod radius is denoted α and the rod spacing is denoted β. The lattice is mathematically defined by the conductivity profile,

$$\sigma(\vec{x}_\perp + \vec{T}_{mn}) = \sigma(\vec{x}_\perp) \tag{2.19}$$

$$\vec{T}_{mn} = \left(m + \frac{n}{2}\right)\beta\hat{e}_x + \frac{\sqrt{3}}{2}n\beta\hat{e}_y \tag{2.20}$$

where b is the lattice spacing, m and n are integers, and $\vec{x}_\perp = x\hat{e}_x + y\hat{e}_y$. Because this geometry is independent of time and uniform in the longitudinal direction, the longitudinal wave number k_z and the frequency ω can be assumed constant. This means that the fields in the structure satisfy the Helmholtz wave equation, Eq. 2.21, subject to the appropriate boundary conditions for TM modes, given by Eq. 2.22.

$$\vec{\nabla}_\perp^{\,2}\psi(\vec{x}_\perp) = \left(k_z^2 - \frac{\omega^2}{c^2}\right)\psi(\vec{x}_\perp) \tag{2.21}$$

$$\psi|_S = 0 \tag{2.22}$$

The periodic nature of the lattice permits a solution of the Bloch form,

$$\psi\left(\vec{x}_\perp + \vec{T}_{mn}\right) = e^{i\vec{k}_\perp\cdot\vec{T}_{mn}}\psi\left(\vec{x}_\perp\right) \tag{2.23}$$

where $\vec{k}_\perp = k_x\hat{e}_x + k_y\hat{e}_y$ is the transverse wave number. This equation can be used to solve the fields in the fundamental unit cell, shown graphically in Figure 2-1 and described mathematically in Eq. 2.24. Requiring that the solutions on the top-bottom and left-right boundaries of the unit cell are equal, as required by the discrete periodic nature of the geometry, further imposes the constraints given in Equations 2.25 and 2.26.

$$\left|x - \frac{y}{\sqrt{3}}\right| \leq \frac{\beta}{2},\ |y| \leq \frac{\sqrt{3}}{4}\beta \tag{2.24}$$

$$\psi\left(\frac{\beta}{2} + \frac{1}{\sqrt{3}}\beta y,\ y\right) = e^{ik_x\beta}\psi\left(-\frac{\beta}{2} + \frac{1}{\sqrt{3}}\beta y,\ y\right) \tag{2.25}$$

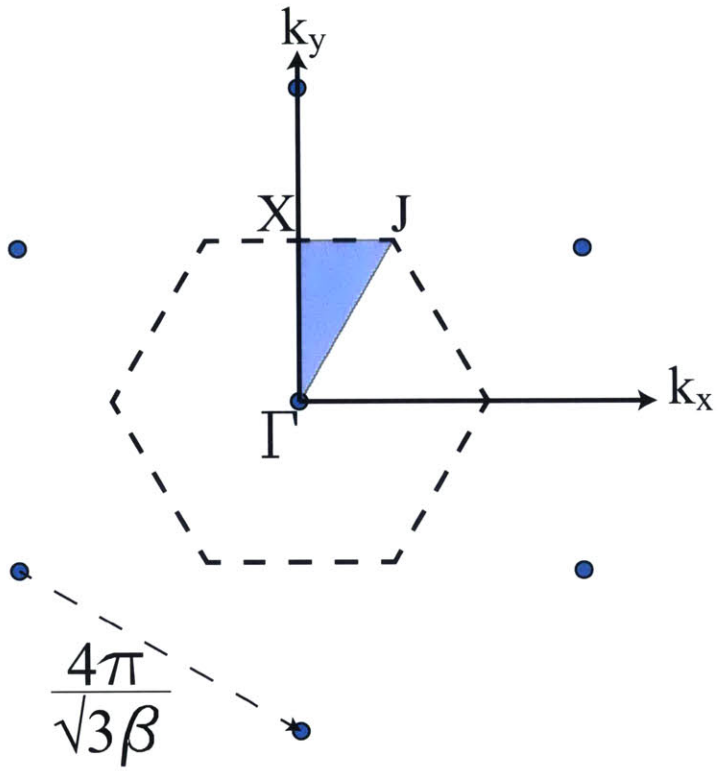

Figure 2-2: The reciprocal lattice for the triangular PBG is shown. The Brillouin zone is shown as a dashed line, and the irreducible Brillouin zone is shown as the shaded area.

$$\psi\left(x,\ \frac{\sqrt{3}\beta}{4}\right) = e^{ik_x\beta/2 + ik_y\sqrt{3}\beta/2}\psi\left(x - \frac{\beta}{2},\ -\frac{\sqrt{3}\beta}{4}\right) \tag{2.26}$$

Combining Equations 2.25 and 2.26 with the Bloch condition imposes limits on the allowed values of $\vec{k}_\perp$, forming the Brillouin zone shown in Fig. 2-2. The irreducible Brillouin zone is formed by the three points Γ, X and J, given by $\vec{k}_\perp = 0$, $\vec{k}_\perp = (2\pi/\sqrt{3}b)\hat{e}_y$, and $\vec{k}_\perp = (2\pi/\sqrt{3}b)(\hat{e}_x + 1/\sqrt{3}\hat{e}_y)$ respectively. These boundary conditions can be used to find the dispersion relation for the eigenmodes of the structure either numerically in the reciprocal space shown in Fig. 2-2 following the techniques discussed in [8] or by converting them to phase advance boundary conditions and solving directly in the fundamental unit cell using a simulation program such as HFSS [25]. This latter technique is discussed in detail in [26]; the results from both techniques are in good agreement.

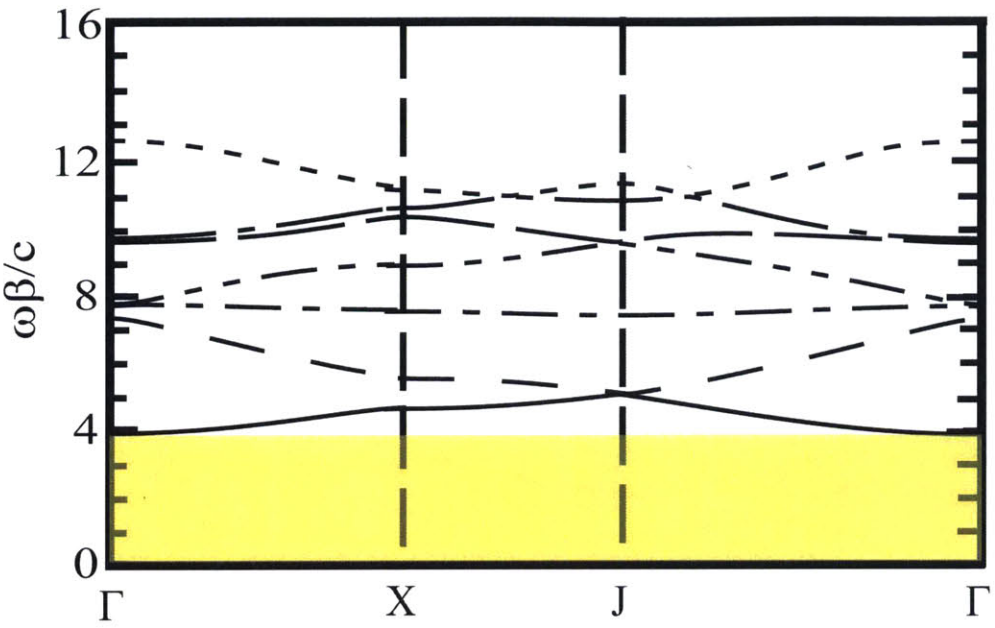

Figure 2-3: This shows the dispersion curves for the seven modes with the lowest normalized frequency in the triangular lattice PBG structure with $\alpha/\beta = 0.2$. The band gap is shown in yellow.

The results of this calculation for the first seven modes are shown in Figure 2-3 in terms of normalized frequency versus wave number for an α/β of 0.2. Frequency ranges where modes are present will have propagation in the transverse direction with finite group velocity. Frequency ranges where no modes are present form the band gap for the structure. Note that the group velocity is given by the slope of the dispersion relation in $\omega - k$ space, so at the edges of the bands modes with zero group velocity exist. In the case of the perturbed finite lattices used in accelerator structures these modes can remain and appear as unexpectedly high-Q HOMs [27].

By repeating this analysis for many values of α/β a band gap map is constructed, showing the normalized frequencies at which propagation is prohibited as a function of filling factor; such a map is shown in Figure 2-4. On this plot the region on the bottom right of the plot shows where propagation is prohibited, i.e. modes at these frequencies will be confined within a defect created in the lattice. This map can then be used to select a desired filling factor for an accelerator design. For a lattice of metallic rods as considered here the band gap always extends to zero frequency,

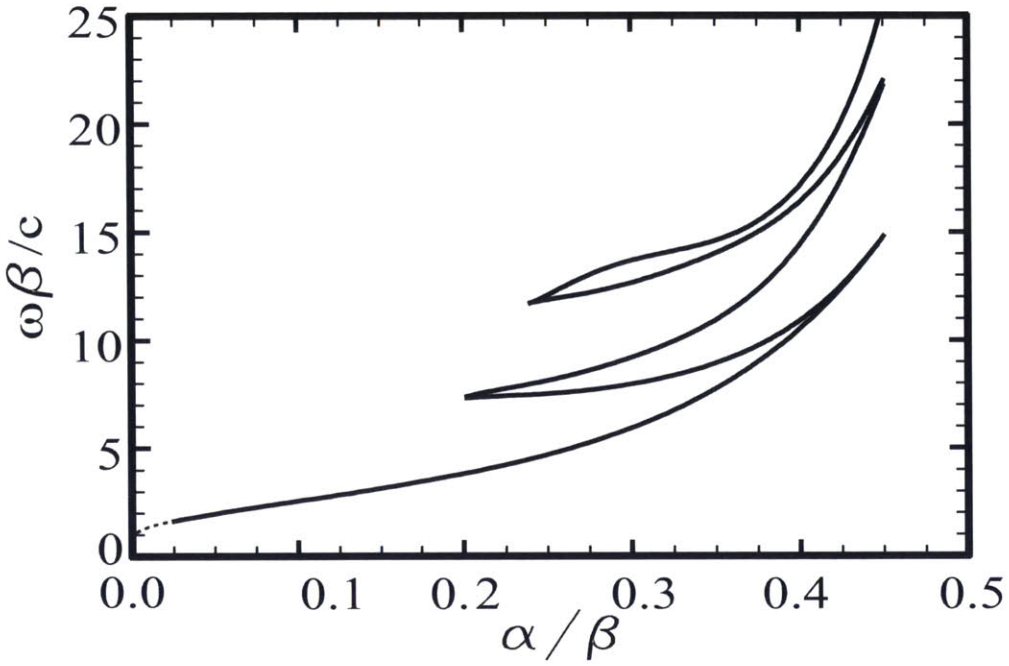

Figure 2-4: The band gap as a function of filling factor, α/β, for a triangular PBG lattice is shown. The band gap extends to zero frequency for all filling factors, and is confined by the outlined region. Incident rf radiation within this region will be reflected by the lattice, allowing a defect mode to be confined.

meaning that in order to provide damping of the other parasitic modes of the structure α/β must be kept below 0.2 where there is no higher gap to confine the HOMs.

2.2.2 Defect Modes

The discussion up to this point has considered the behavior of the lattice as a whole. In order to create an accelerator cavity an operating mode must be localized in the lattice. This is done by removing a single rod to create a defect. Because the band gap extends to zero frequency, and only a single rod has been removed, the lowest frequency mode that can be supported in the defect will be the TM_{01} mode. The geometry of this defect region is shown in Fig. 2-5 (A) and the resulting field calculated from HFSS is shown in Fig. 2-5 (B).

In addition to having a defect region, the lattices used in PBG accelerator structures are, unlike those discussed in Sec. 2.2.1, finite. This results in a modification

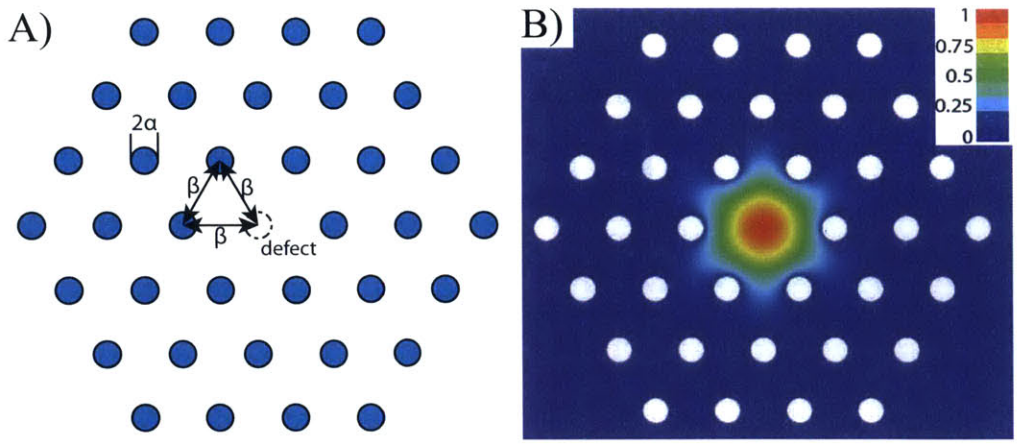

Figure 2-5: This shows the metallic lattice geometry and resulting TM_{01} mode for a triangular PBG lattice with $\alpha/\beta = 0.18$. The geometry is shown in (A) with the defect and lattice parameters indicated. The magnitude of the normalized electric field from an HFSS simulation of this geometry is shown in (B).

of the mode confinement assumed in the infinite case; modes in the gap have finite transmission through the finite lattice and modes outside of the gap have finite reflection from the finite lattice. The diffractive quality factor of all of the modes confined by the cavity increases the number of layers of rods, approaching the limit of a cavity with a solid wall. Because the structure has a finite Q due to surface losses, increasing the number of layers of rods in the design has diminishing marginal returns as the diffractive Q becomes much larger than the Ohmic Q. For a round-rod PBG structure with filling factor $\alpha/\beta = 0.18$ three layers of rods are sufficient for the total Q to be dominated by the wall losses.

The filling factor of the lattice must also be chosen to balance confinement of the fundamental mode with damping of the higher order modes. As α/β increases the Q of all of the modes in the structure will approach the Q factors for those modes in an equivalent cylindrical cavity where $Q_{HOM} > Q_{Accel}$. The different quality factors increase at different rates, however, leading to an optimum value of $\alpha/\beta \approx 0.17$ for damping of the next lowest frequency mode, as shown in [28]. Choosing a filling factor near this optimal value provides a reasonable amount of HOM damping; improvements in both HOM damping and fundamental mode confinement can be achieved via perturbations of the lattice [29, 30].

2.2.3 Magnetic Field Enhancement

One undesirable consequence of HOM damping via diffractive loss, both in PBG structures and it other types of damping such as waveguide HOM damping, is an increase in the surface magnetic fields. In an undamped structure the surface currents that support the mode flow uniformly around the azimuth of the structure. When portions of this surface are removed for HOM damping the same current must flow in a smaller volume, resulting in higher surface magnetic fields. This effect can be counteracted in PBG structures by changing the shape of the inner layer of rods to effectively increase the filling factor without sacrificing HOM damping.

A simple geometry to achieve this reduction in surface magnetic field is to use elliptical rods for the first layer with the major radii of the ellipses perpendicular to the line between the center of the defect region and the center of the elliptical rod. This will be covered in more detail in Ch. 5, where this technique was used to reduced the pulsed heating in PBG breakdown testing.

Chapter 3

Wakefield Simulations

A fundamental objective of the photonic band-gap design is the damping of the higher-order modes, thereby reducing the wakefields in the structure. An important step in validating the PBG design is confirming this wakefield damping. As mentioned in Chapter 1 and presented in [11], simulations of the wakefields in the six-cell traveling-wave PBG structure tested at MIT showed the appropriate scaling, but did not agree with the magnitude of the wakefields observed in experiment. This simulation work sought to model the entire experimental volume, greatly increasing the computation demands of the simulation. While the purpose of this experiment was to measure wakes excited at the fundamental and harmonics of the bunch-train frequency and not damping of modes in the dipole badn, dipole mode damping is an important feature of the design which should be verified via simulation. In order to verify wakefield damping, the wake potential in both a conventional undamped disc-loaded waveguide (DLWG) structure and a PBG structure were simulated using the particle-in-cell (PIC) code Particle Studio from CST [31].[1]

3.1 Wake Potential Theory

The general theoretical work for the analytical calculation of wakefields has been developed in [33, 34, 35, 36]. The wake potential is the summation over all of the

[1]This chapter is adapted from [32].

structure modes excited by the impulse. The longitudinal and transverse wake potentials in cylindrically symmetric structures can be written as [33, 36]:

$$
\begin{aligned}
W_z(r', r, s) = & \sum_{m=0,n=1}^{\infty} 2\left(\frac{r'}{d}\right)^m \left(\frac{r}{d}\right)^m \\
& \cos(m\theta) k_{zmn}(d) \cos\left(\frac{\omega_{mn} s}{c}\right) \exp\left(-\frac{\omega_{mn} s}{2Q_{mn} c}\right) \\
\mathbf{W}_\perp(r', r, s) = & \sum_{m,n=1}^{\infty} 2m\left(\frac{r'}{d}\right)^m \left(\frac{r}{d}\right)^{m-1} (\hat{r}\cos(m\theta) - \hat{\theta}\sin(m\theta)) k_{\perp mn}(d) \\
& \sin\left(\frac{\omega_{mn} s}{c}\right) \exp\left(-\frac{\omega_{mn} s}{2Q_{mn} c}\right)
\end{aligned}
\tag{3.1}
$$

where s is the distance behind the driving bunch, r' is the displacement of the driving bunch, r is the test beam transverse position, d is the radius of the iris aperture, k_{zmn} is the loss factor, $k_{\perp mn}$ is the kick factor, ω_{mn} is the frequency, c is the speed of light and Q_{mn} is the quality factor of the TM_{mn} mode. In Eq. 3.1:

$$k_{zmn}(d) = \frac{|V_{mn}(d)|^2}{4U_{mn}} \tag{3.2}$$

$$k_{\perp mn}(d) = \frac{k_{zmn}(d)}{\omega_{mn} d/c} \tag{3.3}$$

where V_{mn} is the voltage along one period and U_{mn} is the stored energy in the TM_{mn} mode. From Eq. 3.1 we can see that the initial transverse wake potential depends on the kick factor $k_{\perp mn}$, and damping is induced by the damping factor $\exp(-\omega_{mn} s/2Q_{mn} c)$. Low initial transverse wake potential can be reached by decreasing the kick factors of the modes, but effective wake potential damping can be achieved primarily by decreasing the quality factor Q_{mn}.

The longitudinal and transverse wake potentials are described in the time domain. The corresponding longitudinal and transverse impedances for the frequency domain description can be defined as in [35]:

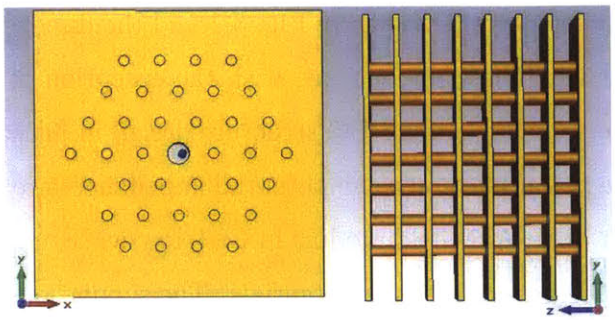

Figure 3-1: Schematic of a seven cell PBG structure. The structure is formed by three rows of a triangular lattice of metallic cylindrical rods. The central rod is removed to form a defect region to confine the fundamental TM_{01} mode. The dimensions are given in Table 3.1.

$$Z_z(\omega) = \frac{1}{c}\int_{-\infty}^{\infty} W_z(s)e^{-j\omega s/c}ds \tag{3.4}$$
$$Z_\perp(\omega) = \frac{1}{jc}\int_{-\infty}^{\infty} W_\perp(s)e^{-j\omega s/c}ds$$

The above formulas can be used to analytically calculate the wake potentials in right-cylinder structures in which the electromagnetic fields can be expressed in a closed form, such as pillbox resonators [37] and disc-loaded waveguide (DLWG) structures [38, 39] with excitation by a point charge [40] or charged rings [41].

3.2 Photonic Band-gap Simulation

In an effort to reduce the computational demands of the simulation, the experimental geometry was simplified for the simulations presented here. In addition to limiting the simulation to the structure itself instead of including the vacuum chamber and waveguides used in the experiment, the structure was also simulated as either six or seven uniform cells; the experimental structure had six cells consisting of four uniform cells and coupling cells at either end. The results presented here are from the seven-cell simulations which initially showed greater promise, although all results have been confirmed for the six-cell simulation.

The simulation geometry is shown in Fig. 3-1 and the dimensions of the structure are given in Table 3.1. These dimensions, with the exception of the number of cells, are taken from the traveling-wave PBG structure design in [9] which has been tested at MIT [11]. Wake potentials and wake potential impedances are calculated per meter of structure length. The Wakefield module in CST Particle Studio is used to calculate the longitudinal and transverse wake potentials. The simulations considered both the ohmic loss due to the finite conductivity of the copper structure and diffractive losses due to power incident on the absorptive boundary layer surrounding the structure. In the experimental test of the structure the diffracted power was dissipated by diffuse reflections in a large external vacuum chamber; dissipation of this power in an accelerator structure represents a future engineering challenge.

For single-bunch measurements, an electron beam of zero transverse dimension and a 1 mm Gaussian length is injected into the beam tunnel with a 0.8 mm displacement in the x direction, as shown in Fig. 3-1. Calculation of the wake potentials with the same beam displacement in the y direction yields the same results.

The longitudinal and transverse wake potential are shown as a function of distance behind the bunch in Fig. 3-2(a) and Fig. 3-3(a). The longitudinal and transverse wake potential impedances are obtained to analyze frequency domain features in Fig. 3-2(b) and Fig. 3-3(b).

The longitudinal wake potential calculated on the beam track decays slowly, as shown in Fig. 3-2(a). The normalized frequency spectrum of the longitudinal wake

Table 3.1: Dimensions of the PBG structure

Geometric parameters	Value
Rod radius, a	1.04 mm
Rod spacing, b	6.97 mm
Iris thickness, t	1.14 mm
Iris radius, d	2.16 mm
Cavity length, L	5.83 mm
TM_{01} mode frequency	17.14 GHz
Accelerating mode	$2\pi/3$ mode
Number of cells	7

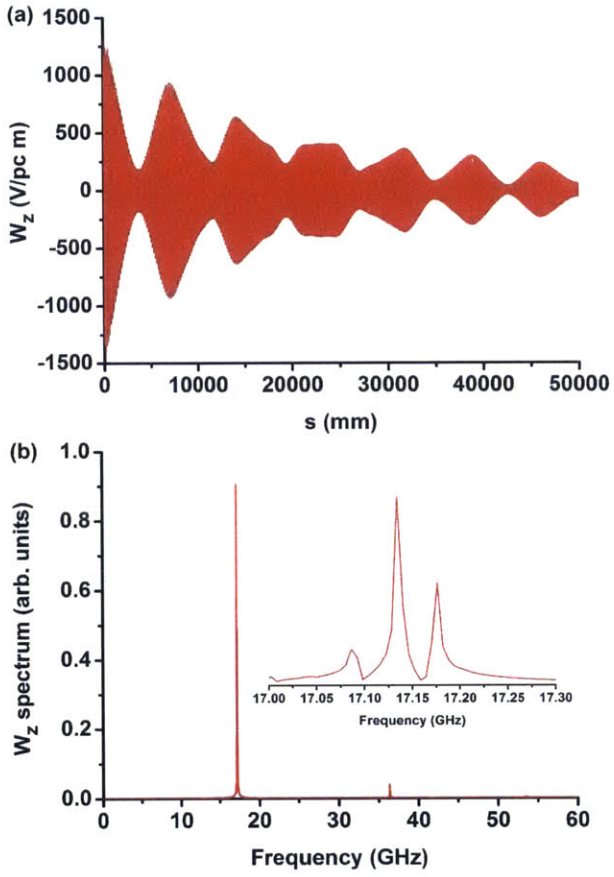

Figure 3-2: Calculation of longitudinal wake potential and impedance:(a) Longitudinal wake potential on a line parallel to the structure centerline and displaced 0.8 mm in the x direction, i.e. following the path of the beam; (b) Longitudinal wake potential impedance.

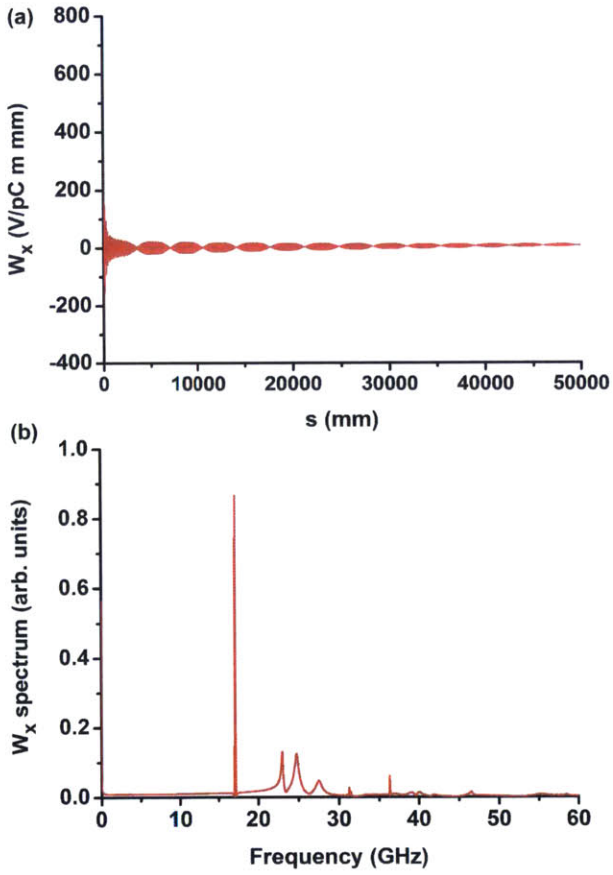

Figure 3-3: Calculation of transverse wake potential and impedance: (a) Transverse wake potential on a line parallel to the structure centerline and displaced 0.8 mm in the x direction, i.e. following the path of the beam; (b) Transverse wake potential impedance.

potential shows that the fundamental mode has three peaks at 17.002 GHz, 17.092 GHz and 17.176 GHz, as shown in top right of Fig. 3-2(b). These peaks reveal the different phase advances (0, $\pi/3$, $2\pi/3$) of the fundamental mode excited by a single bunch in the 7-cell PBG structure; these peaks agree with the previous theoretical analysis and the cold test in [10, 8]. The fundamental frequency resolution in the spectrum is 6 MHz which is limited by the finite simulation length. The dipole modes do not contribute to the longitudinal wake because the longitudinal electric fields of dipole modes are zero in the center, so there is no peak.

The transverse wake potential, shown in Fig. 3-3(a), can be seen to damp much faster than the longitudinal wake potential. The transverse wake potential damps quickly because its main contributions come from the dipole modes and the dipole modes have small Q-factors. The fundamental mode present in the frequency spectrum of the transverse wake potential is formed due to the irises and confined in the defect area. The high Q-factor of the TM_{01} mode keeps the transverse wake potential at a small but stable value at 50000 mm behind the electron beam. Three dipole modes are excited at 23.0 GHz, 24.8 GHz and 27.5 GHz with comparable initial amplitudes. The field distributions of these modes are shown in Fig. 3-4. These modes are distinguished as TM_{11}-like, TM_{12}-like and TM_{13}-like modes separately and all of these modes are not confined within the defect region, but radiate away from the center to the outer boundary. The detailed analysis of the dipole modes will be given in Sec. 3.3.

3.3 Dipole Mode Analysis

Fig. 3-3(a) shows that the transverse wake potential in the PBG structure is quickly damped. The transverse wake is dominated by three dipole modes, with similar initial amplitudes and with frequencies within 4 GHz of each other. This indicates that the previous approach of considering only the lowest-frequency dipole mode is insufficient for predicting the transverse wake potential.

To isolate the contribution to the wake potential from each dipole mode indepen-

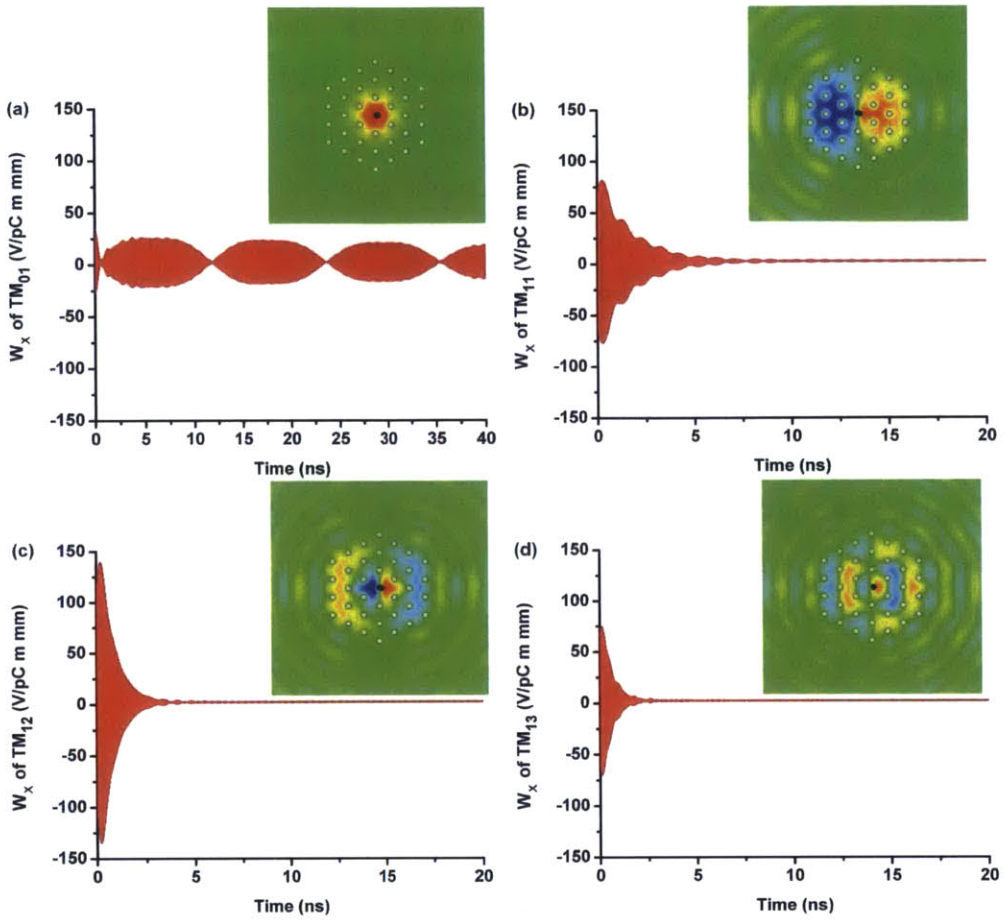

Figure 3-4: Transverse wake potential as a function of time for each mode in the PBG structure: (a) TM_{01}-like mode at 17.1 GHz; (b) TM_{11}-like mode at 23.0 GHz; (c) TM_{12}-like mode at 24.8 GHz;(d) TM_{13}-like mode at 27.5 GHz.

dently, numerical filters were used to separate the different modes within the wake potential. The filtering was done in Matlab using the digital signal processing toolbox. For each frequency a bandpass filter was applied in frequency space. An inverse fast Fourier transform was then applied to the filtered spectra to obtain the time-domain signal showing the damping for each dipole mode.

Fig. 3-4 shows the separate frequency components of the transverse wake potential versus time ($t = s/c$) and the field distribution at each dipole mode frequency. The fundamental mode (Fig. 3-4(a)) is confined in the defect region in a PBG cavity with a high Q-factor, providing a small, slow-decaying transverse wake potential. The

Table 3.2: Comparison of $1/e$ distances calculated from HFSS and CST simulation results.

Mode	Freq. (GHz)	Q value	HFSS $1/e$ dist.	CST $1/e$ dist.
TM_{01}-like	17.1	3955	2.2×10^4mm	3.0×10^4mm
TM_{11}-like	23.2	71	290mm	480mm
TM_{12}-like	24.7	57	220mm	210mm
TM_{13}-like	27.0	45	170mm	140mm

transverse electric field component of the TM_{01} mode is caused by the irises. The beating visible in the fundamental mode is caused by the different fundamental modes shown in Fig. 3-2(b).

The lowest-frequency TM_{11}-like dipole mode (Fig. 3-4(b)) decays more slowly than the two other dipole modes. The TM_{12}-like dipole mode (Fig. 3-4(c)) reaches a maximum amplitude a short time after the bunch passes and decays faster than the TM_{11}-like mode. The TM_{13}-like mode (Fig. 3-4(d)) has the highest frequency and is excited with less than half of the intensity of the previous dipole modes and decays faster than either of the lower-frequency dipole modes. The relative intensity of these dipole modes agrees well with the wake potential spectrum shown in Fig. 3-3(b).

From Eq. 3.1, the decay of the wake potential is related to the damping factor $\exp(-\omega_{mn}s/2Q_{mn}c)$. Because the frequencies of these dipole modes are close, the quality factor of each mode is the dominant contributor to the damping of each mode.

To calculate the quality factor of each mode, eigenmode simulations are run with the same simulation environment as in CST Particle Studio, i.e. a lossy copper structure with an absorbing boundary layer located outside of the PBG lattice. Because CST Microwave Studio does not support the use of absorptive boundary layers in eigenmode simulations, the Ansys code HFSS, which does support absorptive boundary layers in eigenmode simulations, is used instead. All three dipole modes are found to have a phase advance per cell of approximately π in the CST simulation, so the phase advance per cell is set to desired value of $2\pi/3$ for the fundamental mode and the observed value of π for the dipole modes in the HFSS simulations.

The results of the eigenmode calculations in HFSS are shown in Table 3.2. The quality factors in Table 3.2 contain both the ohmic losses and diffractive losses in the structure. The frequencies of the modes in the HFSS simulations agree well with the frequencies observed in the CST simulations.

The HFSS results provide good qualitative agreement with the damping times of the respective dipole modes calculated in the CST simulation. The $1/e$ distance of the wake potential, $(2Q_{mn}c)/\omega_{mn}$ from Eq. 3.1, is calculated for each mode from the Q-factor and ω obtained from HFSS. The $1/e$ distance is also calculated from the decay distance of the wakes observed in CST. These two values of $1/e$ distance are shown in columns 3 and 4 of Table 3.2. The two different simulation techniques give reasonable agreement between the decay distances for each mode. This validates the use of simple single-cell eigenmode models to predict approximate decay distances for modes excited by the beam.

3.4 Comparison of Wake Potential in PBG and DLWG Structures

The previous results confirm that the PBG structure provides wake potential damping, although three dipole modes are excited. To compare the strength of the wake potential damping in the PBG structure the wake potential in the PBG structure is compared the wake potential in an equivalent 7-cell traveling-wave disc-loaded waveguide structure with the same iris geometry, as shown in Table 3.3. The CST PS

Table 3.3: Dimensions of the DLWG structure

Geometric parameters	Value
Cavity radius, b	6.91 mm
Iris thickness, t	1.14 mm
Iris radius, d	2.16 mm
Cavity length, L	5.83 mm
Accelerating mode	$2\pi/3$ mode
Number of cells	7

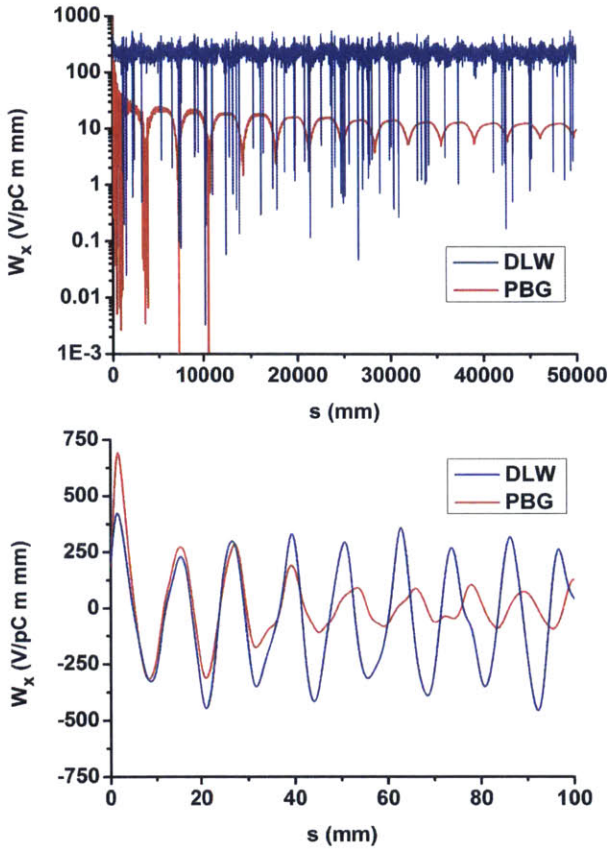

Figure 3-5: Comparison of transverse wake potential between DLWG and PBG structures. The blue line is DLWG wake potential, and the red is PBG wake potential: (a) The envelope of transverse wake potential in DLWG and PBG along 50000 mm; (b) The first 100 mm of the transverse wake potential in both structures.

Wakefield module was used to simulate the equivalent disc-loaded waveguide structure.

The transverse wake potentials for the disc-loaded waveguide structure and the PBG are shown in Fig. 3-5. From the theory, the quality factor of the PBG structure includes two parts: Q_{ohm} and Q_{diff}. Q_{ohm} depends on the ohmic loss of copper, and Q_{diff} accounts for the diffractive loss in the structure. The Q_{diff} in the disc-loaded waveguide structure is very large because of the closed cavities, so the total Q in the disc-loaded waveguide structure depends only on the ohmic Q. The diffractive Q of the fundamental mode in the PBG is finite but much larger than Q_{ohm} because this mode frequency lies in the band gap of the structure.

Fig. 3-5 shows the comparison of the transverse wake potential between the disc-loaded waveguide structure and the PBG structure. This clearly indicates that the wake potential in the PBG structure damps much faster than in the disc-loaded waveguide structure. In the PBG structure the transverse wake potential is highly damped within the first 500 mm, whereas the transverse wake potential in the disc-loaded waveguide structure is not significantly damped even at 50000 mm after the drive bunch. This proves that the PBG structure provides significant damping of the transverse wake potential relative to a disc-loaded waveguide structure. Fig. refFig:PBGvsDLWGWake(b) shows a detail of the first 100 mm of the transverse wake potential, indicating that the initial amplitude of the transverse wake potential in both structures is approximately the same, but the wake in the PBG structure shows significant damping after the first 30 mm.

Fig. 3-6 shows the comparison of the transverse spectrum between the PBG and the disc-loaded waveguide structure. Fig. 3-6(a) shows that in the disc-loaded waveguide structure the TM_{11} π mode (25.1 GHz) has an extremely high peak, and the next higher peaks appear at 38.5 GHz and 54.5 GHz. In conclusion, all of these simulations demonstrate the effective damping of wakefields in PBG structures designed for accelerator applications.

3.5 Multi-Bunch Simulation and Beam Loading Calculation

A six-cell PBG structure with the same iris geometry has been experimentally tested at MIT using the MIT/Haimson accelerator [11]. This experiment was conducted with a train of 1 ps bunches spaced at 17 GHz. This was modeled in the PIC module in CST using a multi-bunch excitation. The simulated PBG structure, shown in Fig. 3-1, had 7 cells to be consistent with the other simulations shown here, and to reduce computation time also used uniform cells instead of the coupling cells and waveguides used in [11]. The simulation used an on-axis train of 1 ps long bunches separated

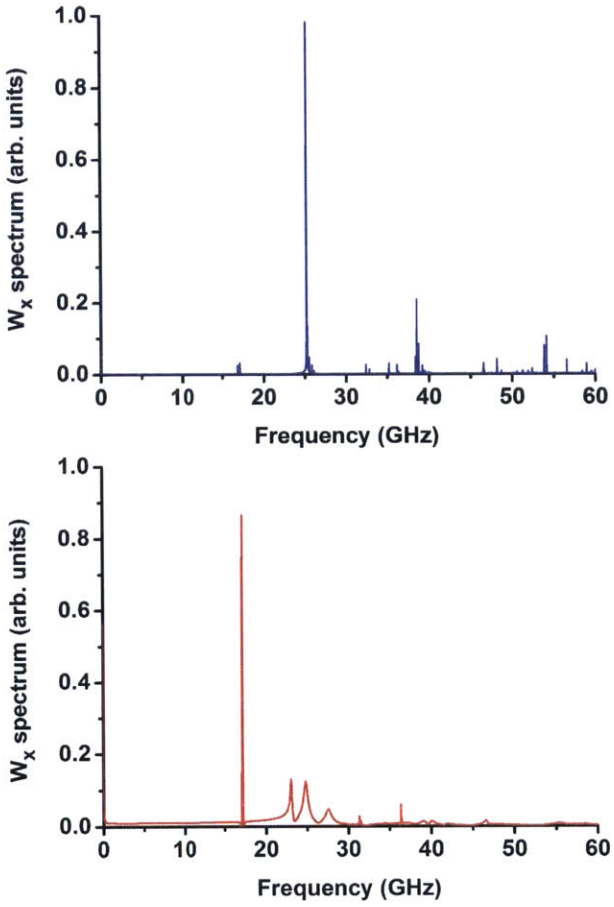

Figure 3-6: Comparison of transverse wake potential impedances between PBG and DLWG structures: (a) The transverse wake potential impedance in the DLWG; (b) The transverse wake potential impedance in the PBG (same as Fig. 3-3(b)).

by 58.1 ps to simulate the long bunch train of the experiment. The total charge of one bunch is 20 pC, corresponding to 344 mA current. The longitudinal E-fields are calculated on-axis.

The longitudinal E-fields at the center of a cell on the beam axis and 35 mm off the beam axis are calculated in CST, showing that most of the energy in the fields is in the fundamental mode, with the second and third harmonics observed approximately 30 dB below the fundamental. The magnitude spectrum of the longitudinal E-field calculated outside the structure about 35 mm away from the beam reveals that the fundamental mode is well confined to the defect area, but the second harmonic, whose frequency is in the pass-band of the lattice, propagates out of the lattice with a small decrease in amplitude. Three dipole modes can be recognized with much lower energy. Due to the coherence, the fields at the frequency of the beam train (17.2 GHz) and its harmonics (34.4 GHz, 51.6 GHz, etc) are enhanced, so the energy in the dipole modes is much lower than the fundamental modes and the harmonics. The calculated E-field at the fundamental is about 10 dB lower than that at the second harmonic, which agrees well with the experimental results measured outside the chamber window [11].

As a check on the applicability of the simulation results to experiment, the beam loading in the simulation can be compared to the beam loading in the theory and the experiment [11]. From the theory [42], the longitudinal electric field induced by the beam after traversing a distance l is:

$$E_b = ir_s\left(1 - e^{-Il}\right) \tag{3.5}$$

where, i is the beam current, r_s is the shunt impedance per unit length and I is the voltage loss per unit length. I can be described as a function of frequency (ω), group velocity (V_g), and quality factor (Q) of the structure [43]:

$$I = \frac{\omega}{2V_gQ} \tag{3.6}$$

The magnitude of the E-field induced by the bunched beam can be calculated from Eq. 3.5 and Eq. 3.6. The theoretical magnitude of E_b in the middle of the fifth cell (i.e. at $z = 32.1$mm) , is calculated to be 3.4×10^6 V/m, using $V_g = 0.013c$, $r_s = 98M\Omega/m$, $Q = 4200$ [10], and beam current $i = 344$ mA. In the CST simulation the steady-state amplitude of E_b measured on-axis in the middle of the fifth cell, when driven by a train of on-axis bunches, is observed to be 4.6×10^6 V/m. This result agrees reasonably well with the theory.

The induced power is given by:

$$P_b = \frac{E_b'^2}{2Ir_s} = \frac{E_b^2 V_g Q}{\omega r_s} = \left(\frac{i^2 r_s}{2I}\right)(1 - e^{-Il})^2 \tag{3.7}$$

Which, upon substituting Eq. 3.6 into Eq. 3.7, gives:

$$P_b = \left(\frac{i^2 r_s V_g Q}{\omega}\right)\left(1 - \exp\left(-\frac{\omega l}{2V_g Q}\right)\right)^2 \tag{3.8}$$

Because $\frac{\omega l}{2V_g Q}$ is much smaller than 1, the expression can be reduced to Eq. 3.9 via Taylor expansion.

$$P_b = i^2 \frac{\omega l^2 r_s}{4V_g Q} \tag{3.9}$$

Using the steady-state field amplitude from the simulation and Eq. 3.7, the electromagnetic power induced by the beam in the simulation is calculated to be 33 kW. By comparison the theoretical power induced by the beam after 32.1 mm is 18 kW.

From [11] the experimental value of the power induced by a 344 mA current beam is calculated to be approximately 13 kW in a 6-cell PBG structure with two ports coupling the field at the first and the sixth cells. This coupling makes the effective length of the structure at the measurement location shorter by approximately the length of one full cell, making the effective length 26.7 mm instead of the 32.1 mm

used in the simulation. From Eq. 3.8 the power induced by the beam scales as the square of the length; scaling the length of the structure in simulation gives a predicted beam induced power of 23 kW. This represents reasonable agreement between the power induced by the beam in the simplified geometry used in the simulation and the power induced by the beam that was observed experimentally.

3.6 Conclusion

The longitudinal and transverse wake potentials excited by an electron beam in a traveling-wave PBG structure have been simulated using CST Particle Studio. Simulation of a disc-loaded waveguide structure with the same iris geometry shows that the PBG structure can effectively confine the fundamental mode and damp the dipole modes excited by the bunch. While the results presented here are for 7-cell structures, simulations with 6-cell structures have shown excellent agreement with the 7-cell results.

The wake potential impedances for the longitudinal and transverse wakes were calculated from the time-domain wake potentials using Matlab. Numerical filters were used to isolate each mode from the wake potential spectrum. This frequency information was then used to recover the contribution to the wake potential from each mode; this provides the $1/e$ decay distance for each mode.

The modes observed in CST simulations of the PBG structure were confirmed using single-cell eigenmode simulations in HFSS. The single-cell simulations were used to confirm the frequency of the observed mode, and then to provide a Q-factor for that mode for quantitative comparison. These simulations showed reasonable agreement between the decay distances of the wakes observed in the frequency domain (HFSS) and particle-in-cell (CST) simulations for the fundamental mode and the three lowest-frequency dipole-like modes.

The combination of particle-in-cell (CST) and frequency-domain (HFSS) simulations provides an effective method by which to study the wakefield damping in the latest PBG structures. The testing of these structures, e.g. the elliptical-rod PBG

structure tested at SLAC by MIT and described in [7], has focused on achieving the highest gradient possible in a PBG structure. Achieved gradient cannot be easily predicted from simulation, so the use of PIC simulations for wakefield damping allows the experimental efforts to continue to focus on achieved gradient.

The PBG lattice was found to have dipole-like modes with peaks in field amplitude within the lattice, giving rise to three dipole modes which are excited with similar amplitudes over a 4 GHz frequency range in the three-row PBG lattice.

A comparison of the transverse wake potentials of the PBG and DLW structures shows that the PBG structure does not significantly alter the initial excitation of HOMs, based on the initial amplitude of the wake potential, but the PBG does damp the wake potential much faster than the DLW structure. This validates the use of the HOM Q as a design metric for future PBG structures.

In addition to the single bunch simulations used to investigate the wake potential in the PBG structure, a bunch train spaced at the fundamental frequency of the structure was also simulated. This reflects the micro-bunched beam used the MIT experiment to study wakefields in the traveling-wave PBG structure. The full experimental geometry could not be simulated, but the beam loading calculated in the CST simulation agrees with the experimental beam loading.

Chapter 4

Breakdown Structure Design and Modeling

In order to facilitate comparisons of the breakdown rate performance between different structures, a standardized structure design for breakdown testing has been adopted by SLAC and adhered to for testing at MIT. This design allows for rapid testing of a single high gradient cavity of varying geometry and design under nearly identical test conditions. This in turn allows for the direct comparison of results obtained by testing different structures.[1]

4.1 Overview

Structures designed to test the breakdown probability per pulse per meter of structure must be easy to test rapidly, be easily interchangeable even under variations in cavity design, confine the breakdown physics to the variable part of the structure, and do not require access for an electron beam. The axially-powered, single-high-gradient, standing-wave structures designed by SLAC satisfy all of these requirements. The structures are axially powered using a reusable TM_{01} mode launcher designed by SLAC, shown in Fig. 4.1. The SLAC-type mode launchers are driven by an incident TE_{01} mode in rectangular waveguide, either WR-90 for the 11.42 GHz launcher or

[1]Parts of this chapter were adapted from [7].

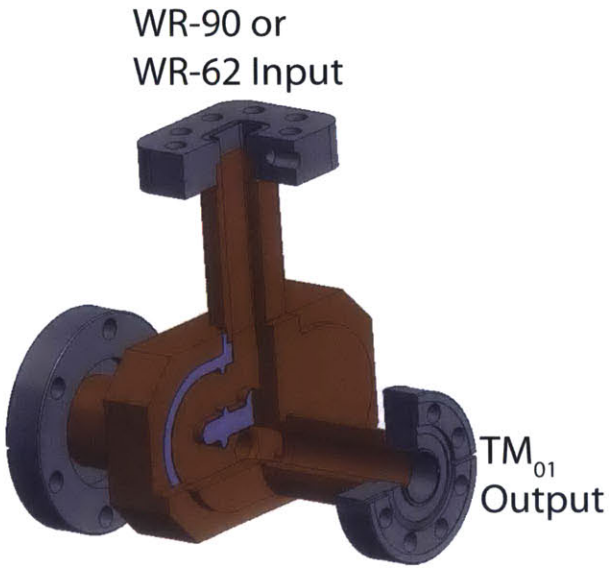

Figure 4-1: Partial section view of the SLAC-type TM_{01} mode launcher. The mode launcher shown here is scaled to 17.14 GHz operation, and therefore has a WR-62 input flange in 0.600 inch diameter output waveguide. The 11.42 GHz launchers have identical internals scaled for the lower frequency and WR-90 input flanges with 0.900 inch diameter output waveguide.

WR-62 for the 17.14 GHz launcher, which is then converted to the TM_{01} mode in cylindrical waveguide with a diameter of either 0.900 or 0.600 inches respectively. At both frequencies the mode launchers couple to the structure with a Pearson's rf flange.

This cylindrical input waveguide is coupled into a three-cell structure through a coupling iris. The high-gradient center cell is designed to have twice the axial electric field amplitude of the coupling cells on either side, which limits breakdowns to the high-gradient cell. The irises coupling the center cell to the coupling cells are fixed for a given design; this makes the center cell and irises effectively part of a periodic accelerator structure of the desired geometry. The two coupling cells and the input coupling iris can be used to tune the frequency and coupling of the structure for breakdown testing, as discussed in Sec. 4.2. The general layout of the breakdown structures is shown in Fig. 4-2.

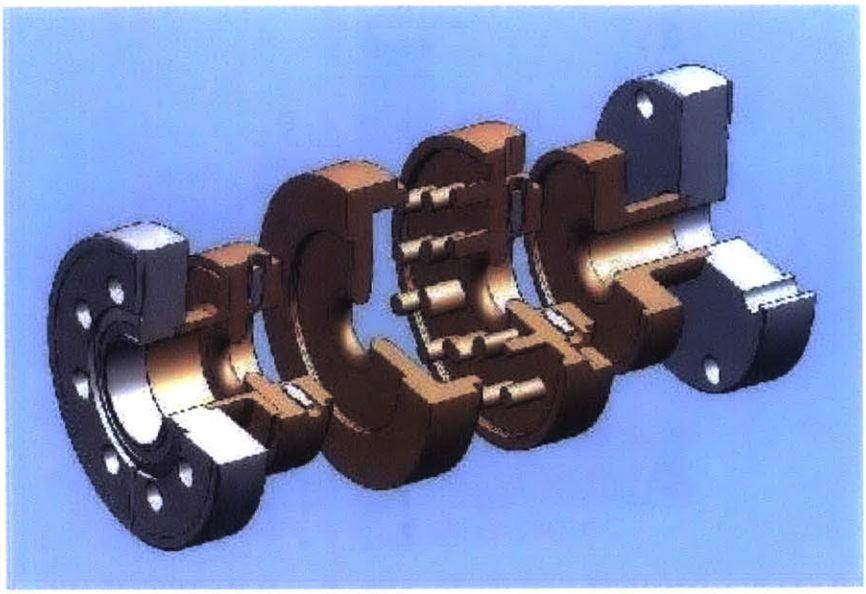

Figure 4-2: Expanded three-quarter view of solid model of elliptical-rod PBG structure, showing two coupling cells and central PBG cell. Power is coupled in from the left.

4.2 Structure Parameters

A significant advantage of the three-cell design is the ease of tuning. For the purposes of this thesis the shape and thickness of all three irises, and the aperture of the high-gradient irises, are kept the same as a known cylindrical-wall structure to which the PBG structures will be compared. The diameter of the input waveguide is fixed to that of the mode launcher being used. The diameter of the output waveguide is chosen such that the accelerator mode is below cutoff, thereby reflecting the mode and forming a standing wave structure. The lengths of the cells are fixed by matching the frequency of the π mode to the frequency of the klystron used for testing, and the radii of curvature in the cells are fixed for ease of fabrication. These parameters are shown in an axisymmetric view, showing the vacuum space of a sample PBG structure, in Fig. 4-3 (A).

When designing the structure the frequency of the π mode and 1:2:1 field amplitude profile are dominated by three tuning parameters: the radius of each of two coupling cells and the aperture of the coupling iris. These tuning parameters of the

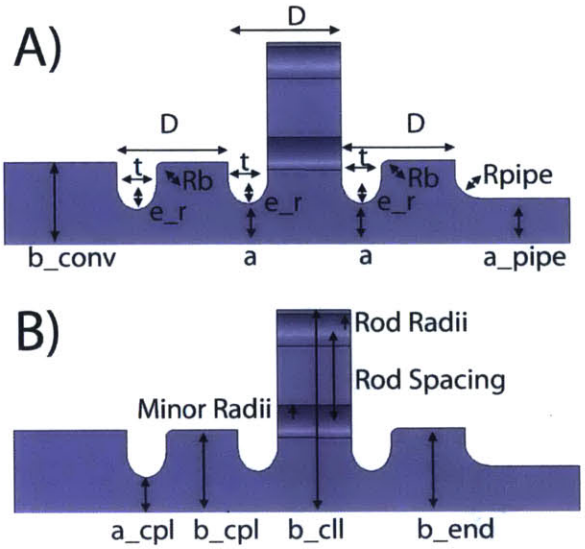

Figure 4-3: Axisymmetric views of the vacuum space of the PBG-E structure showing the fixed parameters, (A), and tuning parameters, (B), for the elliptical-rod PBG structure.

structure are shown in Fig. 4-3 (B). The radii of the input and output coupling cells, b_cpl and b_end respectively, are varied in HFSS simulations to find a field profile on axis with approximately half of the peak field amplitude in the coupling cells relative to the central PBG cell. When needed, the radius to the outer wall of the PBG cell, b_cll, is chosen to allow space between the outer row of rods and the outer wall of the vacuum can. The aperture of the coupling iris, a_cpl, is chosen to achieve critical coupling in the HFSS simulation. Varying a_cpl affects the frequency of the structure so an iterative pocess of tuning the frequency with the cell radii then adjusting the coupling with the iris aperture must be used to keep the resonant frequency of the entire structure as close as possible to the resonant frequency of the PBG lattice, which is tuned to the center frequency of the klystron, either 11.42 GHz or 17.14 GHz.

4.3 Structure Modeling

Electromagnetic modeling of the fields in the structure is a three-step process. All modeling is done using the Ansys code HFSS [25]. This allows the user to define

the vacuum space of the model and simulate the electromagnetic fields in the cavity subject to appropriate boundary conditions.

4.3.1 High-Gradient Cell Design

The first step in the structure modeling process is to design the high-gradient cell. For a cylindrical-wall cavity this amounts to choosing the correct cavity radius. For a photonic band-gap cell the α/β ratio must be chosen, and any perturbations to the lattice, such as elliptical rods, must be included. A two-dimensional TM_{010} mode is then modeled, ignoring the irises and end plates of the cell, to ensure that the lattice supports the design frequency of the final three-cell design as set by the klystron powering the test stand.

4.3.2 Periodic Structure

Given a lattice design and the fixed parameters for the iris aperture, thickness, and curvature from the reference design, the high-gradient cell is fully defined. Because the structure will operate in the standing wave π mode at the center frequency of the klystron the length of the cell is also fixed. This allows a periodic model to be built, extending along the axis from the center of the input iris to the center of the output iris, as seen for one of the SLAC PBG structures, in Fig. 4-4. Periodic boundary conditions requiring the phase advance between the two end planes to be 180 degrees are enforced on the model, and the eigenmode of the structure is determined. Because of the axial confinement in the periodic model the simulated π mode will have a higher frequency than the TM_{010} mode in the lattice simulations.

The π mode of the periodic structure will also have a higher frequency than the π mode in the breakdown tester because the periodic boundary conditions provide stronger axial confinement than seen in the full structure. In the full breakdown test structure the electric field from the high-gradient cell extends a finite distance into the two coupling cells; the on-axis null in the electric field does not correspond to the center of the irises. The periodic structure, in contrast, enforces a null in the

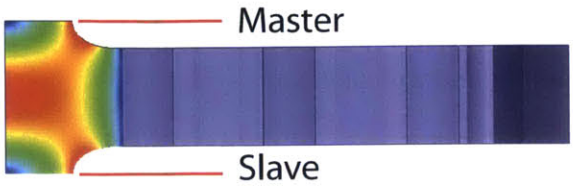

Figure 4-4: Axisymmetric view of the vacuum space of the periodic model showing the electric field amplitude. The phase advance between the master and slave planes is set to 180 degrees. This model is used to calculate the equivalent gradient in the breakdown test structure.

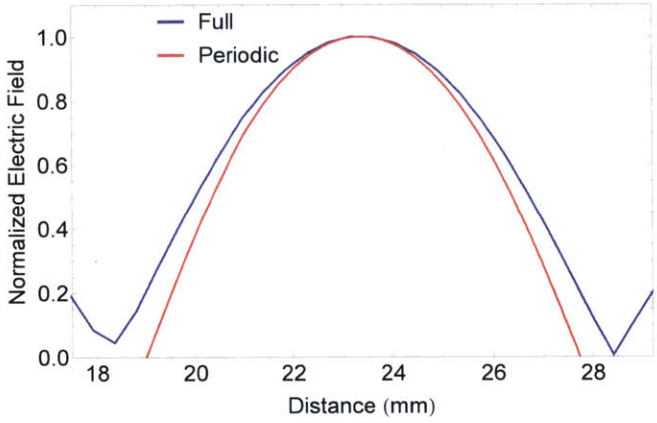

Figure 4-5: Difference in the on-axis electric field in the periodic (red) and full breakdown (blue) structures. The field in the full structure extends into the coupling cells.

electric field at the center of the irises, resulting in an increase in frequency for the π mode. Because the longer effective cavity length in the full structure, as seen in Fig. 4-5, yields an effective gradient higher than what could be achieved in an accelerator application, the periodic model must be used for gradient calculations.

This model simulates the fields in a real accelerating section assuming that a number of high-gradient cells, each with the geometry of the center cell of the breakdown tester, were built; this is referred to as the equivalent accelerator cell. The integrated gradient in this single-cell model is calculated as a fraction of the peak surface electric field. This relationship between gradient and peak surface field is used to provide a calibration between input power and effective gradient in the three-cell structure; this calibration is used in converting measured power levels into cavity fields. Because this periodic simulation will be used in analysis of the experimental data, it should be run

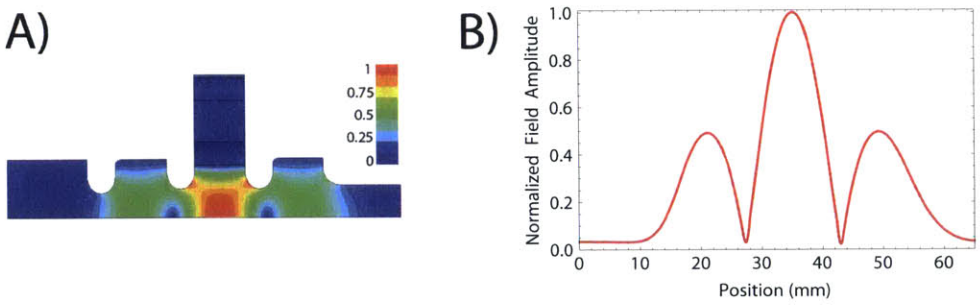

Figure 4-6: Normalized electric field amplitude for an 11.42 GHz standing-wave PBG structure(A) looking at a radial cut of the structure through an inner rod, and (B) along the axis of the structure. This is representative of the desired field profile after structure tuning.

to a high precision, e.g. better than 1 MHz frequency resolution, to ensure accurate analysis.

4.3.3 Breakdown Test Structure

Once the dimensions of the high-gradient cell have been verified and the periodic model has been built the full three-cell breakdown test structure can be designed. This design is most easily completed using a combination of eigenmode and driven modal simulations in HFSS. The final electric field profile of an 11.42 GHz structure after tuning can be seen in Fig. 4-6. The qualitative shape of the field profile is the same at 17.14 GHz.

In eigenmode simulations the tuning parameters b_cpl and b_end are varied to find an eigenmode with the desired frequency and with approximately half the field amplitude in the coupling cells relative to the high-gradient cell. Once these parameters are close a driven modal simulation is used to adjust a_cpl for critical coupling, as evidenced by the S_{11} and Smith chart for the structure. Varying a_cpl has a small effect on the frequency of the eignemode, so b_cpl and b_end must then be varied to return the design to the desired frequency. This process is iterated until a structure with critical coupling and the desired field pattern at the desired frequency is found.

At this point a high-precision driven modal simulation can be run. Because HFSS normalizes driven modal simulations to one Watt of incident power this simulation

can be used to calibrate the field amplitude in the structure. Combining this result with the periodic simulation from earlier a relationship between incident power and effective gradient (i.e. gradient in the periodic structure) can be obtained. Again in order to ensure accurate analysis of experimental data this driven modal simulation needs to be run to high precision.

4.4 Modeling for Data Analysis

The experimental data collected at both SLAC and MIT can only be analyzed using the calibrated simulations discussed in Sec. 4.3. As will be discussed in Chapters 5 and 6, the primary experimental data collected is the power incident on and reflected from the structure. The simulations in Sec. 4.3, however, assume steady-state operation of the structure. In order to accurately model the fields in the structure, which is critical for calculating the peak surface temperature rise, the evolution of the fields in the structure with time is required. This time-dependent behavior is obtained using Fourier transforms by modeling the circuit as a driven resonator and convolving the frequency response of this resonator with the frequency spectrum of the applied rf power.

4.4.1 Resonator Fields

The electric field in a damped oscillator with undamped resonant frequency ω_0 and loaded quality factor Q_L driven at a frequency ω satisfies Eq. (4.1).

$$\frac{d^2E(t)}{dt^2} + \frac{\omega_0}{Q}\frac{dE(t)}{dt} + \omega_0^2 E(t) = Ce^{i\omega t} \tag{4.1}$$

Assuming a solution of the form $E(t) = Ae^{i\omega t}$ for some complex number A gives

$$A = \frac{C}{\omega_0^2 - \omega^2 + \frac{i\omega\omega_0}{Q_L}} \tag{4.2}$$

This is is the steady state amplitude of the electric field in the cavity subject to an

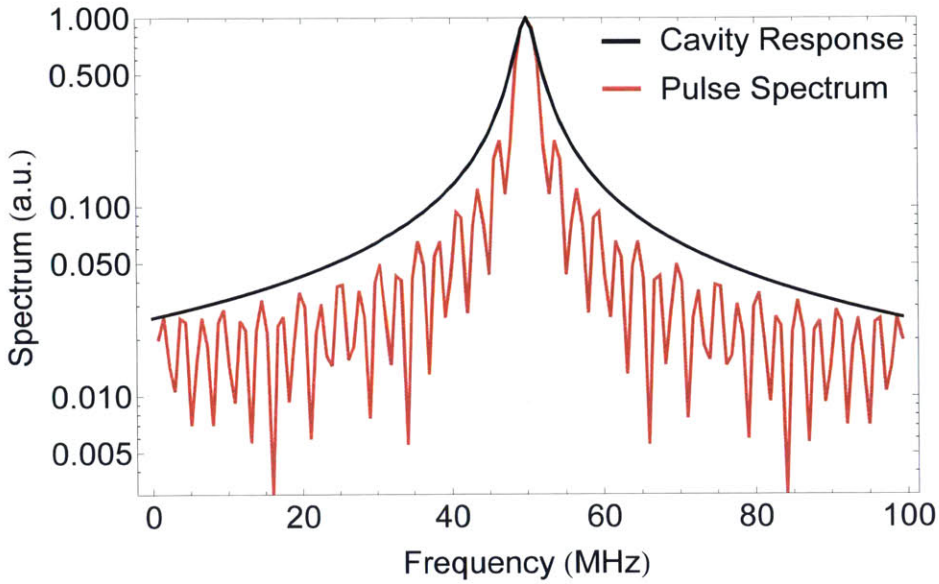

Figure 4-7: The cavity response function (black) and the normalized spectrum of the incident rf pulse (red) are shown as a function of frequency. Both the cavity response and the pulse spectrum have been centered at 50 MHz.

applied electric field with amplitude $|C|$ and frequency ω. This field amplitude is at a maximum when $\omega = \omega_0$, with a maximum amplitude of $|A|_{max} = CQ_L/\omega_0^2$. Because the calibrated simulations give the steady state field amplitudes for a given input power, the relevant parameter in the data analysis is the fraction of the field in the cavity as a function of frequency, i.e. $A/|A|_{max}$, which is given by Eq. (4.3) where ω has been replaced by the real frequency f.

$$\frac{A(f)}{|A|_{max}} = \frac{f_0^2}{Q_L} \frac{1}{f_0^2 - f^2 + \frac{if f_0}{Q_L}} \tag{4.3}$$

This cavity response, $\frac{A(f)}{|A|_{max}}$, is shown in Fig. 4-7, where it is plotted along with the frequency spectrum of an artificial power pulse. The cavity response can be convolved with the frequency spectrum of the fields applied to the cavity to obtain the fields in the cavity.

4.4.2 Pulse Fields

As mentioned previously, the measurement systems used in the experiments to be presented in this thesis measure the power applied to the cavity. In order to convert this into a field an rf signal of the form $\hat{E}(t) = e^{i2\pi ft}$ is multiplied by the square root of the measured rf power trace, resulting in $E(t) = \sqrt{P(t)}e^{i2\pi ft}$. This creates an artificial signal that is equivalent to heterodyne detection of the incident rf pulse resulting in an intermediate frequency (IF) f. The Fourier transform of this artificial field pulse gives the frequency spectrum of the applied rf which can be convolved with the frequency response for the cavity found in 4.4.1.

Because this artificial signal is being recreated from the video signal recorded by either the power meter, at 11.42 GHz, or the diode, at 17.14 GHz, f must be small enough to ensure that the sampling rate of the measurement system satisfies the Nyquist sampling theorem. In the case of the power meter the sampling rate is 100 MHz, and an effective IF of 30 MHz is used. At 17.14 GHz the diode signals are detected using a 350 MHz oscilloscope and an effective IF of 100 MHz is used. As part of the experimental procedure the cavities will be tested on-resonance, therefore the applied rf can be modelled as having a frequency f_{IF} and the cavity response function can be shifted to be centered at f_{IF}. Mathematically this is accounted for in the cavity response by taking $\tilde{f} = f + f_{shift}$ with $f_{shift} = f_0 - f_{IF}$ and evaluating $\tilde{f}$ over the range of frequencies found in the Fourier spectrum of the artificial field pulse.

4.4.3 Cavity Fields

Given the cavity response $A(\omega)$ and the applied electric field $E_{rf}(t)$ with Fourier transform $\tilde{E}_{rf}(\omega)$, the complex fields in the cavity as a function of time can be found using Eq. (4.4).

$$E_{cav}(t) = \int_{-\infty}^{\infty} A^*(f)\tilde{E}_{rf}(f)df \tag{4.4}$$

From here the real power in the cavity as a function of time, $P_{cav}(t)$, is simply given by $P_{cav}(t) = |E_{cav}(t)|^2$. This in turn gives the real electric and magnetic fields and

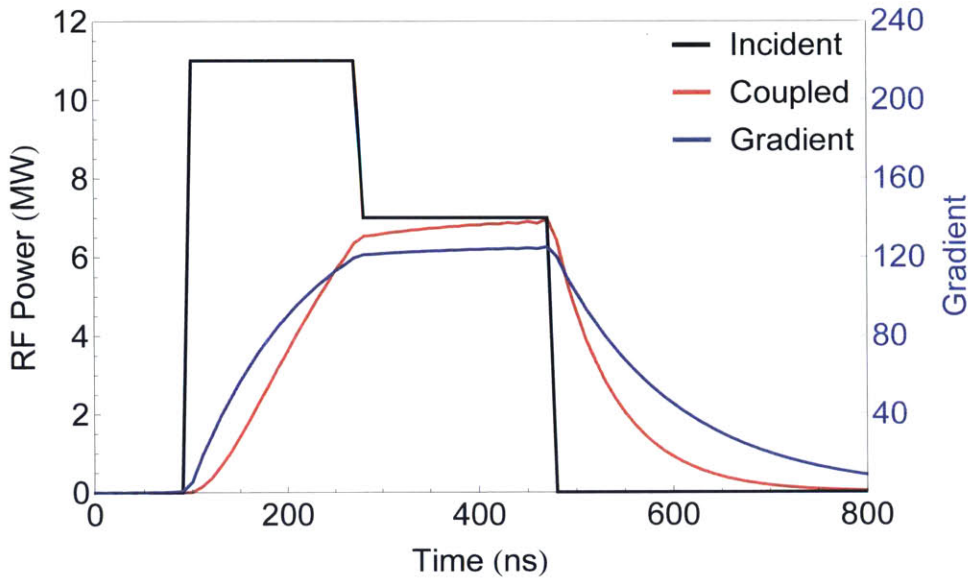

Figure 4-8: This shows the result of analysis of a representative incident rf pulse, shown in black. The power coupled into the structure, shown in red, and the gradient in the structure, shown in blue on the right axis, have been calculated using the frequency-space technique discussed in this section.

gradient in the structure as a function of time via the calibrated simulations. Once the fields in the structure have been calculated, the analysis code written in Mathematica [44] calculates the pulse length, average power, average gradient, and pulsed heating values for each pulse, which simplifies the later analysis of the breakdown statistics.

An artificial power pulse with analysis is shown in Fig. 4-8. The shows a stepped pulse typical of testing at SLAC, as well as the power coupled into the structure and the gradient as a function of time.

Chapter 5

Experimental Testing at 11 GHz

5.1 Introduction

In order to investigate the high-gradient operation of a photonic band-gap structure for accelerator applications, and as part of an ongoing program of high-gradient breakdown probability testing of standing wave structures at SLAC National Accelerator Laboratory, a round-rod PBG structure was tested at SLAC. The purpose of this test was to determine the breakdown probability performance of the structure under high-gradient operation; the results of this initial test were presented in [12]. This initial experiment revealed that high surface temperature rise early in testing degraded the performance of the round rod PBG structure. An improved PBG design was made based on results of this initial high gradient, high repetition rate testing of a PBG structure [28]. The results of this improved design, motivation for the specific changes used in testing of the improved designs, and results of that testing are presented in this chapter.[1]

The improved PBG design changes the shape of the rods immediately surrounding the defect region to reduce the peak surface magnetic field in the structure; this reduces pulsed heating and cyclic fatigue, which improved structure performance. The improved lattice has been incorporated into a single-cell standing wave structure for high-gradient high repetition rate testing at SLAC, a model of which is depicted

[1]This chapter was adapted from [7].

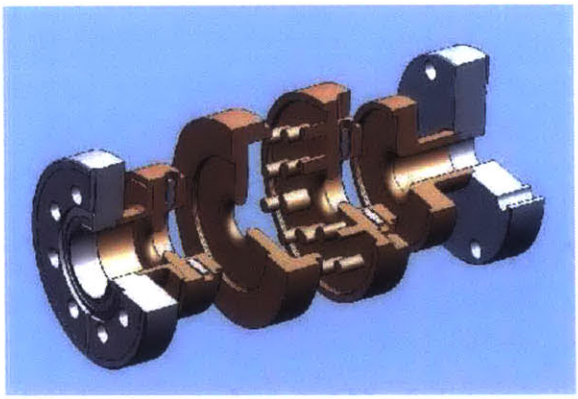

Figure 5-1: Expanded three-quarter view of solid model of elliptical-rod PBG structure, showing two coupling cells and central PBG cell. Power is coupled in from the left.

in Fig. 5-1. This structure follows the general design used extensively in previous SLAC single-cell standing wave structure testing [45, 46, 47, 48, 49, 50, 51, 52, 53]. The structure is designed with a matching cell on either side of a single PBG test cell. The structure is designed to have the highest electric and magnetic fields in the test cell and significantly reduced fields in the matching cells. The matching cells have solid cylindrical walls instead of PBG rods. The structure is axially powered via a reusable TM_{01} mode launcher [54], which remains with the structure for the duration of all cold and hot tests; this mode launcher design has been thoroughly tested in previous experiments.

5.2 Design of Photonic Band-gap (PBG) Structure

The structure was designed to be directly comparable to the original high-gradient round-rod PBG structure, SLAC designation 1C-SW-A5.65-T4.6-PBG-Cu and referred to here as PBG-R [12], and a disc-loaded waveguide structure fabricated at INFN-Frascati and tested at SLAC [55], SLAC designation 1C-SW-A5.65-T4.6-Cu, referred to here as DLWG . The SLAC designations indicate a single high-gradient cell, 1C, standing wave, SW, structure with an iris aperture of 5.65 mm, A5.65, and

iris thickness of 4.6 mm, T4.6, made out of copper, Cu. To this end, all three structures have irises with elliptical cross-sections to reduce the peak surface electric field, and the same iris aperture and thickness for the irises on either side of the high-field cell. With these parameters fixed, the PBG cell parameters, the aperture of the coupling iris, and the radii of the coupling cells were left as design variables.

The PBG-E lattice has two main variations when compared to the lattice of the PBG-R structure. The most significant variation is the use of elliptical rods for the inner row of the structure, keeping the outer rods circular. Making the rods elliptical reduces the peak surface magnetic field on the rod, thereby reducing peak surface temperature rise; the field is much lower on the outer rods, making modification of these rods unnecessary. The lattice used in the elliptical-rod structure is shown in Fig. 5-3. The same lattice parameter of $\alpha/\beta = 0.18$ is used for both the PBG-E and PBG-R structures [12]. In the elliptical-rod lattice the minor radius of the elliptical rods is kept the same as the radii of the round rods. The major radius is chosen to be 1.5 times the minor radius. This ratio of major to minor radius for the elliptical rods represents a trade-off between increasing the ratio of peak surface electric field to peak surface magnetic field, a measure of peak surface temperature rise at a given gradient, and keeping the Q-value of the TM_{11} mode low, as reported in [28].

The other significant change in the PBG-E cell design is the use of only two rows of rods as opposed to the three rows used in the PBG-R structure, making fabrication easier. In the absence of an outer wall, the number of rows of rods in the structure determines the diffractive Q-value of the modes. This Q increases with the number of rows of rods. When a solid outer wall is present, as is required for vacuum purposes in the SLAC design, the diffractive Q also increases, allowing the use of two rows of rods without a decrease in total Q of the mode. A minimum of two rows of rods are required for proper confinement of the fundamental mode.

5.2.1 Structure Tuning

In addition to the iris geometry, various other structure parameters are fixed by the frequency of the experiment and the geometry of the SLAC mode launchers being

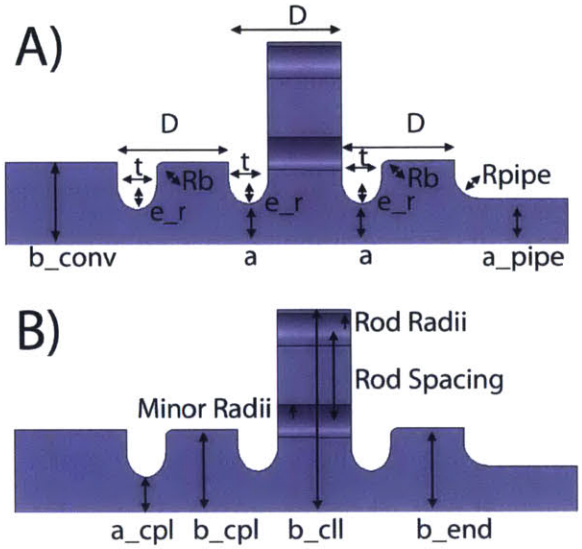

Figure 5-2: Axisymmetric views of the vacuum space of the PBG-E structure showing the fixed parameters, (A), and tuning parameters, (B), for the elliptical-rod PBG structure.

used. These parameters are shown in an axisymmetric view, showing the vacuum space of the structure, in Fig. 5-2 (A), and listed in Table 5.1.

The tuning parameters of the structure are shown in Fig. 5-2 (B). The radii of the input and output coupling cells, b_cpl and b_end respectively, are varied in HFSS simulations to find a field profile on axis with approximately half of the peak field amplitude in the coupling cells relative to the central PBG cell. The radius to the outer wall of the PBG cell, b_cll, is chosen to allow space between the outer row of

Table 5.1: Fixed parameters for PBG-E structure. Final design values for Fig. 5-2 (A).

Fixed Parameters	
Rpipe	3.0 mm
Rb	1.0 mm
t	4.6 mm
e_r	3.4 mm
D	13.12 mm
a	5.65 mm
a_pipe	6.35 mm
b_conv	11.43 mm

Table 5.2: Tuning parameters for PBG-E structure. Final design values for Fig. 5-2 (B).

Tuning Parameters	
a_cpl	4.83 mm
b_cpl	11.44 mm
b_cll	28.0 mm
b_end	11.63 mm
Minor Radii (α)	2.27 mm
Major Radii (δ)	3.40 mm
Rod Spacing (β)	12.59 mm

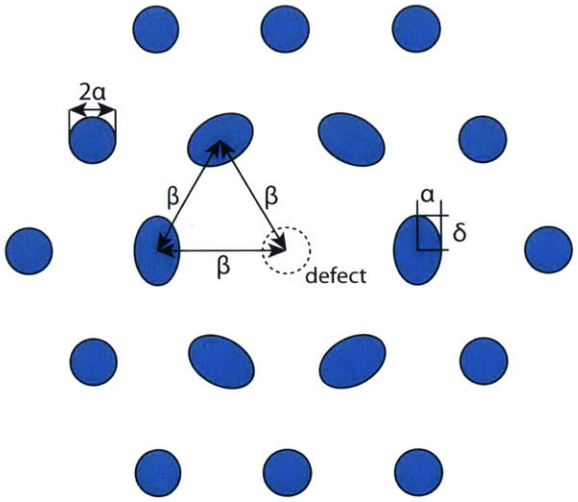

Figure 5-3: Elliptical-rod PBG lattice showing lattice spacing, β, rod radius (minor radius for elliptical rods), α, and major radius, δ.

rods and the outer wall of the vacuum can. The aperture of the coupling iris, a_cpl, is chosen to achieve critical coupling in the HFSS simulation. All three parameters a_cpl, b_cpl, and b_end affect the frequency of the structure, and must be adjusted to keep the resonant frequency of the entire structure as close as possible to the resonant frequency of the PBG cell, which is tuned to the center frequency of the klystron, 11.424 GHz. The final design values for the tuning parameters are given in Table 5.2.

5.2.2 PBG Cell Design

In the three-cell design used for this and previous high-gradient structure testing (e.g. [51]), the central cell is designed to have twice the on-axis electric field magnitude of the coupling cells on either side. This requires a PBG cell which strongly confines a TM_{01} accelerating mode at a frequency of 11.424 GHz. Critical coupling into the entire structure is also required.

The PBG-E lattice has two main variations when compared to the lattice of the PBG-R structure. The most significant variation is the use of elliptical rods for the inner row of the structure, keeping the outer rods circular. Making the rods elliptical reduces the peak surface magnetic field on the rod, thereby reducing peak surface temperature rise; the field is much lower on the outer rods, making modification of these rods unnecessary. The lattice used in the elliptical-rod structure is shown in Fig. 5-3. The same lattice parameter of $\alpha/\beta = 0.18$ is used for both the PBG-E and PBG-R structures [12]. In the elliptical-rod lattice the minor radius of the elliptical rods is kept the same as the radii of the round rods. The major radius is chosen to be 1.5 times the minor radius. This ratio of major to minor radius for the elliptical rods represents a trade-off between increasing the ratio of peak surface electric field to peak surface magnetic field, a measure of peak surface temperature rise at a given gradient, and keeping the Q-value of the TM_{11} mode low, as reported in [28].

The other significant change in the PBG-E cell design is the use of only two rows of rods as opposed to the three rows used in the PBG-R structure, making fabrication easier. In the absence of an outer wall, the number of rows of rods in the structure determines the diffractive Q-value of the modes. This Q increases with the number of rows of rods. When a solid outer wall is present, as is required for vacuum purposes in the SLAC design, the diffractive Q also increases, allowing the use of two rows of rods without a decrease in total Q of the mode. A minimum of two rows of rods are required for proper confinement of the fundamental mode.

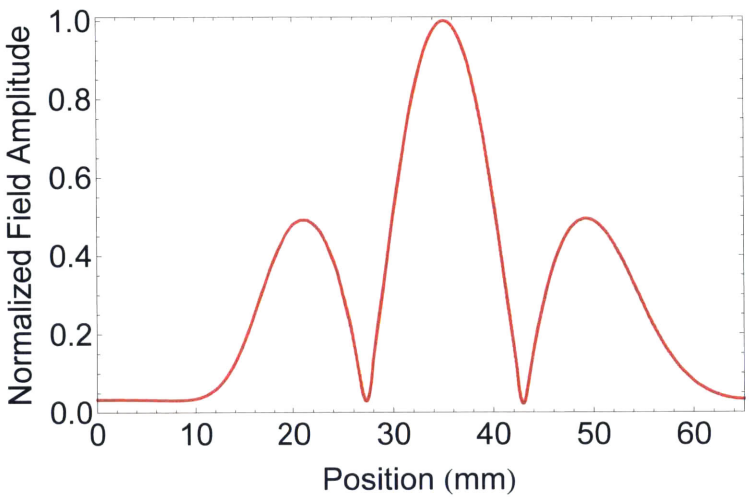

Figure 5-4: Normalized electric field profile on axis in PBG-E structure; the field amplitude in each coupling cell is approximately half that in the PBG cell.

5.2.3 Design Results

The elliptical-rod PBG test structure, PBG-E, was designed using HFSS [25]. The field amplitude on axis for the structure is shown in Fig. 5-4, showing the 1:2:1 relationship between the field amplitudes in the cells. The reflection from the cavity as a function of frequency (S_{11}) is shown in Fig. 5-5, showing that a π mode minimum reflection of -49 dB is achieved at 11.427 GHz; this is sufficiently close to the center frequency of the klystron for testing.

Field plots for the final design are shown in Fig. 5-6 and Fig. 5-7 in a cutaway view through an inner rod and top-down view, respectively. In the cutaway view the 1:2:1 relationship in electric field value can be seen, as well as the increase in surface electric field on the irises. This view also shows the localization of the magnetic field to the defect-facing side of the inner rods. The top-down view shows the uniformity of the accelerating field in the defect region, and the distribution of the magnetic field across the defect-facing side of the inner rod.

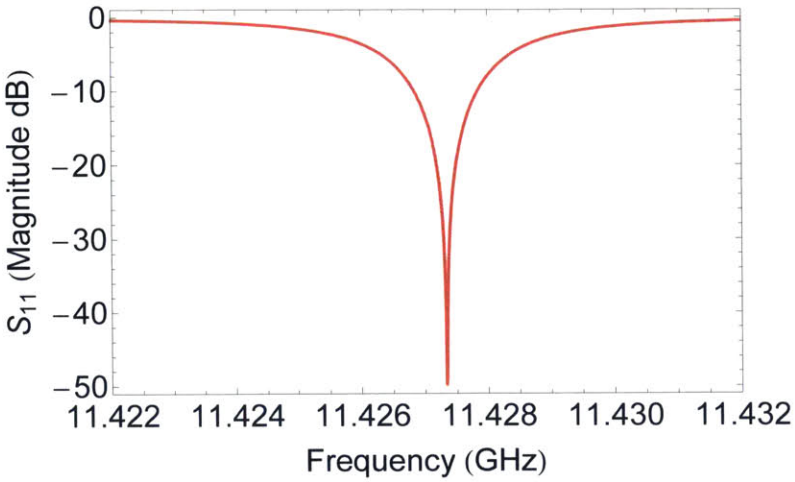

Figure 5-5: Calculated reflection as a function of frequency for the PBG-E structure.

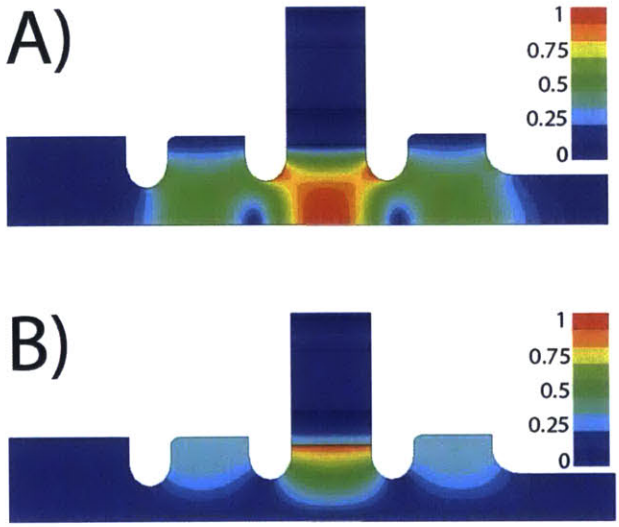

Figure 5-6: Electric (A) and magnetic (B) field amplitudes looking at a radial cut of the structure through an inner rod. At an accelerating gradient of 100 MV/m the peak surface electric field amplitude is 207 MV/m at the iris surfaces. At the same gradient the peak surface magnetic field occurs on the inner surface of the inner rod, and reaches a value of 713 kA/m.

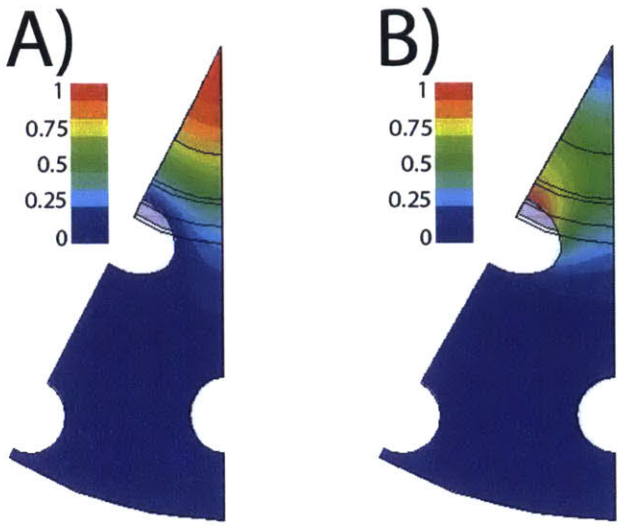

Figure 5-7: Electric (A) and magnetic (B) field amplitudes looking at top-down view of the structure. The peak surface electric field of 207 MV/m for a 100 MV/m accelerating gradient is seen on-axis. The peak surface magnetic field of 713 kA/m for an accelerating gradient of 100 MV/m is confined to the center of the inner surface of the innermost rod.

5.2.4 HFSS Simulations for Data Analysis

The data collected during experimental operation is in the form of number of breakdowns versus power incident on the structure. In order to translate this data into breakdown probabilities as a function of field parameters, such as gradient or peak surface temperature rise, calibrations between input power and field must be made. This can be done using driven simulations in HFSS, which allow the user to specify the frequency or frequencies of the simulation as well as the input power at the input port. To calculate the gradient and shunt impedance an eigenmode model of the central PBG cell is simulated with a phase advance of 180 degrees across the cell. The integrated gradient in this single-cell model is calculated as a fraction of the peak axial electric field. This relationship between gradient and peak surface field is used to provide a calibration between input power and effective gradient in the three-cell structure; this calibration is used in the analysis of the experimental data. For the elliptical-rod PBG structure the structure achieves 100 MV/m gradient at 4.4 MW. The fields in the structure scale as the square root of the input power, so this result

Table 5.3: Surface field values from HFSS simulations for PBG-E structure, PBG-R structure, and disc-loaded waveguide structure. The shunt impedance calculated here is for a periodic π mode structure; i.e. a structure composed of iterations of the central cell of the three-cell structures tested.

Structure	PBG-E	PBG-R	DLWG
Power	4.4 MW	5.9 MW	3.9 MW
Gradient	100 MV/m	100 MV/m	100 MV/m
Q_0 (measured)	7792	7401	8870
r_{sh}	37 MΩ/m	36 MΩ/m	51 MΩ/m
Peak surface E field	207 MV/m	208 MV/m	211 MV/m
Peak surface H field	713 kA/m	890 kA/m	418 kA/m

can be used to find the field values at any input power. The surface fields at 100 MV/m gradient for both PBG structures and the equivalent disc-loaded waveguide structure are given in Table 5.3.

5.2.5 Surface Temperature Rise Calculation

The elliptical-rod PBG structure was designed with a goal of reducing the peak surface magnetic field, which causes surface temperature rise via ohmic heating. This heating cannot be measured experimentally, but can be predicted mathematically using Eq. (5.1) [20].

$$\Delta T = \frac{1}{\rho c_\epsilon \sqrt{\pi \alpha_d}} \int_0^t \frac{1}{\sqrt{t-t'}} \frac{1}{2} R_S \left| H(t') \right|^2 dt' \tag{5.1}$$

Equation (5.1) relates the surface temperature rise, ΔT, to the surface magnetic field as a function of time, $H(t')$, using the density, ρ, specific heat at constant strain, c_ϵ, thermal diffusivity, α_d, and surface resistance, R_S. This equation can be used with a model of the real pulse shape to predict the temperature rise prior to high-power testing, which can be used to limit the power applied to the structure. A comparison of the calculated peak surface temperature rise for the two PBG structures, given a pulse with a 180 ns filling portion and 150 ns flat top at 100 MV/m gradient is given in Table 5.4.

Table 5.4: Calculated peak surface temperature rise for both PBG structures at 100 MV/m accelerating gradient

Structure	Temp. Rise (K)
PBG-R	131
PBG-E	84

5.3 Cold Test

The initial cold test and final tuning of the elliptical-rod PBG structure were done using the same TM_{01} mode launcher used for the high power testing and post-operation cold test. A vector network analyzer (VNA) was connected to the rectangular waveguide input of the launcher and used to measure the complex reflection from the structure. All cold testing was done with a dry nitrogen flow through the structure to maintain structure cleanliness. The temperature of the structure was monitored via a thermocouple attached to the structure body.

The structure is tuned via four tuning studs in each matching cell, allowing the radius of the cells to be perturbed. The structure is tuned to produce the desired 1:2:1 field profile in addition to minimizing the S_{11} of the π mode. The final observed frequency of the π mode of the structure is 11.440 GHz, which is within the acceptable tuning range of the klystron. This frequency shift is likely due to large braze fillets around the rod ends, which was introduced to correct problems with the rod braze joints in the PBG-R structure; this large fillet is visualized in the autopsy of the structure.

After the structure is tuned the field profile is measured using a non-resonant perturbation technique [56, 57, 58]. The perturbing object is a small dielectric "bead" on a thin dielectric wire, which is suspended in the structure via a pulley assembly mounted to the top of the structure. The wire used is Ashaway 10/0 black monofilament micro suture thread and the bead is a small drop of super glue.

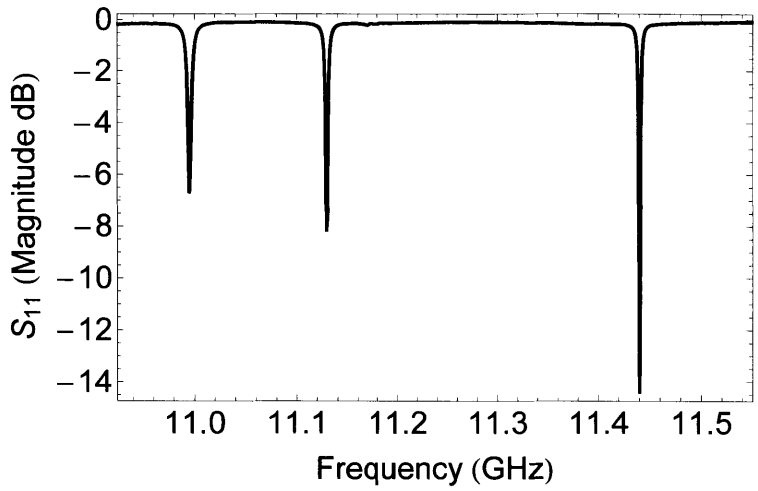

Figure 5-8: S_{11} of PBG-E structure, showing resonances for, in order of increasing frequency, the 0 mode, the $\pi/2$ mode, and the π mode.

5.3.1 Bead Pull Measurements

The PBG structure supports multiple modes depending on the phase advance between the cells. The frequencies of these modes can be found by measuring the S_{11} of the structure in the absence of any perturbing elements, as seen in Fig. 5-8. The modes can be identified by their field patterns, which are found by moving the bead through the full length of the structure and measuring the real and imaginary reflection on or near resonance as a function of axial distance.

Three structure modes were identified, the 0 mode, the $\pi/2$ mode, and the π mode. The structure is designed to operate in the π mode, so it is of primary importance for the axial field profile of this mode to match the design. Good agreement between the design and measured field was found in the test and matching cells as shown in Fig. 5-9.

5.3.2 Coupling and Q

Using the S_{11} measurement the resonant frequency, coupling, and mode Q values can be determined for each structure mode [59]. The unloaded Q, Q_0, and external Q, Q_{ext}, can be measured directly from the Smith chart. These are then used to calculate

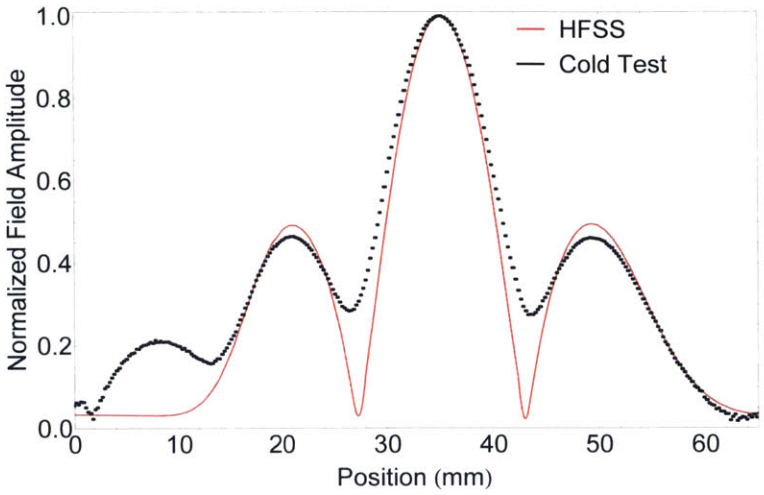

Figure 5-9: π mode field profile

Table 5.5: Q values for the various structure modes

Mode	Frequency (GHz)	Q		
		Q_0	Q_{ext}	Q_L
0	10.995	9057	3058	2286
$\pi/2$	11.129	9319	5304	3380
π	11.440	7792	10290	4434

the loaded Q, Q_L, via $1/Q_L = 1/Q_0 + 1/Q_{ext}$. These values are summarized in Table 5.5.

5.4 Experimental Setup

The PBG structure was tested at the SLAC National Accelerator Laboratory, using the X-band klystron XL4-6B. This klystron is controlled by a computer system, which allows the use of shaped pulses as well as controlling the power and frequency of the rf on a shot to shot basis. The power at the klystron is measured with an Agilent 8990 A peak power meter, and the power incident on and reflected by the structure is measured with an Agilent N-1912A peak power meter; traces from both power meters are recorded every two seconds. The filling of the standing wave structure is done using a shaped pulse with a higher-power portion filling the structure rapidly, after

which the power decreases to maintain a constant power coupled into the structure for the duration of the pulse; the quoted pulse power and pulse length reflect this constant-power portion of the pulse. The control system monitors the power and frequency of the applied rf and makes changes as needed. The structure is cooled via external water flow in a copper jacket which keeps the frequency shift at the few megahertz level, well within the bandwidth of the klystron. In addition to the peak power meters, there are crystal detectors on both the forward and reflected power signals, current monitors measuring the current in each direction, and an ion gauge measuring structure pressure. A log is kept for the test stand, providing records of the operating conditions and testing goals for the current experiment.

During testing two distinct sets of data are recorded by microwave diagnostics. The peak power meters record the klystron, forward, and reflected power every two seconds while the system is operating. The current monitors' signals are measured by an oscilloscope and used to determine when a breakdown has occurred. When a breakdown is detected, based on the magnitude of the current monitor signal, the forward power crystal signal, reflected power crystal signal, forward current monitor signal, and reverse current monitor signal are recorded for that trace and the trace immediately before the breakdown was detected. This provides a fast way of counting the number of breakdowns during testing, and the forward and reverse crystal signals provide a monitor of the microwave pulses. A schematic of the diagnostic setup is shown in Fig. 5-10.

5.5 Testing Methodology

5.5.1 Experience with First PBG Structure

A PBG structure with only round rods, PBG-R, was tested at SLAC with the standard SLAC testing methodology, as reported in [12]. The goal of this standard methodology is to collect systematic and reproducible data as fast as is practical. To this end the structures are typically exposed to very high power at low pulse

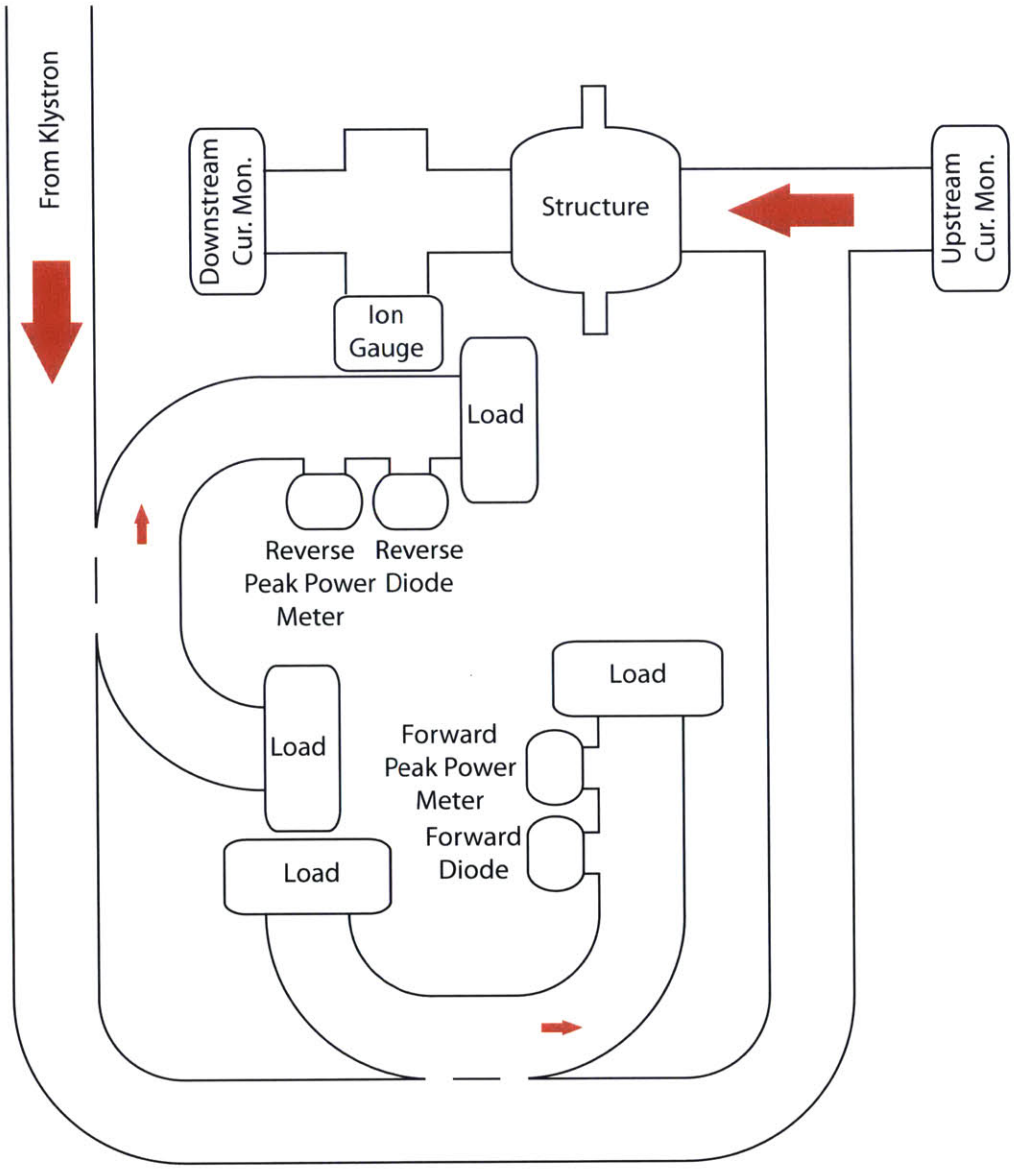

Figure 5-10: This shows a rough schematic view of the diagnostics available during breakdown testing at SLAC.

length early in the testing. This produces a large number of breakdowns in a short time, and is intended to process the surface in a minimal amount of time. After this initial processing phase, in which many hundreds or thousands of breakdowns may occur, the structure is operated at lower breakdown rates, with the goal of producing data sets which show a linear relationship between accumulated breakdowns and time. By taking data at different power levels and pulse lengths it is possible to generate plots showing breakdown probability as a function of gradient or pulsed heating. This methodology has been applied to many disc-loaded waveguide-type structures and produced repeatable results showing no degradation in structure performance during testing. Use of this protocol with a structure with very high peak surface temperature rise, such as the PBG-R structure, may have degraded the performance of the structure very early in the testing.

Contrary to previous tests of conventional structures, the post-testing autopsy of the PBG-R structure showed no damage at high electric field locations. Damage was instead seen at high magnetic field locations. This indicates that the breakdowns that occurred in the PBG-R structure were qualitatively different from those seen in previous high-gradient structure tests conducted at SLAC. It is therefore likely that use of the testing methodology normally used at SLAC, which results in the accumulation of a large number of breakdowns early in the testing, caused an irrevocable degradation of the performance of the PBG-R structure very early in the testing.

The hypothesis that the PBG-R structure was damaged early in testing is supported by calculated pulsed heating temperature rise for the PBG-R structure (Fig. 5-11), indicating extremely high surface temperature rises well above the "safe" limit of 50 K [21] early in the processing.

Another possible source of degraded performance in the PBG-R structure is the poor braze connections between the rods and the copper end plate, as seen in post-testing SEM imaging. These braze joints resulted in a negative curvature region at the brazed end of the rod (as opposed to a positive-curvature fillet as intended). Such regions can increase the breakdown probability in several ways, including trapping pockets of gas and supporting multipactoring. Because the damage to the PBG-R

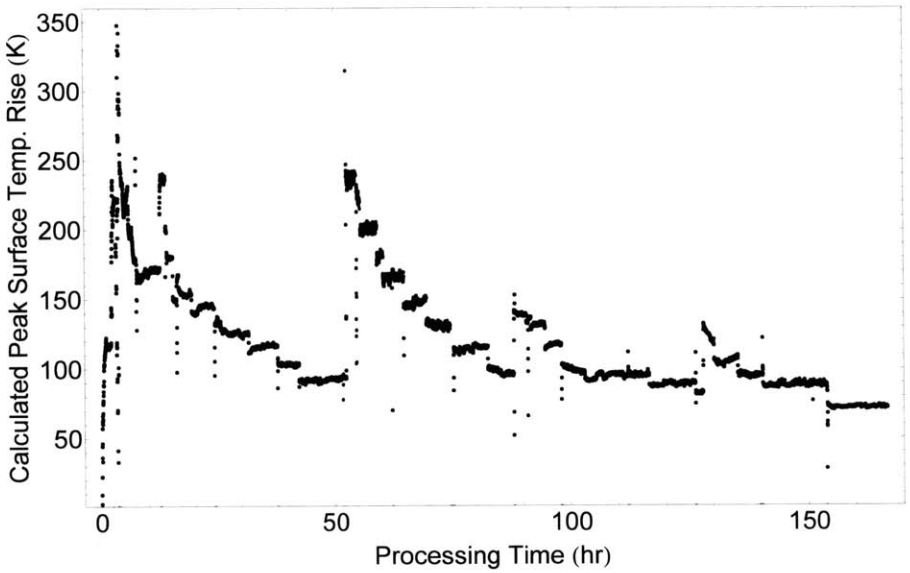

Figure 5-11: Calculated peak surface temperature rise due to pulsed heating in the PBG-R structure. Note the excursions to over 200 K early in the testing.

rods looks uniform along the length of the rod it is unlikely that the poor braze joint is the sole cause of the decreased performance observed in the PBG-R structure, although it may have contributed. The brazing technique was modified for the PBG-E structure to avoid negative curvature regions, resulting in larger-than-intended fillets at the brazed end of the rods.

5.5.2 Revised Testing Methodology

The goal of the revised testing methodology was to show that PBG-type structures can operate at high gradients and low breakdown probability simultaneously. This means that any performance degradation early in testing, as may have occurred in the PBG-R testing, should be avoided. This was done by using a testing methodology for the PBG-E structure that limited both the calculated pulsed heating and the breakdown rate. The calculated pulsed heating was limited to 150 K and the breakdown rate was limited to a steady state rate of 10 per hour. This methodology better protects the structure from damage, but significantly increases the duration of the testing, because a comparable number of breakdowns must be accumulated for each structure. Because

of power level and performance fluctuations on a day-to-day basis, each breakdown probability must be calculated from a single day. Each day is limited to a run time of approximately 14 hours, and approximately 10 breakdowns are needed in a data set to achieve reasonable error bars. This limits the practical breakdown rate to a rate of at least 1 per hour. The imposed upper limit of 10 breakdowns per hour for structure protection means that data can only be taken over one order of magnitude in breakdown probability; this is a necessary and acceptable consequence of protecting the structure.

5.6 Data Analysis

The critical data for analysis of the structure performance is stored in the oscilloscope and peak power meter traces; this data must be analyzed to determine the gradient and pulsed heating at which breakdowns occurred. Breakdowns are counted by looking at the current monitor channels of the scope data sets. Using the time stamps on these files, breakdowns can be correlated with precise power and pulse length information from the peak power meter data sets. The power level and pulse length from the peak power meter is then translated into structure fields using calibrated HFSS simulations. The analysis for both scope and peak power meter data was done using Wolfram MATHEMATICA [44]. Data from both the baseline disc-loaded waveguide structure (1C-SW-A5.65-T4.6-Cu, [49]) and the PBG-R structure (1C-SW-A5.65-T4.6-PBG-Cu, [12]) were re-analyzed using the same algorithms as the PBG-E structure (1C-SW-A5.65-T4.6-PBG2-SLAC-Cu) to ensure consistency between results.

5.6.1 Scope Traces

The scope traces contain both uncalibrated forward and reflected power information and the forward and reverse current monitor signals. A sample set of scope traces showing a shot without a breakdown is shown in Fig. 5-12. The next shot, on which a breakdown occurred, is shown in Fig. 5-13; the breakdown can be identified by the

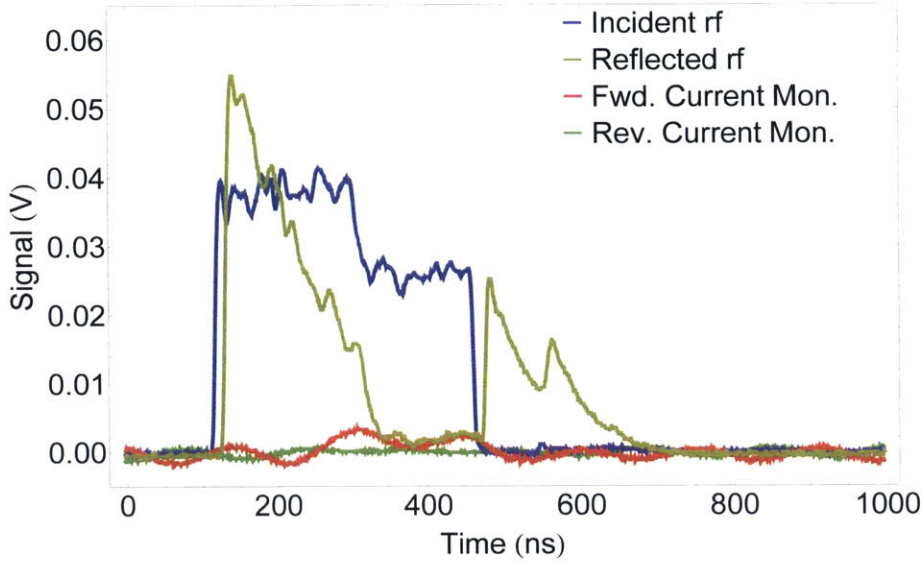

Figure 5-12: A sample set of scope traces showing a normal shot. This is a 150 ns shot at approximately 125 MV/m gradient. The measured incident rf signal is shown in blue, and the measured reflected rf signal is shown in yellow. The forward and reverse current monitor signals are shown in red and green respectively.

spike in both current monitor signals. An increase in the reflected power can also be seen.

The computer system records every shot where there is a breakdown, as well as the shot before, triggered based on the level of the current monitor signals. This means that in post-processing the breakdown shots must be separated from the non-breakdown shots to allow for accurate counting of the accumulated breakdowns. This is done using a MATHEMATICA program which generates a set of data containing the time for each breakdown and the accumulated number of breakdowns for all the testing up to that time. Because the system fires at 60 Hz, secondary breakdowns, i.e. breakdown shots immediately preceded by a breakdown shot instead of a normal shot, can be identified by looking at the time interval between breakdowns.

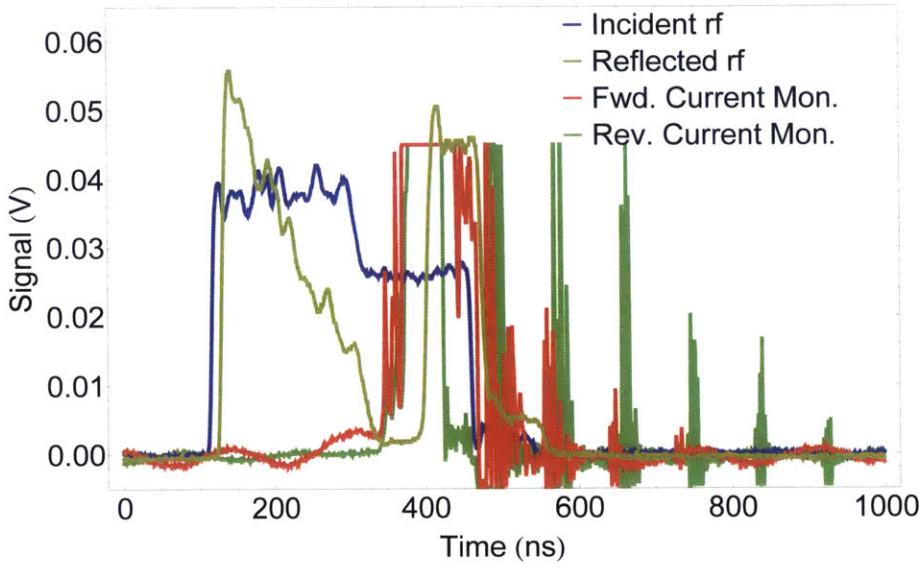

Figure 5-13: A sample set of scope traces showing a breakdown shot, as indicated by the peaks in the current monitor signals, and an increase in reflected rf signal. This is a 150 ns shot at approximately 125 MV/m gradient. The measured incident power is shown in blue, and the measured reflected power is shown in yellow. The forward and reverse current monitor signals are shown in red and green respectively. Note that the currents generated by the breakdowns saturate the current monitors.

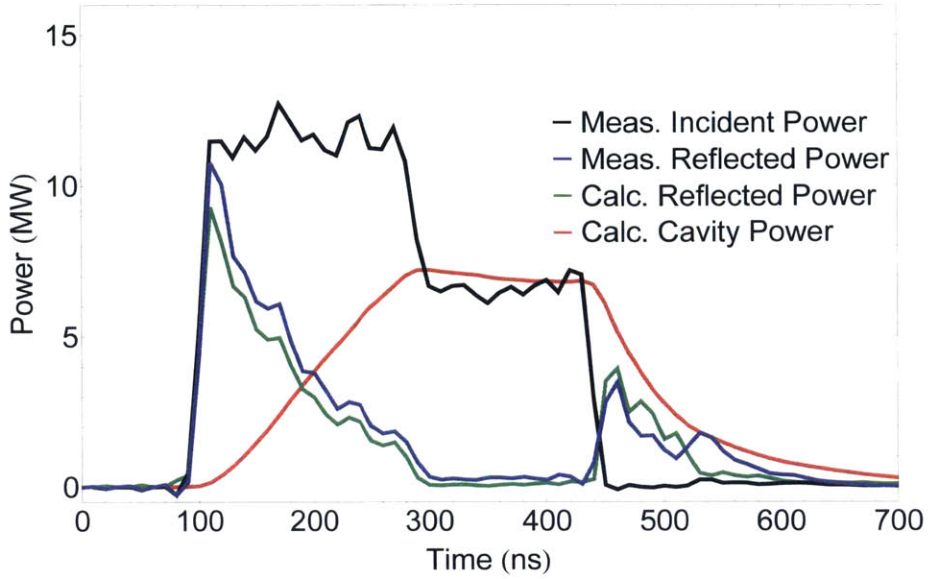

Figure 5-14: Sample traces from the peak power meter for a 150 ns pulse at a gradient of 126 MV/m. The incident and reflected power measured by the peak power meter are shown in black and blue respectively. The calculated reflected power and power coupled into the structure are shown in green and red respectively.

5.6.2 Peak Power Meter Traces

All three peak power meter signals are recorded, but in practice only the forward power channel is used in data analysis. During data analysis the reflected power can be used to check that the system was on resonance for any given forward power meter trace, but this is not generally necessary as the control system is able to quickly find the resonant frequency as it varies and maintain resonance throughout the day. These traces, as well as the power coupled into and reflected by the cavity, are shown in Fig. 5-14.

For each forward power trace, the real system response for that input signal is calculated using the S_{11} values obtained in the cold test. This gives an actual power coupled into the structure for each pulse, which is turned into actual fields and then actual gradient and pulsed heating measurements using HFSS simulations. The measured input rf trace, calculated gradient, and calculated peak surface temperature rise are shown in Fig. 5-15. The actual input power and gradient are then averaged

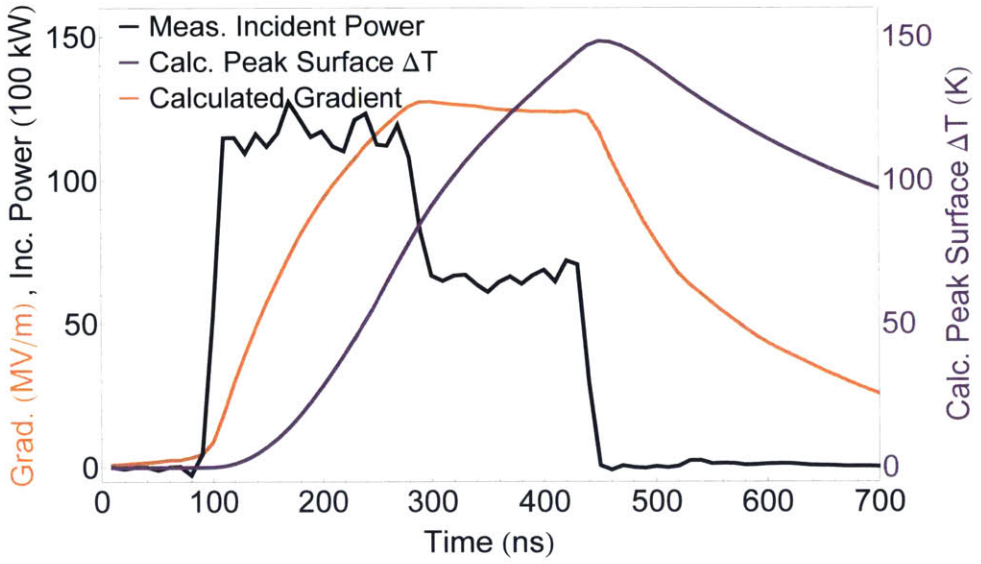

Figure 5-15: Sample traces from the peak power meter for a 150 ns pulse at a gradient of 126 MV/m. The incident power measured by the peak power meter is shown in black. The calculated gradient is shown in orange, and the calculated peak surface temperature rise is shown in purple.

over the flat-top of the pulse, which is calculated for each trace using the known duration of the filling portion of the pulse. The time stamp, pulse length, average filling and flat-top power, average gradient, and maximum value of pulsed heating are all recorded for each trace.

5.6.3 Combining Results

The time stamps on the scope traces and peak power meter traces can be used to correlate the two data sets, providing a plot of accumulated breakdowns and gradient versus time, shown in Fig. 5-16. By looking for sections of these plots where the gradient is approximately constant and the number of breakdowns increases linearly with time, values of breakdown probability versus gradient can be found. Values of breakdown probability versus peak pulsed heating or field values can be found using a similar procedure. The structure was tested at high gradient for more than 350 hours.

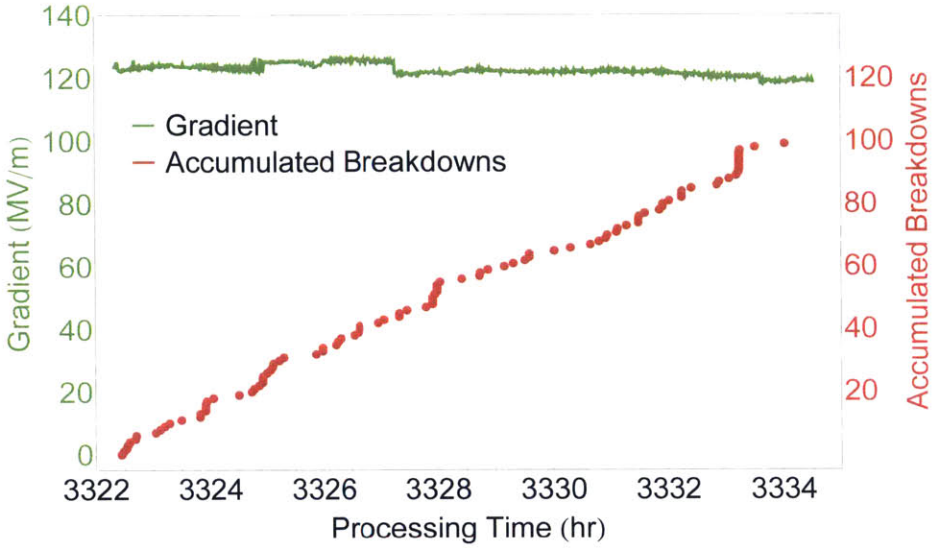

Figure 5-16: Accumulated breakdowns and gradient during the majority of testing.

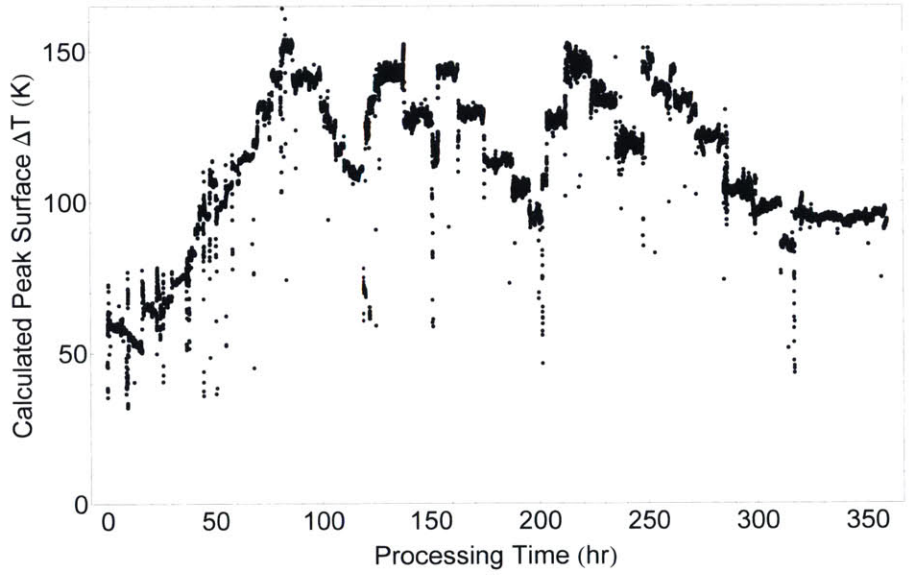

Figure 5-17: Calculated peak surface temperature rise due to pulsed heating in the PBG-E structure.

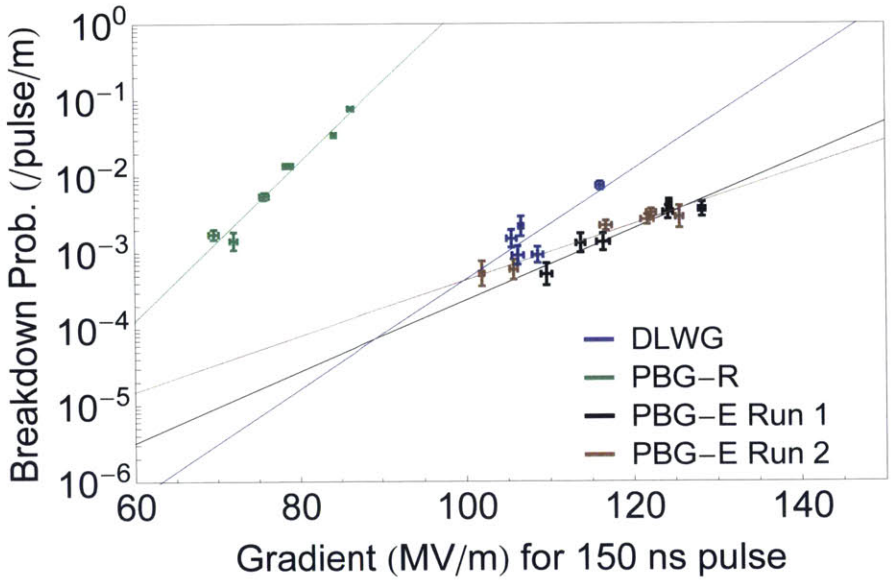

Figure 5-18: Breakdown probability per pulse per meter of structure vs. gradient at 150 ns pulse length for the PBG-R, PBG-E, and a conventional disc-loaded waveguide structure with the same iris geometry (DLWG). The two data sets for the PBG-E represent the beginning and end of testing.

A plot of the peak surface temperature rise for the duration of testing (Fig. 5-17) shows that a majority of the testing was done at greater than the "safe" temperature rise of 50 K [21], with many pulses showing a temperature rise between 100 K and 150 K. Pulses with a peak surface temperature rise of less than approximately 100 K correspond to a breakdown rate less than the artificial lower limit of 1 per hour. This restriction, along with an effort to achieve the largest possible gradient, explains the higher average peak surface temperature rise.

5.7 Experimental Results

For the elliptical-rod PBG structure breakdown probability measurements were made at pulse lengths of 150 ns, 200 ns, 400 ns, and 600 ns. This spans a large portion of the phase space of gradient and peak pulsed heating, as well as providing comparisons to the previous structures. A comparison of breakdown probability versus gradient at a pulse length of 150 ns for all three structures is shown in Fig. 5-18. The two data

sets for the PBG-E structure represent the beginning (Run 1) and end (Run 2) of the testing, indicating no degradation in performance over the course of the testing. The data shows that the breakdown probability increases with the gradient in the structure for a fixed pulse length. All three structures have the same iris geometry and peak surface electric fields that are approximately twice the gradient. The variation in breakdown probability between the PBG-R and PBG-E is likely due to the damage sustained by the PBG-R structure early in testing. The significant improvement in performance between the two PBG structures is likely due in part to the improved design and fabrication and in part to the improved testing methodology, both of which contributed to protecting the PBG-E structure during testing. From Fig. 5-18 it appears that, for undamaged structures, the gradient provides a good prediction of the breakdown probability for the PBG-E and disc-loaded waveguide structures with the same iris geometry at the same pulse length; previous work at SLAC has shown that gradient is not a good predictor of breakdown probability for structures with different iris geometries [51]. More importantly, Fig. 5-18 indicates that the elliptical-rod PBG structure can operate at gradients and breakdown rates comparable to a disc-loaded waveguide structure, while simultaneously providing wakefield damping.

Comparison of the breakdown probability as a function of gradient at different pulse lengths in the PBG-E structure, as shown in Fig. 5-19 indicates that gradient is not sufficient to predict breakdown probability for the PBG-E structure at different pulse lengths, i.e. the breakdowns in the PBG-E structure are not purely due to electric field effects. Previous work with disc-loaded waveguide structures with different iris geometries suggests that the peak surface temperature rise is a good figure of merit for predicting the breakdown probability of a given structure at different pulse lengths, e.g. [50, 51]. This is not the case in the PBG-E structure, as seen in Fig. 5-20. Neither gradient nor peak surface temperature rise alone is sufficient to predict the breakdown probability of the PBG-E structure, indicating that the breakdown probability in the PBG-E structure is likely the result of both electric and magnetic field effects.

The breakdown probability for all three structures can also be plotted as a func-

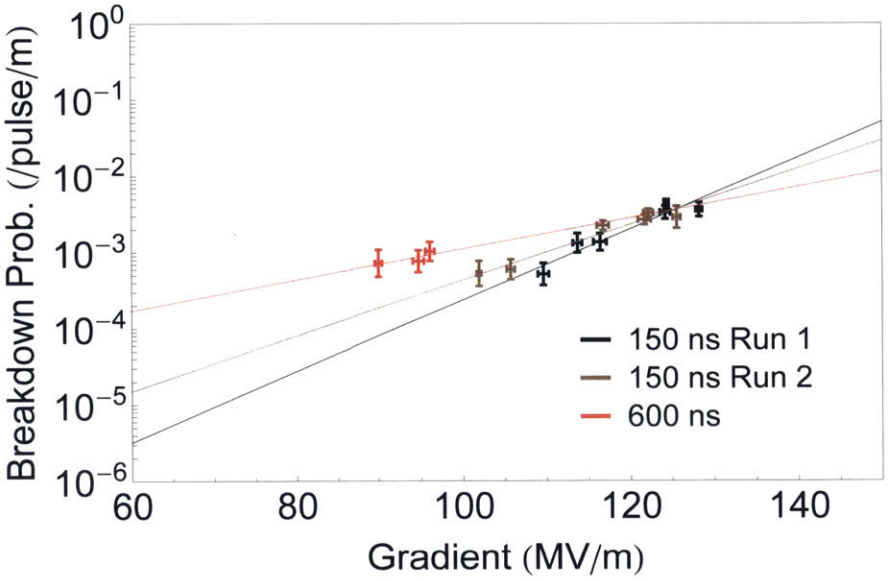

Figure 5-19: Breakdown probability per pulse per meter of structure vs. gradient for PBG-E at pulse lengths of 150 ns and 600 ns.

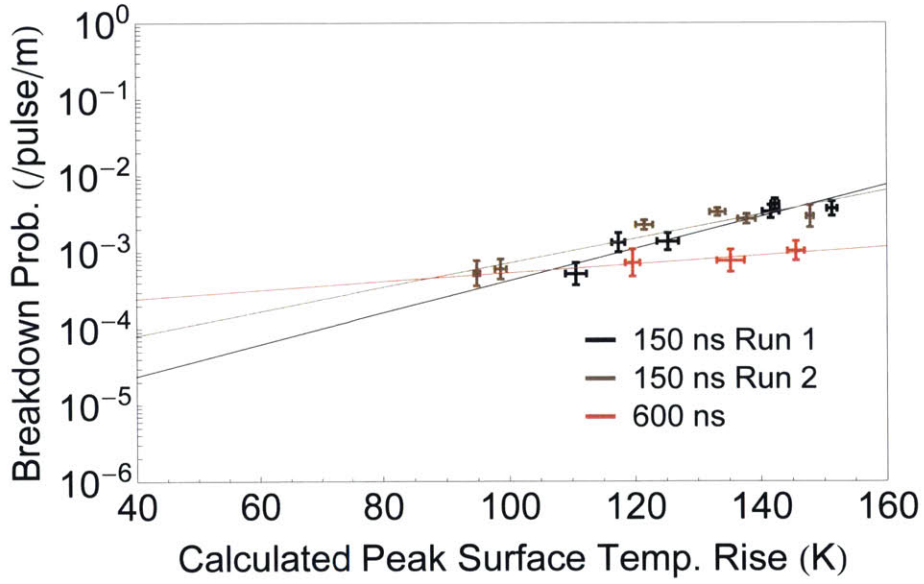

Figure 5-20: Breakdown probability per pulse per meter of structure vs. peak surface temperature rise for PBG-E at pulse lengths of 150 ns and 600 ns.

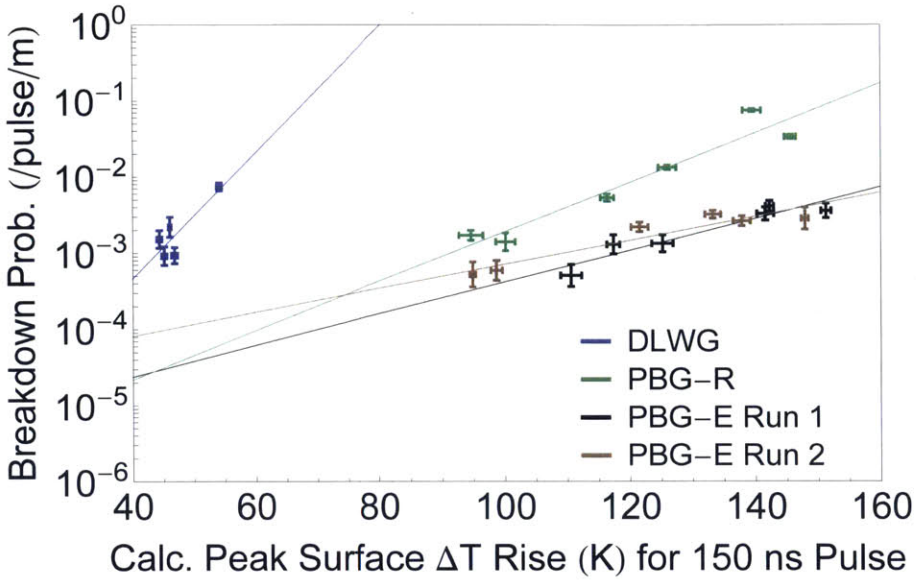

Figure 5-21: Breakdown probability per pulse per meter of structure vs. peak surface temperature rise for PBG-E, PBG-R, and DLWG structures at a pulse length of 150 ns.

tion of calculated peak surface temperature rise, shown in Fig. 5-21, which shows the breakdown probability at a pulse length of 150 ns for all three structures. This shows that the peak surface temperature rise is not sufficient to predict the breakdown probability across multiple structures, indicating that ratio of peak surface magnetic field to accelerating gradient, which varies between the three structures, plays a role in determining the breakdown probability. The elliptical-rod PBG does show marked improvement over the PBG-R structure at similar surface temperature rise, indicating that these temperatures are not sufficient to cause high breakdown probability, even when combined with high gradients. These temperatures occur at much higher gradients in the PBG-E structure than the PBG-R structure; this is a result of the improved design.

5.8 Autopsy

After high-power testing the PBG-E structure was cold tested again. This indicated a decrease in Q_0 for the operating mode from 7800 to 7400, a decrease of approximately 5% from the original value. The structure was then cut in half and examined with a scanning electron microscope (SEM). The structure is cut along the longitudinal direction, with the plane of the cut passing through a rod in the second row but missing all of the rods in the inner row. Cutting along this plane allows SEM imaging of the high-field irises of the structure, on either side of the PBG-E cavity, and the PBG rods themselves; the input coupling iris and the outer rods of the PBG-E cavity can be taken as un-processed surfaces due to the significantly lower fields in these regions.

SEM imaging of the high-field irises showed some damage to both sides of the irises, as seen in Fig. 5-22. This micrograph shows the input iris of the PBG cell, looking perpendicular to the axis of the structure, so that the curvature of the iris cannot be readily seen; the high-field side of the iris is on the right of the image. White splotches of breakdown damage can be seen, as well as grain growth due to pulsed heating. The larger particles visible on the surface of the iris are copper particles deposited during the cutting of the structure for autopsy.

SEM imaging of the inner rods showed significantly more damage to the rod surface than the iris surface, shown in Fig. 5-23. Because the surface magnetic field is concentrated on a small portion of the high-field sides of the inner rods, a variation in surface magnetic field intensity can be seen around the azimuth of the rods, as evidenced by decreased surface damage around the azimuth. The micrographs of the high-field rods show primarily grain formation, with some increase in surface roughness at the grain boundaries, as shown in Fig. 5-24. This is qualitatively different from the damage seen at the highest-field regions of the rods in the PBG-R structure, which shows an increase in surface roughness covering the entirety of the high-field side, obscuring grain boundaries in this region. The elliptical-rod PBG, in contrast, shows increased surface roughness almost exclusively at the grain boundaries, which

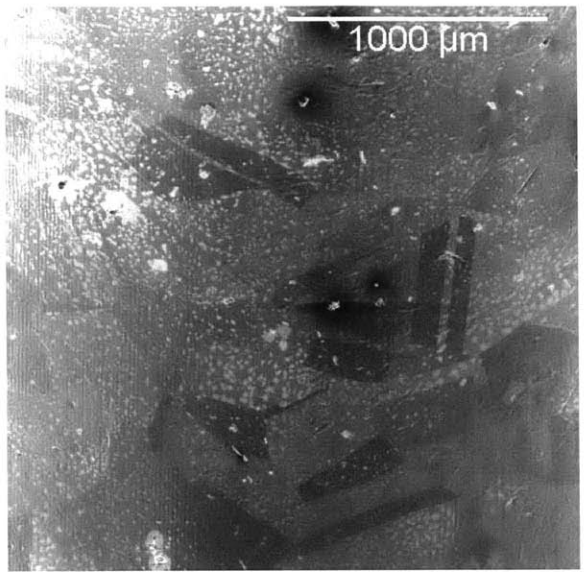

Figure 5-22: SEM micrograph of damage on the iris on the input side of the PBG-E cell. The view shows a close-up view of the iris looking perpendicular to the axis of the structure, so that the curvature of the iris cannot be readily seen. The high-field side of this iris is to the right of the image.

remain visible even in the highest-field region. This qualitative difference is shown in Fig. 5-25. Because both structures saw many pulses with a peak surface temperature rise greater than 100 K, but only the PBG-R saw excursions to over 200 K, the hypothesis that the PBG-R suffered significant damage early in the testing as the result of many shots with extremely high peak surface temperature rise is well supported.

5.9 Discussion

An improved PBG structure using elliptical rods in the inner row was tested at high gradient at SLAC and achieved a maximum gradient of 128 MV/m at a breakdown probability of 3.6×10^{-3} per pulse per meter at a pulse length of 150 ns. This is comparable to the performance of an undamped disc-loaded waveguide structure with the same iris geometry, indicating that PBG-type structures are viable for high-gradient acceleration, consistent with the goal of the revised testing methodology. This achievement of both high gradient and low breakdown probability can be at-

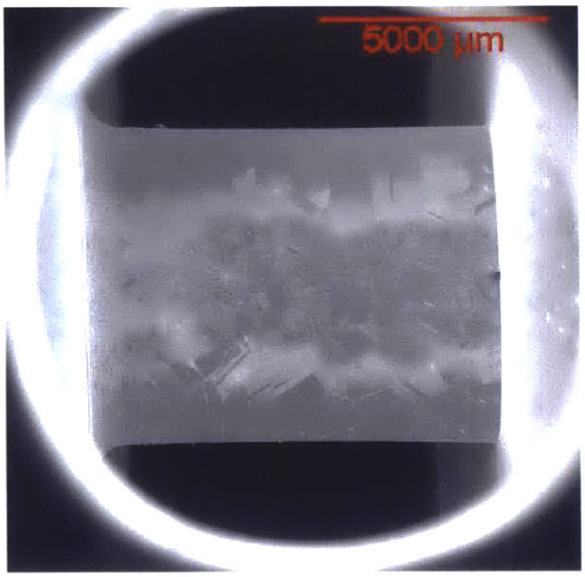

Figure 5-23: SEM micrograph looking directly at high-field side of an inner rod of the PBG-E structure. Grain boundaries are easily visible, and surface roughness does increase at these boundaries.

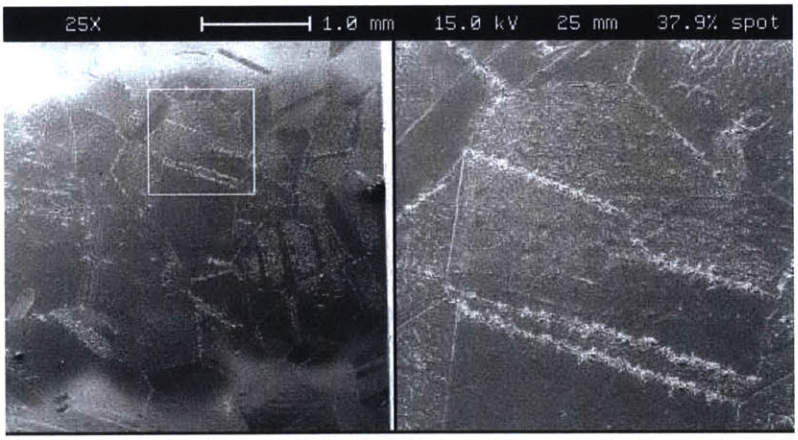

Figure 5-24: Detail micrograph of the high-field side of the inner rod of the PBG-E, showing grain boundaries even at the highest-field region. The PBG-E shows significantly less damage than the PBG-R structure.

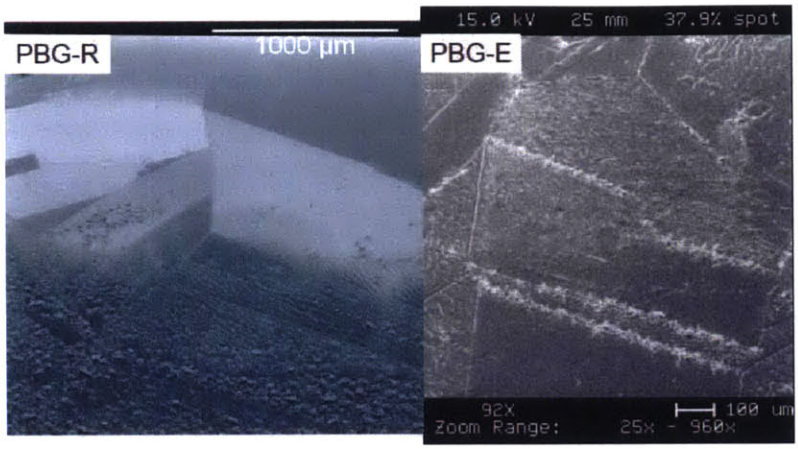

Figure 5-25: Detail micrographs comparing the high-field sides of inner rods of the PBG-R (left) and PBG-E (right), showing the qualitative difference in damage between the two structures. In the PBG-E structure grain boundaries are visible even at the highest-field region, while in the PBG-R structure the strucutre appears uniformly damaged at the highest-field region (bottom of the images).

tributed to improvements in both design and testing methodology. This represents a significant advance in high-gradient structure testing, as the PBG design incorporates intrinsic wakefield damping, which is lacking in the disc-loaded waveguide structures.

This result is particularly significant because the PBG-E structure has wakefield damping. The comparable performance between the PBG-E structure and the disc-loaded waveguide structure indicates that the use of a PBG lattice to damp wakefields does not inherently degrade the performance of the structure. A full comparison of the PBG structure with other accelerator structures would compare the PBG-E to a structure with the same iris geometry that also has wakefield damping, and would need to consider the quality of the wakefield damping in addition to the achieved gradient at a given breakdown probability. It should be noted that the wakefield damping of the PBG-E lattice could be improved via further perturbations of the lattice, as shown in [30]. The PBG-E structure does, however, demonstrate that in principle a structure with wakefield damping via a PBG lattice can operate at high gradients.

The approximately 360 hours of testing for this structure was not long enough to evaluate the lifetime of the structure, but it can be seen that the performance

did not degrade significantly during testing. If the initial operation at high gradient represented an unprocessed state that happened to perform better than the steady-state condition of the structure, then the data should show a regression to a higher breakdown probability when the structure was operated at 150 ns at the end of testing; this was not observed in the PBG-E testing.

The post-testing autopsy did show changes in the high-field surfaces, as well as a decrease in Q_0 of approximately 5%. Both of these changes are likely the result of consistent operation of the structure above the "safe" threshold of 50 K of peak surface temperature rise in an effort to achieve higher gradients and more easily measured breakdown probabilities; when limited to a temperature of 50 K the breakdown rate was much too low to be reliably measured without thousands of hours of testing, something which is beyond the scope of this study. Throughout the testing the breakdown probability remained low, and the damage seen in the SEM images is qualitatively different from the damage observed in the high-gradient testing of the PBG-R structure, indicating that the changes in the high-field surfaces may have caused the decrease in Q but were not sufficient to increase the breakdown probability. At a pulse length of 150 ns the PBG-E structure achieved a gradient of 100 MV/m and a breakdown probability of approximately 5×10^{-4} per pulse per meter.

Future work should seek to categorize the change in the rod surface throughout testing to determine how the change in surface properties due to pulse heating correlates with changes in structure performance. The previous work by Laurent et. al. [21] showed that a peak surface temperature rise of more than 50 K will cause changes in the surface. The PBG-E structure saw temperature rises much higher than this limit, but did not suffer significant changes in breakdown performance; this indicates that physics of rf breakdowns is more complicated than a simple pulsed heating issue. This can be studied with future PBG structures by looking at the rod surfaces in-situ during testing.

Additional testing should also be done at other frequencies, e.g. 17 GHz, to determine how the achievable gradient at a given breakdown probability scales for PBG structures. Demonstration of high-frequency, high-gradient, low breakdown

probability operation of a structure with wakefield damping would be a very important achievement for accelerator development.

Chapter 6

Experimental Testing at 17 GHz: Design and Setup

6.1 Introduction

In order to compare breakdown performance as a function of frequency, two standing wave high-gradient structures have been designed and fabricated for breakdown testing at 17 GHz at MIT. Two round-rod PBG structures (MIT-PBG and MIT-PBG-2), for direct comparison to the PBG-R structure tested at 11 GHz, and a disc-loaded waveguide structure (MIT-DLWG), to serve as a reference for structure performance at 17 GHz, have been tested. Note that both PBG structures tested at MIT are identical. The PBG and DLWG designs are electrically very similar to the structures tested at SLAC, although the mechanical designs of both structures are modified to use a clamped, as opposed to brazed, assembly. A model of the PBG structure tested at MIT is shown in Fig. 6-1; the DLWG structure differs only in the center cell pieces.

These structures will be tested at the MIT Plasma Science and Fusion Center accelerator research lab. The lab features a high-power klystron and an electron beam line for structure testing. The standing-wave structures are tested on a new test stand specifically designed for this purpose. The standing-wave test stand features similar diagnostics to those used at SLAC, with the addition of optical access during testing to the inside of any open structures. An overhead view of the lab with key relevant

Figure 6-1: Expanded three quarter section view of the solid model of the 17 GHz PBG structure, showing two coupling cells and central PBG cell. The coupling rods are not shown for clarity. Power is coupled in from the left.

components labeled is shown in Fig. 6-2.

6.2 Structure Design

Although the electrical design of the structures tested at MIT is extremely similar to the electrical design of the structures tested at SLAC, the mechanical design of the structures was varied significantly. Because the structures tested at MIT are contained in an external vacuum chamber, as opposed to providing both rf and vacuum confinement at SLAC, the mechanical design could be modified to ease fabrication, allow for greater diagnostic access during testing, and allow for easier structure inspection after testing.

6.2.1 Common Modifications

The PBG and DLWG structures tested at MIT are designed using the same basic stacking cup design used for the PBG structures tested at SLAC, however the final assembly of the cups is completed via the use of clamping rods as opposed to brazing. The decision to use a clamped structure was made in part due to the difficulty in tuning seen in testing of a brazed structure and in part due to the difficulty in achieving a high quality braze of all of the joints in a fully brazed design. The use of a

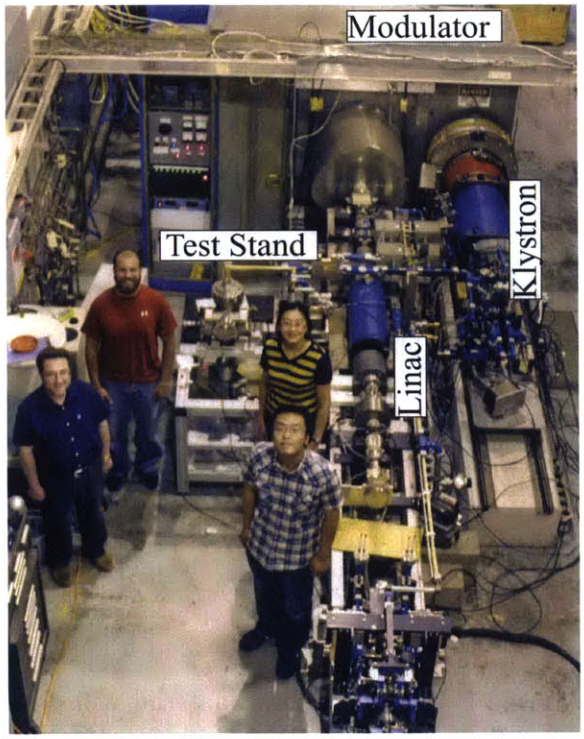

Figure 6-2: The MIT PSFC accelerator research lab. Key components relevant to the standing wave structure test are indicated.

clamped structure is also greatly simplified because of the external vacuum chamber at the MIT standing-wave test stand. While clamped structures which can also hold vacuum have been fabricated, removing this constraint makes clamped designs much more accessible.

In the case of the PBG structure, the high-gradient cell is still brazed in the final clamped design. This allows better alignment of the two high-gradient irises and guarantees good electrical contact for all of the rods. The use of overlapping concentric alignment surfaces between the rest of the cups and the single mating surface at those junctions makes clamping a good alternative for the rest of the structure joints.

Clamping the structure together allows for a number of benefits over the brazed structure. Because the structure can be assembled and disassembled repeatedly, not only can certain parts be reused, but the structure can also be examined carefully at multiple points during the high-power testing. This is in contrast to the brazed structures, where the high-gradient surfaces can only be visually examined via a destructive autopsy after testing is complete.

Using a clamped structure also allows for easier tuning of the structure. Because the structure can be disassembled after the central cell is brazed, the coupling cells can be re-machined as needed to match the desired frequency and axial field profile without concern that the addition of braze material will change the field profile in final assembly. This allows for tuning over a larger range of frequencies, which is useful given the relatively smaller bandwidth of the 17 GHz klystron.

Both structures have the same basic design described in Ch. 4, and the aperture for the high-gradient irises relative to wavelength, a/λ, and the thickness of the irises relative to the wavelength, t/λ, were kept constant. The other fixed parameters discussed in Sec. 5.2, with the exception of Rb which was changed with the change to a clamped design, were scaled to the higher frequency. The final values of these constant parameters are given in Table 6.1, and the parameters are shown graphically in Fig. 6-3.

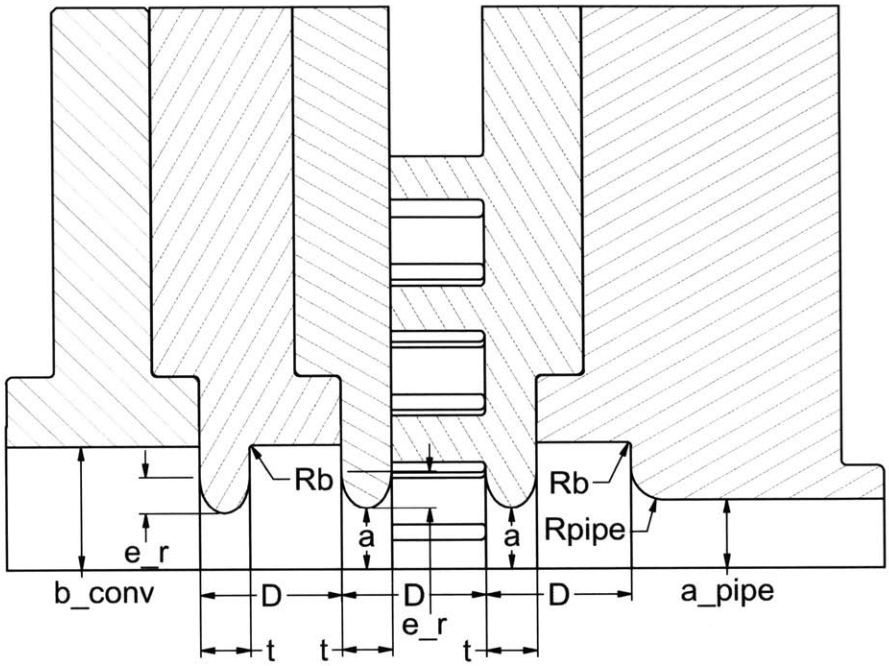

Figure 6-3: Axisymmetric views of the assembly drawing of the 17 GHz PBG structure showing the fixed parameters common to both structures.

Table 6.1: Common fixed parameters for 17 GHz standing-wave structure. Final design values for parameters shown in Fig. 6-3.

Fixed Parameters	
Rpipe	2.0 mm
Rb	0.25 mm
t	3.07mm
e_r	2.27 mm
D	8.75 mm
a	3.77 mm
a_pipe	4.23 mm
b_conv	7.62 mm

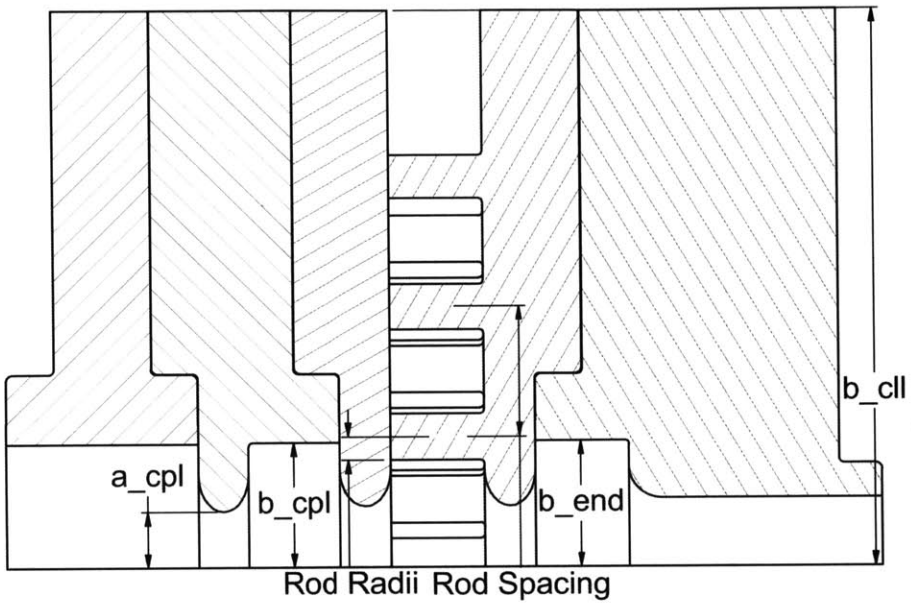

Figure 6-4: Axisymmetric views of the assembly drawing of the 17 GHz PBG structure showing the tuning parameters for the structure.

6.2.2 Design of the Photonic Band-Gap Structure

The photonic band-gap structure for testing at 17 GHz is designed as a scaled version of the PBG-R structure fabricated and tested at SLAC. The structure frequency and field profile were modified in the tuning parameters shown in Fig. 6-4. The radii of the input and output coupling cells, b_cpl and b_end respectively, are varied in HFSS simulations to find a field profile on axis with approximately half of the peak field amplitude in the coupling cells relative to the central PBG cell. The radius to the outer wall of the PBG cell, b_cll, is chosen to allow the clamping rods for the structure to be placed in the holes in a standard 2.75 inch ConFlat flange. The aperture of the coupling iris, a_cpl, is chosen to achieve critical coupling in the HFSS simulation. All three parameters a_cpl, b_cpl, and b_end affect the frequency of the structure, and must be adjusted to keep the resonant frequency of the entire structure within the bandwidth of the 17.142 GHz klystron. The final design values for the tuning parameters are given in Table 6.2.

The assembly drawings in Figures 6-3 and 6-4 also show the major modification

Table 6.2: Tuning parameters for the 17 GHz PBG structure. Final design values for Fig. 6-4.

Tuning Parameters	
a_cpl	3.45 mm
b_cpl	7.69 mm
b_cll	69.34 mm
b_end	7.78 mm
Rod Radii (α)	1.45 mm
Rod Spacing (β)	8.05 mm

to the PBG design for testing at MIT: the open outer wall. Removing the outer wall of the structure provides line-of-sight access to the high-gradient surfaces of the structure, such as the irises and rod faces. Although direct observation of these surfaces in-situ is difficult, the general access to the high-gradient region of the structure allows for optical detection of light produced by breakdowns, with the possibility of localization of the source of this light to identify breakdown location; this will be discussed in more detail in Sec. 6.5.2.

The outer wall in the PBG-E structure tested at SLAC does also increase the diffractive quality factor of that structure. To account for this decrease in diffractive Q when moving to an open-walled structure, the number of layers of rods in the 17 GHz PBG structure was increased. The open wall, like in the traveling-wave structure previously tested at MIT, also allows the HOMs to be radiatively damped. While no HOMs should be excited by the TM_{01} mode launcher, testing the open structure validates that a PBG structure with actual damping can operate at high gradients; in contrast any HOMs excited in the SLAC structures would be reflected back into the lattice by the solid wall.

The key results of the PBG structure design are summarized in Figures 6-5 and 6-6, showing the magnitude of the reflection from the cavity as a function of frequency and the normalized axial field profile of the structure, respectively. Figure 6-5 shows the minimum in reflection for the π mode of the structure of -27 dB, which is achieved at 17.137 GHz; this is comfortably within the operating bandwidth of the MIT klystron. Figure 6-6 shows the desired 1:2:1 pattern in the axial field amplitude.

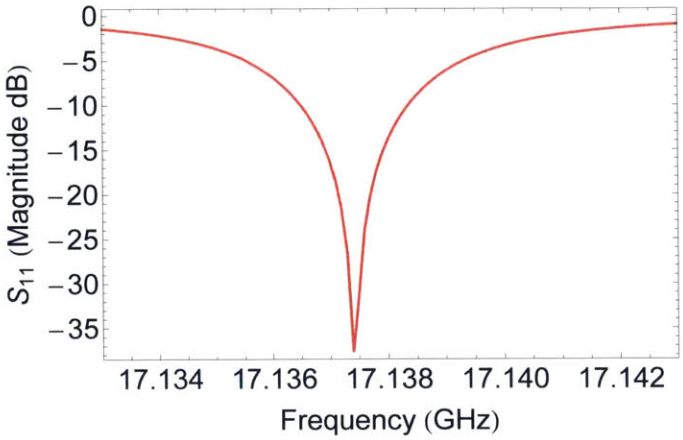

Figure 6-5: Calculated reflection as a function of frequency for the 17 GHz PBG structure.

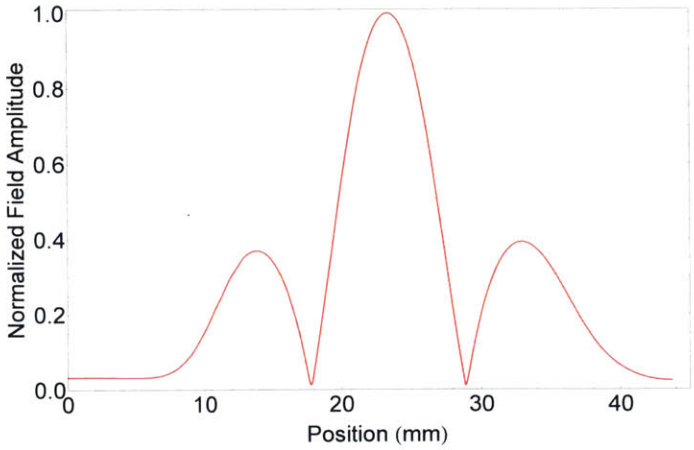

Figure 6-6: Normalized electric field profile on axis in PBG structure; the field amplitude in each coupling cell is approximately half that in the PBG cell.

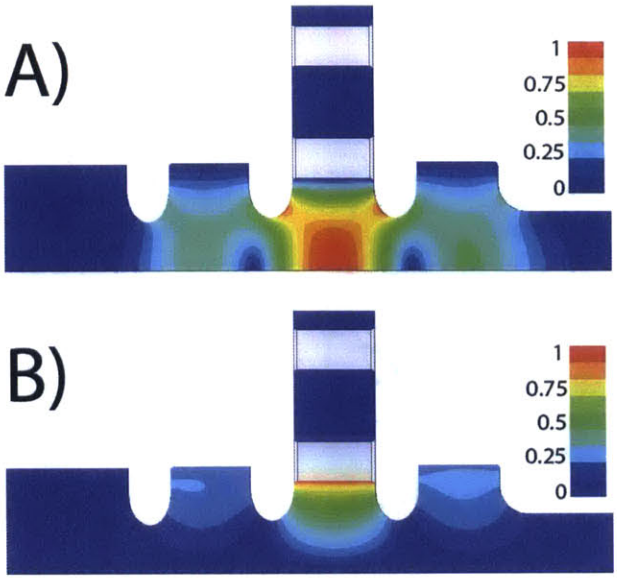

Figure 6-7: Electric (A) and magnetic (B) field amplitudes looking at a radial cut of the structure through an inner rod. At an accelerating gradient of 100 MV/m the peak surface electric field amplitude is 200 MV/m at the iris surfaces. At the same gradient the peak surface magnetic field occurs on the inner surface of the inner rod, and reaches a value of 900 kA/m. The radial extent of the structure has been cropped for compactness.

Field plots for the final design are shown in Fig. 6-7 and Fig. 6-8 in a cutaway view through an inner rod and top-down view, respectively. In the cutaway view the 1:2:1 relationship in electric field value can be seen, as well as the increase in surface electric field on the irises. This view also shows the localization of the magnetic field to the defect-facing side of the inner rods. The top-down view shows the uniformity of the accelerating field in the defect region, and the distribution of the magnetic field across the defect-facing side of the inner rod.

6.3 Design of the Disc-Loaded Waveguide Structure

In order to facilitate rapid testing of the disc-loaded waveguide (DLWG) structure for comparison to the 17 GHz PBG structure, the DLWG structure was designed with

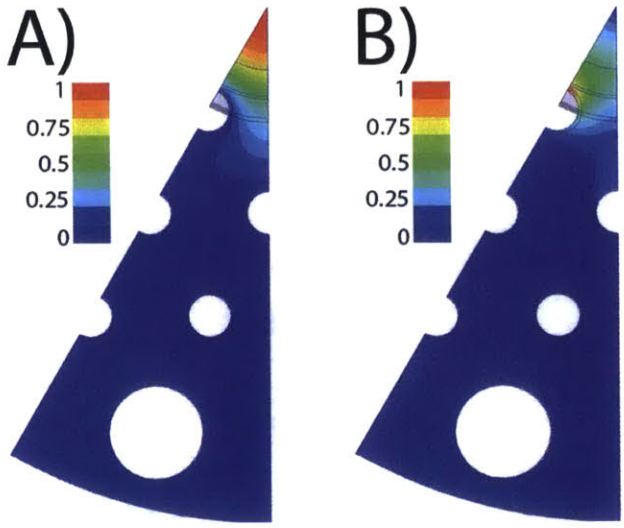

Figure 6-8: Electric (A) and magnetic (B) field amplitudes looking at top-down view of a 30 degree section of the structure. The peak surface electric field of 200 MV/m for a 100 MV/m accelerating gradient is seen on-axis. The peak surface magnetic field of 900 kA/m for an accelerating gradient of 100 MV/m is confined to the center of the inner surface of the innermost rod. The additional large white space at the bottom of the images is the clamping rod that hold the structure together.

identical parameters wherever possible. This allows for reuse of parts for the PBG structure that had already been fabricated. This means that for the DLWG structure the only tuning parameter was the radius of the high-gradient cell, b_cll. While this means that the coupling to and axial field profile of the final design are not optimized, sufficient coupling at a frequency within the bandwidth of the klystron was found at b_cll = 7.58 mm. The additional fixed parameters determined by the PBG design are shown in Fig. 6-9 in black, and the tuning parameter b_cll is shown in blue. The coupling is shown in Fig. 6-10, showing that the π mode has a minimum reflection from the structure occurring at 17.149 GHz with a minimum value of -22 dB.

The axial field profile along the structure is shown in Fig. 6-11. As in the case of the PBG structure design, an approximately 1:2:1 ratio in field amplitude is found. Field plots for the final design are shown in Fig. 6-12 and Fig. 6-13 in a cutaway view through an inner rod and top-down view, respectively. In the cutaway view the 1:2:1 relationship in electric field value can be seen, as well as the increase in surface electric field on the irises. This view also shows the localization of the magnetic field

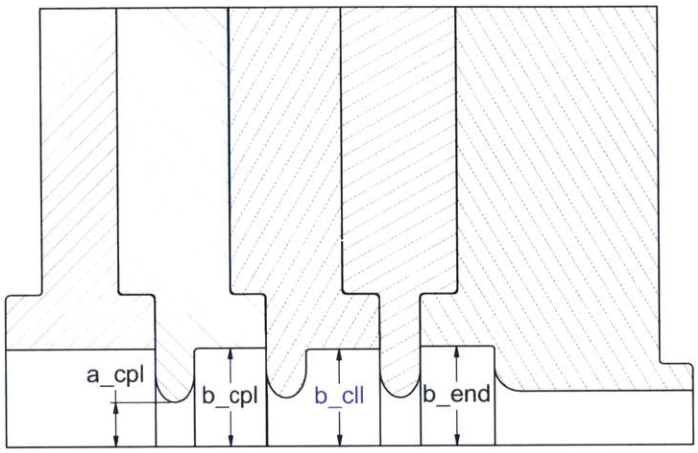

Figure 6-9: Axisymmetric views of the assembly drawing of the 17 GHz DLWG structure showing the additional fixed parameters for the structure in black and the one tuning parameter in blue.

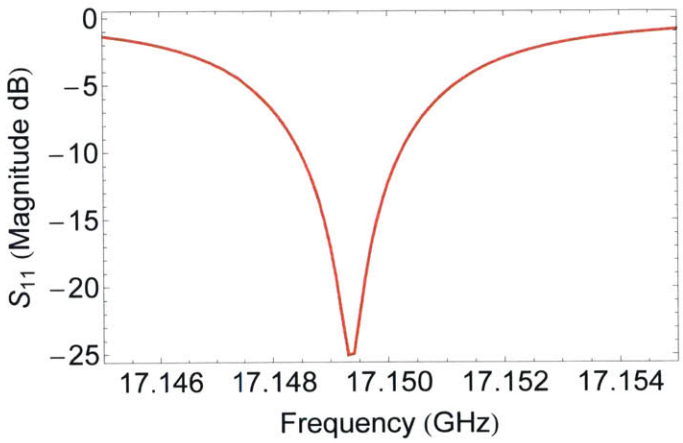

Figure 6-10: Calculated reflection as a function of frequency for the 17 GHz clamped DLWG structure.

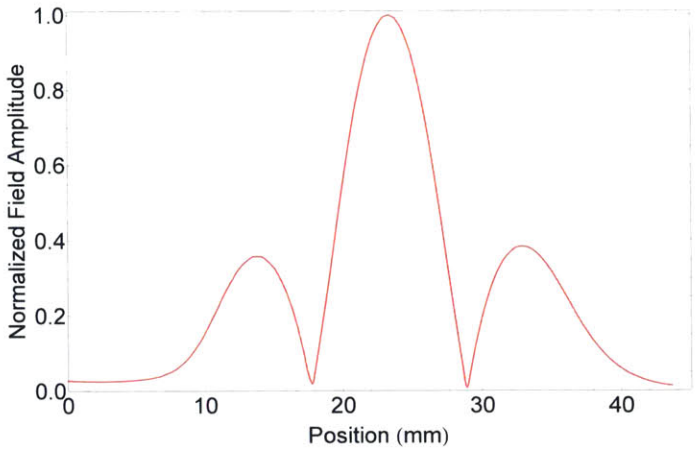

Figure 6-11: Normalized electric field profile on axis in DLWG structure; the field amplitude in each coupling cell is approximately half that in the central cell.

to the outer wall of the central cell. The top-down view shows the uniformity of the accelerating field in the central cell, and the distribution of the magnetic field across the outer wall of the structure.

6.4 Cold Test Setup

Initial setup and tuning of the clamped PBG and DLWG structures was completed using a vector network analyzer (VNA) and an additional TM_{01} mode launcher. The VNA was connected to the rectangular input of the mode launcher and a measurement of the complex reflection (S_{11}) from the single-port structure is made. This measurement can be used to determine if any tuning of the structure is necessary.

In additional to the S_{11} measurement, the axial field profile in each structure is measured. This is done using the same non-resonant technique described in Sec. 5.3.1 where a dielectric bead is suspended on a thin dielectric wire along the axis of the structure. The wire used is Ashaway 10/0 black monofilament micro suture thread and the bead is a small drop of super glue. The bead is moved through the structure with the use of a precision translation stage. The structure is suspended with the axis vertical and tension is maintained on the line using lead weights; the translation stage moves perpendicular to the structure axis over a pulley to reduce bouncing of

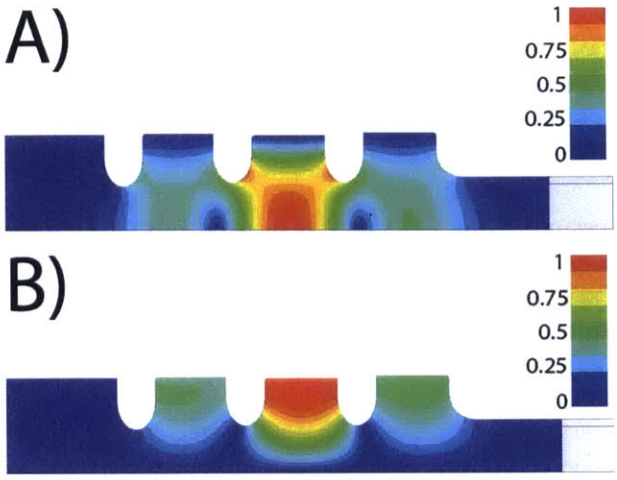

Figure 6-12: Electric (A) and magnetic (B) field amplitudes looking at a radial cut of the structure. At an accelerating gradient of 100 MV/m the peak surface electric field amplitude is 197 MV/m at the iris surfaces. At the same gradient the peak surface magnetic field occurs along the outer wall of the structure, and reaches a value of 421 kA/m.

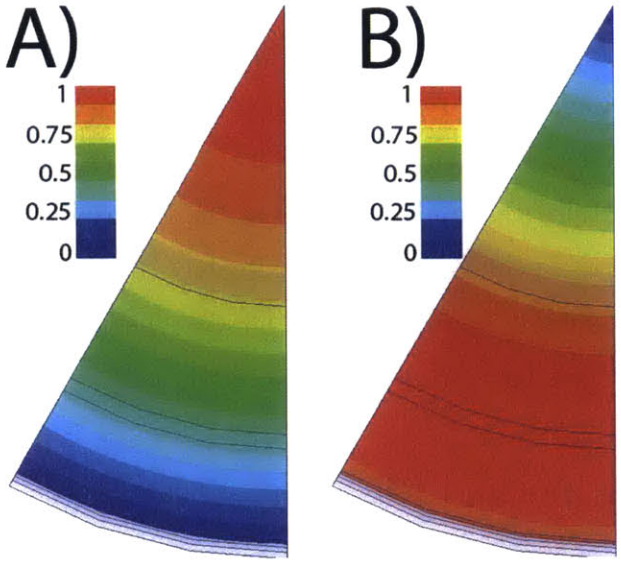

Figure 6-13: Electric (A) and magnetic (B) field amplitudes looking at top-down view of a 30 degree section of the structure. The peak surface electric field of 197 MV/m for a 100 MV/m accelerating gradient is seen on-axis. The peak surface magnetic field of 421 kA/m for an accelerating gradient of 100 MV/m is on the end plate of the structure.

Table 6.3: The operating parameters of the MIT rf system used for high-gradient structure testing.

Maximum rf power to test stand	3.6 MW
Pulse length	10-1000 ns

the bead during testing. This field profile is used both to confirm that the structure is operating in the desired π mode and to determine which coupling cell needs to be modified to tune the frequency of the structure.

6.5 Experimental Setup

Both structures were tested at the MIT Plasma Science and Fusion Center, using a 17 GHz traveling-wave relativistic klystron (TWRK) designed by Haimson Research Corporation. The rf is generated by a continuous wave rf synthesizer and is gated by a pin diode before entering a solid state rf amplifier chain to drive the klystron, producing up to 25 MW of rf power at a gain of 76 dB. The klystron produces square pulses with pulse lengths between 10 ns and 1000 ns.

The standing-wave structure test stand is isolated from the klystron using a 4.4 dB hybrid to prevent power reflected from the structure from returning to the klystron. This test stand is also vacuum isolated from the klystron with an rf window; this window is limited to a peak power of approximately 10 MW, resulting in a maximum power to the test stand of approximately 3.63 MW. The operating parameters of the MIT rf system are summarized in Table 6.3.

6.5.1 Modulator and Klystron

The HRC TWRK operates with a 500 kV electron beam at approximately 90 Amps of beam current produced by a Thomson electron gun. This modulator driving this gun was designed in-house and is capable, in its current configuration, of driving three separate electron guns simultaneously at 500 kV; currently only the Thomson gun is in use. The modulator has a nominal flat top of 1 μs. The rise and fall times of

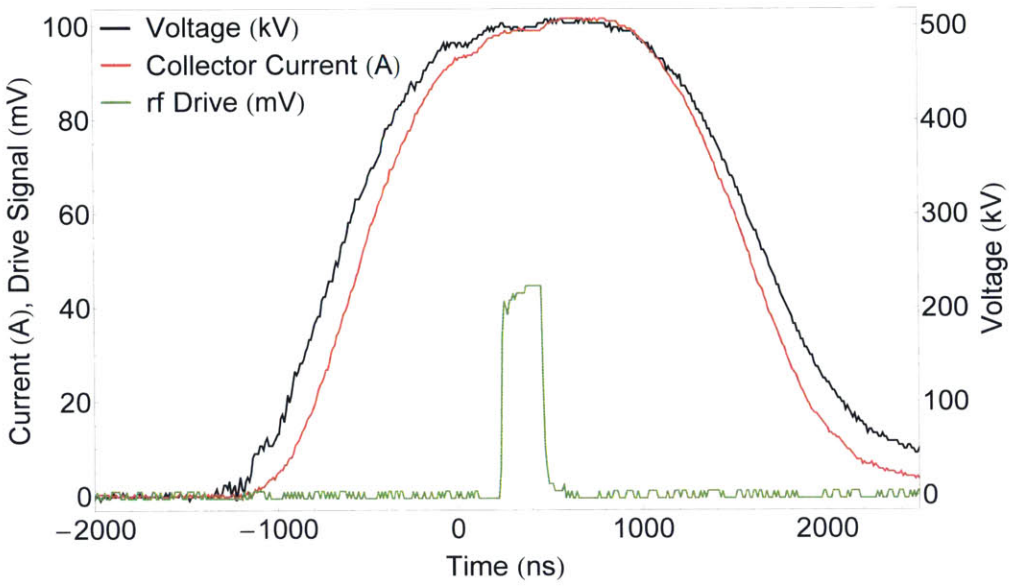

Figure 6-14: Sample traces for the HRC TWRK high-voltage signal, black, current detected at the collector measured via a resistive voltage divider, red, and rf drive signal, green.

the pulse are also approximately 1 μs. A sample voltage trace is shown in black in Fig. 6-14. Also shown on this figure are the beam current measured at the collector via a resistive current monitor, shown in red, and the rf drive signal, shown in green. A small oscillation can be seen on the flat top of the voltage trace, separate from any high-frequency noise generated by the thyratrons. This oscillation is also present on the current detected at the collector, indicating that it is a real component of the voltage. The current transmission shown in Fig. 6-14 has been improved from recent operation through the addition of steering coils. These steering coils have also improved klystron stability and efficiency.

The output of the TWRK is shown in Fig. 6-15. Note that this rf signal is only a 100 ns per division time base, as opposed to the 200 ns per division used for the voltage traces. The timing of the rf drive signal relative to the high-voltage pulse can be controlled, allowing the variation in output power resulting from the oscillation on the high-voltage signal to be used to provide rudimentary shaping of the rf pulse. This does not allow for optimal pulse shaping like that used at SLAC, however it

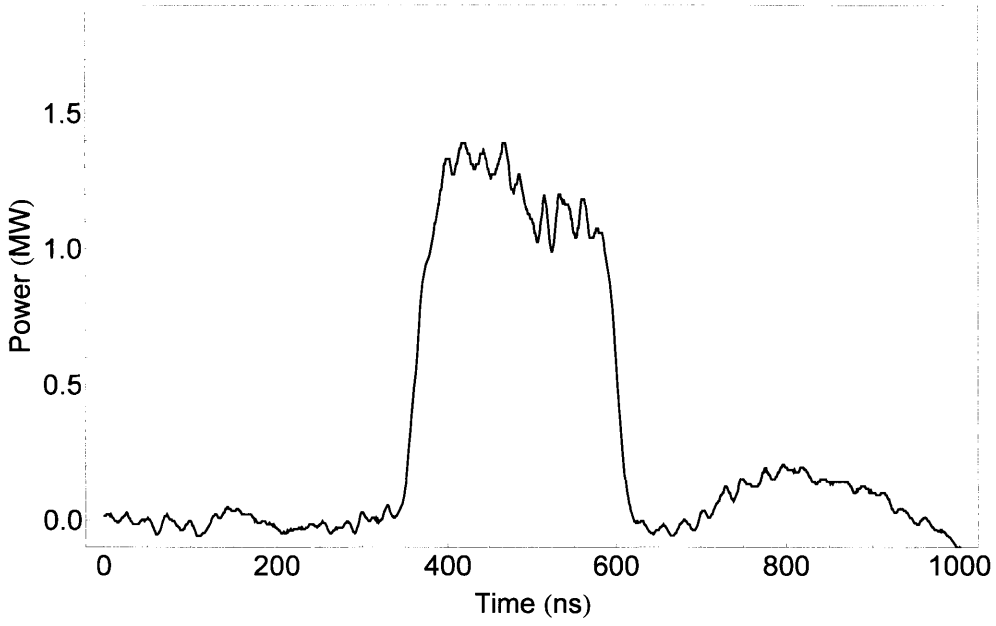

Figure 6-15: Sample output power trace for the HRC TWRK. Pulse shape is due to the fluctuation in the voltage seen in Fig. 6-14, and varies with frequency. This pulse is at approximately 17.150 GHz.

can provide a small decrease in filling time for the structures. The shape of the output pulse does also change with frequency. The result shown in Fig. 6-15 is for the operating frequency of the MIT-PBG structure, approximately 17.150 GHz.

6.5.2 Diagnostics

The standing-wave test stand at MIT is setup to include equivalent diagnostics to those available at SLAC. These diagnostics are a measurement of incident and reflected rf power, and upstream and downstream current monitors. In contrast to the SLAC setup, the diagnostics at MIT do not serve a dual purpose of also controlling autonomous operation of the test stand; this simplifies the diagnostic requirements. A schematic view of the standing wave test stand and associated diagnostics is shown in Fig. 6-16.

The incident and reflected rf power signals are detected using Hewlett Packard HP 8473B low-barrier Schottky diodes coupled into at LeCroy LT264M oscilloscope. Both

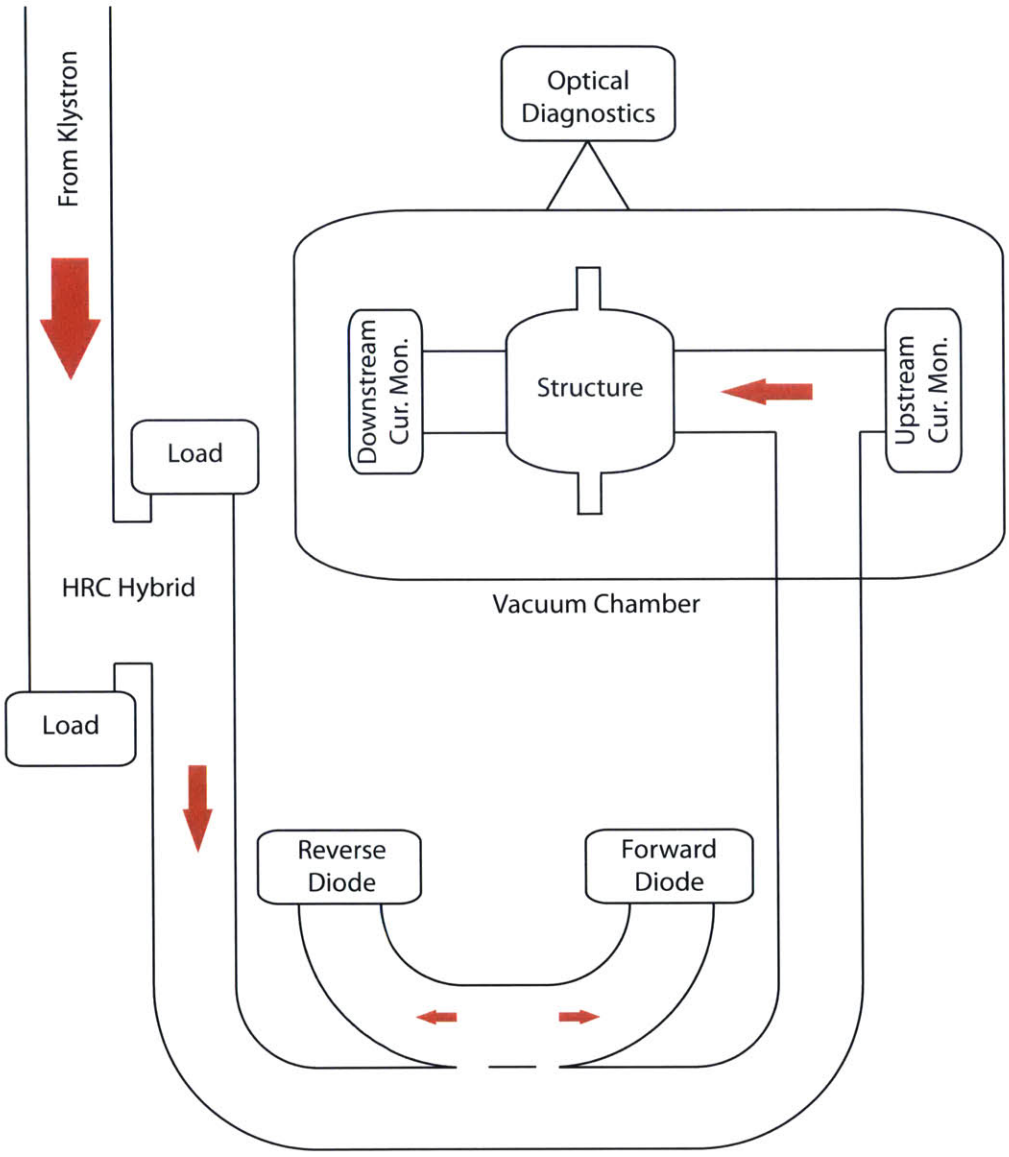

Figure 6-16: A schematic view of the MIT standing-wave test stand and associated diagnostics is shown. Power is coupled from the klystron through a 4.4 dB hybrid made by Haimson Research Corporation (HRC) before coupling into the structure. Incident and reflect rf power signals are measured using diode detectors on a 65 dB waveguide directional coupler. Upstream and downstream current monitors are present within the vacuum chamber.

signals are detected using the forward and reverse arms of a single high-directivity waveguide directional coupler with 65 dB of attenuation in the measurement arms. This directional coupler is located after the klystron protection hybrid, as close as is practical to the structure to give accurate measurements of the incident power. The diode traces are recorded by the associated computer system and saved for later analysis. Control of the rf power level and frequency is achieved via manual control of the rf source.

The upstream and downstream current monitors are both composed of copper plates isolated from the body of the mode launcher and structure, respectively. These current monitors are grounded to the body of the vacuum chamber and terminated into 50 Ohm loads on the same LeCroy LT264M oscilloscope used for rf detection. This allows for very good relative timing of different breakdown events compared to the rf pulse, although due to differences in signal cable lengths the absolute timing of the current signals relative to the rf cannot be determined. The current monitor signals are used both to monitor the dark current during normal operation and to detect breakdown events. Because of the resolution of the oscilloscope, either the full current signal during a breakdown, or the dark current signal during normal operation, can be resolved, but not both simultaneously. The system is typically operated such that the dark current can be resolved. This allows for breakdowns to be detected as a binary signal; if the current monitor signal goes off-scale, then a breakdown is determined to have occurred. If the full breakdown signal is detected, then the dark current signal is indistinguishable from zero, making this a less useful operating condition.

Because of the open nature of the clamped 17 GHz PBG structure, optical diagnostics are also available at the MIT test stand. During the initial PBG structure testing a video camera was used to visually observe the locations of breakdown during testing. Bright flashes can be seen during breakdown events, and the location of the brightest part of the flash is assumed to correspond to the initiation site of the breakdown. Unfortunately no practical system was in place to record and analyze this information, meaning that no quantitative analysis of the visual indications of

breakdown was possible. This information could, however, be used to provide qualitative agreement with post-testing inspection of the structure, which will be discussed in Ch. 7. The direct visual access could also be used to record light emission during breakdowns using a still camera or photodiode, however an appropriate still camera was not available during PBG testing and photodiodes were not able to detect any signal.

6.6 Data Analysis

Analysis of the data recorded during testing at MIT follows the same basic procedure outlined in Ch. 5: rf power traces are analyzed to determine the power coupled into the structure, this is calibrated using HFSS simulations to determine field-related quantities such as gradient and pulsed heating, and these results were combined with breakdown information to determine breakdown probability as a function of the desired quantity, e.g. gradient or peak surface temperature rise. Every effort was made to keep the analysis code procedure consistent between the two experiments, ensuring that the results are calculated in a consistent fashion.

The differences in experimental setup do require slight modifications to the Mathematica analysis code. At MIT the data is stored as a diode voltage, whereas at SLAC the peak power meter stores real power values given the attenuation present in the system. These diode voltages are converted to power levels prior to analysis. Because the rf traces at MIT are flat as opposed to shaped for more efficient filling of the structure, the effective pulse length must also be calculated slightly differently at MIT. At SLAC the pulse length, defined to be the length of time during which the structure is in a steady-state condition, is well defined by the drive pulse length. At MIT, however, fluctuations in voltage during the rf pulse combined with a flat rf drive pulse result in variations in power level during the pulse. To account for this the pulse length is calculated as the length of time during which the power level in the structure is at least 80% of the maximum power level; this agrees well with the predictions for a square pulse given the quality factor of the structure.

One important difference between the MIT and SLAC setups is that at MIT both rf power signals and one current monitor trace are recorded every pulse, whereas at SLAC rf power signals are recorded every two seconds while operating at 60 Hz, and current monitor traces are only recorded for pulses on which a breakdown is detected and the pulse immediately preceding a breakdown. The data recording system at MIT is not capable of discriminating between normal operation and breakdown signals in real time, thus requiring the recording of every pulse. This also avoids any potential systematic errors that might arise if rf power signals were only recorded for pulses during which breakdowns occurred.

While recording three traces for every pulse is possible with the current data collection system, recording a fourth trace for every pulse introduces an unacceptable number of data storage errors; this is the reason for only recording one current monitor signal. Sample traces for the data recording will be shown in Ch. 7.

6.7 Sample Traces

All data used for analysis at MIT is recorded from a single oscilloscope. Data is recorded from the LeCroy LT264M oscilloscope using a LabView routine that records the forward rf signal, reflected rf signal, and downstream current monitor signal for every pulse. A sample set of these traces, as well as the power coupled into the structure corresponding to this forward power pulse, is shown in Fig. 6-17. The forward power and current monitor traces from each pulse must be analyzed to calculate the power coupled into the structure and whether or not a breakdown occurred. A sample of traces for a pulse during which a breakdown did occur is shown in Fig. 6-18. The breakdown can be seen as an increase in both the current monitor signal and the reflected power signal to the limit of the oscilloscope range. Note also that the current monitor signal in this figure is on a much larger scale, amps versus milliamps. The upstream current monitor signal, which typically shows a zero reading, is not recorded due to throughput limitations of the data collection system.

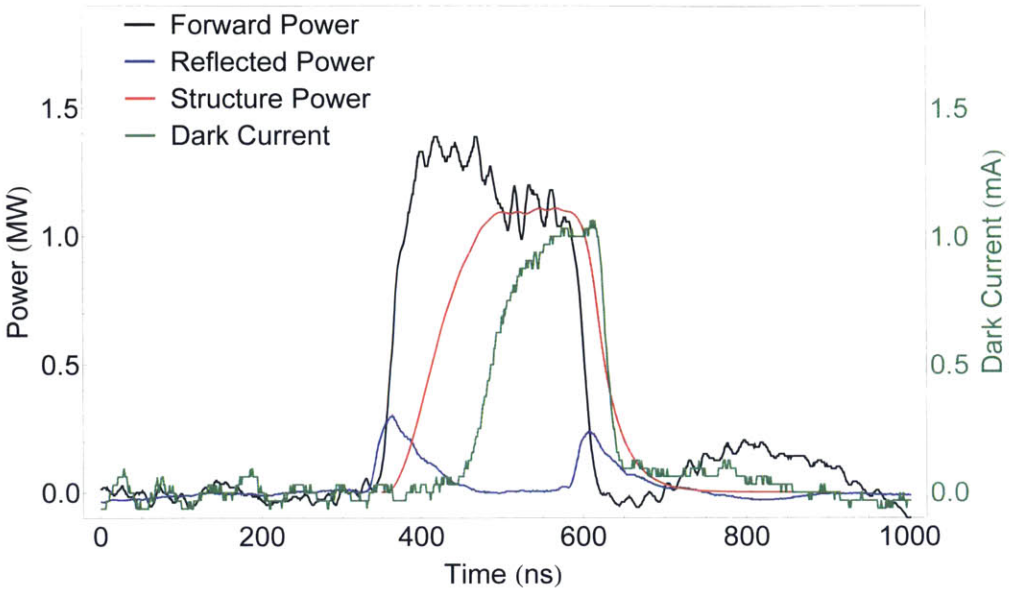

Figure 6-17: Sample forward power, black, reflected power, blue, downstream current monitor, green, and calculated structure power, red, traces are shown. This trace was recorded during the MIT-PBG testing.

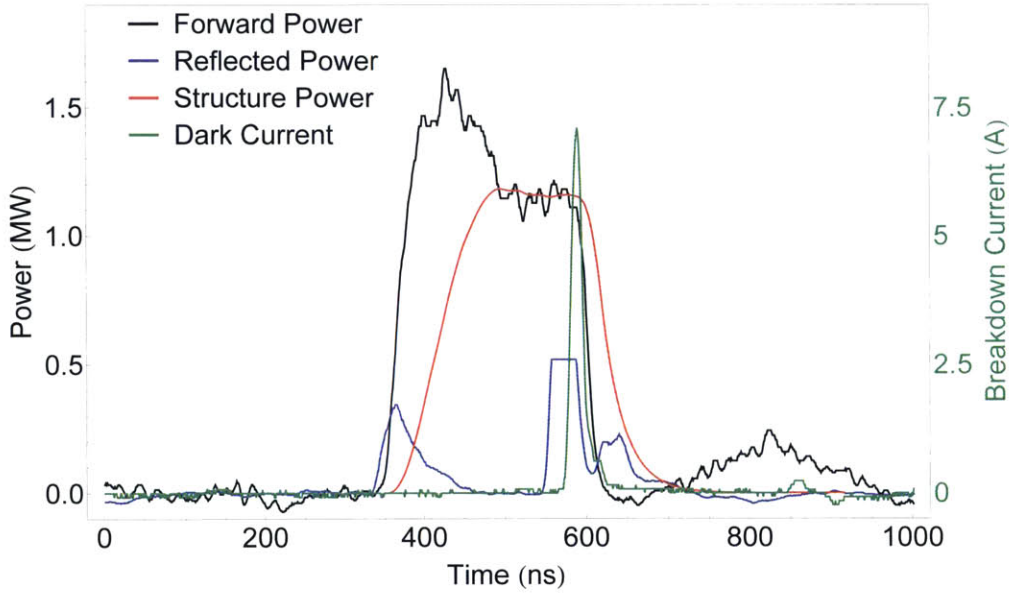

Figure 6-18: Sample forward power, black, reflected power, blue, downstream current monitor, green, and calculated structure power, red, traces for a pulse during which a breakdown occurred are shown. This trace was recorded during the MIT-PBG testing.

Chapter 7

Experimental Testing at 17 GHz: Results

Both the photonic band-gap and disc-loaded waveguide structures designed and built for testing at MIT were subjected to both low-power (cold) and high-power (hot) testing. The low-power testing served to confirm that the structures were operated in the desired mode at an acceptable frequency, while the hot test of each structure was used to determine the breakdown performance of each structure. Cold test measurements were taken before and after hot testing to look for any degradation in the structure performance as a result of the hot tests.

7.1 Cold Test Results

Both structures were measured using the same mode launcher. The complex reflection coefficient (S_{11}) was measured first to determine the resonant frequency of the structure. Using the S_{11} measurement the resonant frequency, coupling, and mode Q values can be determined for each structure mode [59]. The unloaded Q, Q_0, and external Q, Q_{ext}, can be measured directly from the Smith chart. These are then used to calculate the loaded Q, Q_L, via $1/Q_L = 1/Q_0 + 1/Q_{ext}$. After the resonant frequency was determined the structures were moved to the bead pull setup, shown in Fig. 7-1 with the clamped DLWG structure under test. The results of both these

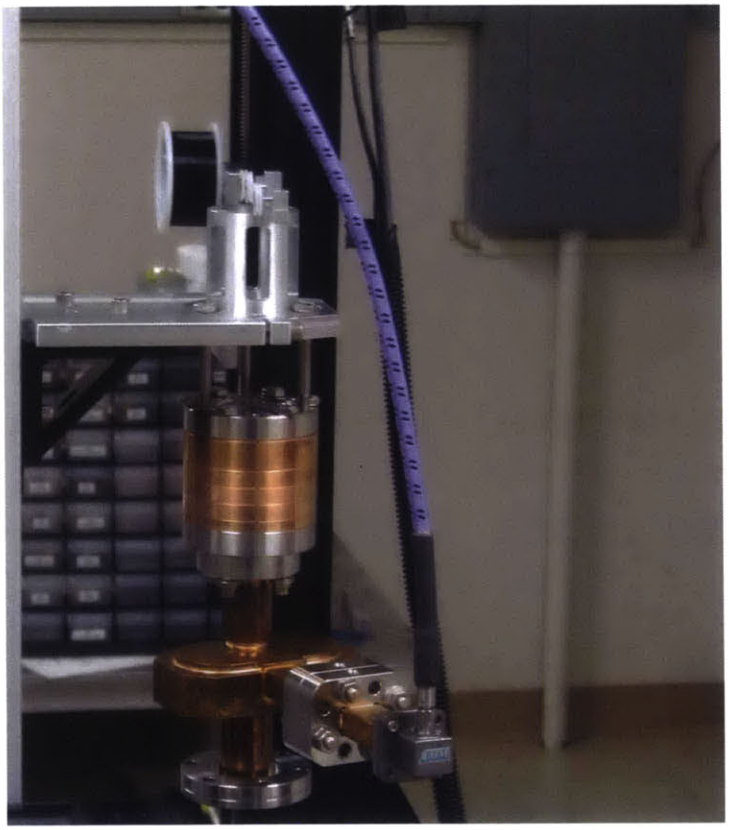

Figure 7-1: Photograph showing the disc-loaded waveguide structure undergoing a bead pull measurement to determine the axial field profile.

measurements are discussed below for their respective structures.

7.1.1 PBG Structure

Despite reducing the total number of braze joints in the structure, matching the design frequency for the PBG structure proved challenging. After switching the braze material from copper-gold to Silcoro, a copper-gold-silver mixture, a resonant frequency within the acceptable range was found. The measured reflection of the structure for this final structure is shown in Fig. 7-2. The data in Fig. 7-2 is restricted to the π mode of the structure, as confirmed by the axial field profile shown in Fig. 7-3, which compares the measured field profile to the field profile from simulation. The non-zero field in the input waveguide of the structure that can be seen in Fig. 7-3 is the result of non-critical coupling into the structure. The quality factor and frequency of the

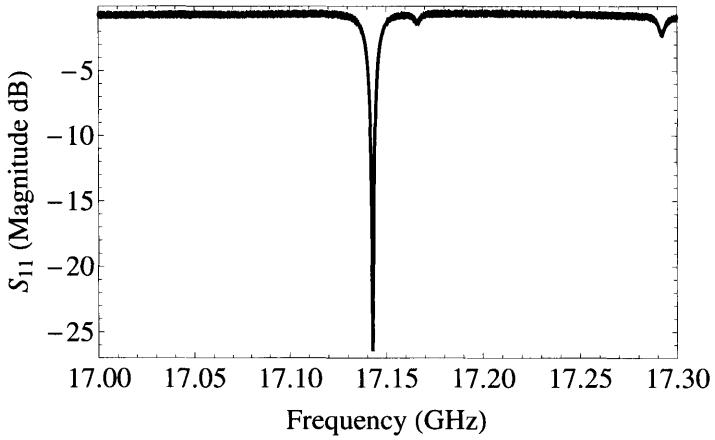

Figure 7-2: S_{11} of PBG structure showing resonance for the π mode.

Table 7.1: Q values for the π mode of the PBG structure. Note that this frequency is measured in air. The resonant frequency in vacuum is 5 MHz higher.

Mode	Frequency	Q		
	(GHz)	Q_0	Q_{ext}	Q_L
π	17.143	4609	6211	2646

operational mode of the clamped PBG structure calculated from the S_{11} are given in Table 7.1.

The cold test of the clamped PBG structure also provided a test of the optical diagnostic access present in the open-walled structure. During the bead pull, the small dielectric perturber could be seen inside the central cell of the PBG structure, as shown in Fig. 7-4.

7.1.2 DLWG Structure

The measured resonant frequency and quality factors for the π mode in the 17 GHz clamped DLWG structure are shown in Table 7.2; the measured reflection data from which these values are obtained are shown in Fig. 7-5. The observed frequency of the DLWG structure is approximately 20 MHz below the design value. The expected shift in frequency resulting from measuring the reflection in air instead of vacuum is 5 MHz. The remaining 15 MHz shift in frequency is likely due to small fabrication

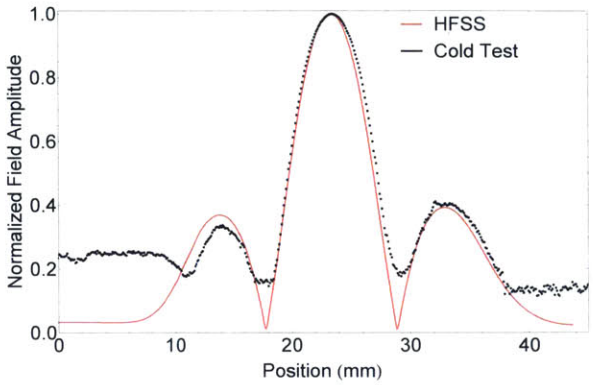

Figure 7-3: Comparison of the simulated and measured axial field profiles for the π mode of the PBG structure.

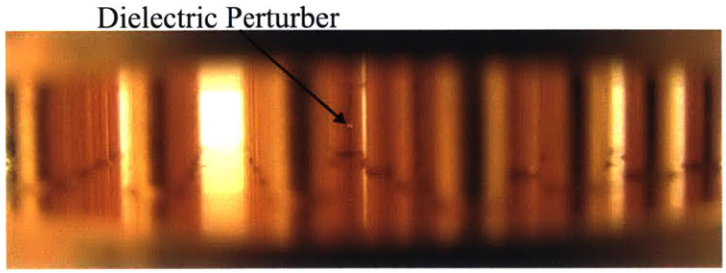

Figure 7-4: Photograph showing the dielectric perturber in the central PBG cell. This illustrates the optical access to the high-field side of the rods even during operation.

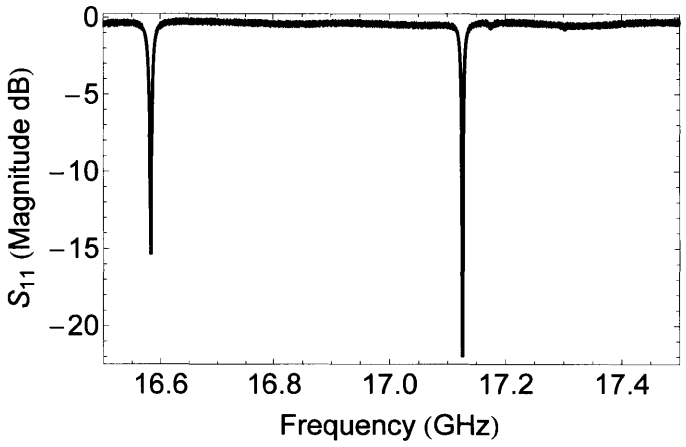

Figure 7-5: S_{11} of DLWG structure showing resonances for the $\pi/2$ and π modes at increasing frequency.

Table 7.2: Q values for the π mode of the DLWG structure. Note that this frequency is measured in air. The operational value is 5 MHz higher in frequency.

Mode	Frequency	Q		
	(GHz)	Q_0	Q_{ext}	Q_L
π	17.126	5166	5270	2609

errors across all of the pieces of the clamped assembly. The DLWG structure was tuned by shortening the central cell so that the coupling cells could be used for testing of additional PBG cavities.

A comparison of the measured axial field profile to the simulation results for the DLWG structure is shown in Fig. 7-6. This confirms that the structure is operating in the π mode at the desired resonant frequency, with approximately a 1:2:1 ratio of field amplitude across the three cells. Given that the coupling to the structure is very close to critical, the non-zero field amplitude seen outside of the coupling cells is likely a result of noise in the measurement. This can result from larger step sizes in the bead position, contamination of super glue on the thread suspending the bead, or disturbances to the setup during measurement.

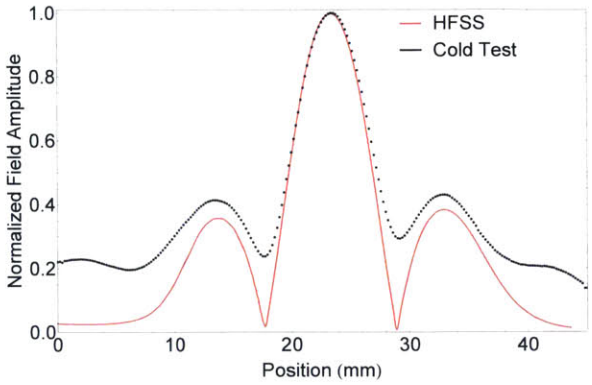

Figure 7-6: Comparison of the simulated and measured axial field profiles for the π mode of the DLWG structure.

Table 7.3: Q values for the π mode of the MIT-PBG-2 structure. Note that this frequency is measured in air. The resonant frequency in vacuum is 5 MHz higher.

Mode	Frequency	Q		
	(GHz)	Q_0	Q_{ext}	Q_L
π	17.136	4745	6095	2668

7.1.3 Second PBG Structure

After testing of the MIT-DLWG structure a second PBG structure (MIT-PBG-2) was measured. This structure reused all of the components used in the MIT-DLWG structure except the cylindrical central cell. The measured reflection of the structure for the MIT-PBG-2 structure is shown in Fig. 7-7. The frequency for this structure matches the design value of 17.137 GHz much more closely than the orignial MIT-PBG structure. The data in Fig. 7-7 is restricted to the π mode of the structure, as confirmed by the axial field profile shown in Fig. 7-8, which compares the measured field profile to the field profile from simulation. There is significant noise in the field profile shown in Fig. 7-8. This is the result of fraying of the thread used to suspend the dielectric bead used for the measurement. The quality factor and frequency of the operational mode of the clamped PBG structure calculated from the S_{11} are given in Table 7.3.

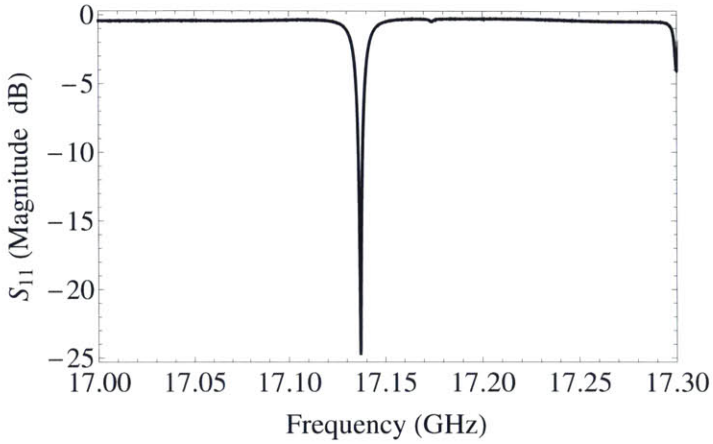

Figure 7-7: S_{11} of the MIT-PBG-2 structure showing resonance for the π mode.

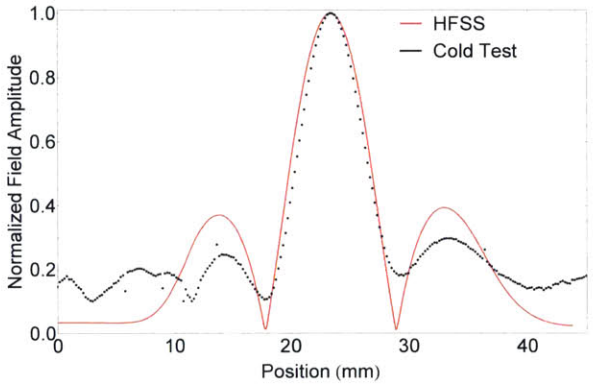

Figure 7-8: Comparison of the simulated and measured axial field profiles for the π mode of the MIT-PBG-2 structure.

7.2 First PBG Experimental Results

7.2.1 Testing Methodology

The objective of the breakdown experiments at MIT is to compare the performance of PBG structures at high gradients and different frequencies than those used in the SLAC testing. While the clamped PBG structure tested at MIT was designed based on the PBG-R structure tested at SLAC, the testing methodology for the structure was based on the testing of the PBG-E structure. Predetermined limits on input power and pulse length were determined to ensure that the temperature rise in the structure remained below 120 K. The lower limit on breakdown rate is still approximately one breakdown per hour, however this represents one breakdown every 3600 pulses at MIT as opposed to one breakdown every 216,000 pulses at SLAC. In terms of breakdown probability per pulse per meter of structure, the testing at MIT is limited to between 1, at 30 breakdowns per hour, and 3×10^{-2} at 1 breakdown per hour.

The upper limit on number of breakdowns in an hour was similarly maintained at around 10 breakdowns per hour at both MIT and SLAC. Because the repetition rate is limited at the present time to 2 Hz at MIT as opposed to 60 Hz at SLAC, a higher maximum breakdown probability per pulse must be tolerated at MIT to allow for accumulation of a sufficient number of breakdown events. The testing was further complicated by the propensity of the PBG structure to suffer chains of multiple successive breakdown events. This meant that overall probability of a breakdown occurring was an order of magnitude or more higher than the probability of a breakdown initiation (i.e. a breakdown immediately following a non-breakdown pulse) for the MIT-PBG structure. Because the relevant quantity for structure performance is the probability of breakdown initiation, but the relevant quantity for structure damage is total probability of breakdown, very small changes in probability of breakdown initiation took the structure beyond the tolerable limit for total breakdown probability.

7.2.2 Optical Diagnostics

Quantitative optical diagnostics were unavailable during the MIT-PBG testing. While video monitoring of the structure during testing was available, the photodiodes tested with the structure did not produce measurable signals during testing. The video signal was monitored in the control room, and qualitative analysis of breakdown events as the occurred was possible. No still images from this video feed, however, are available. The real-time impression of the video feed was that there were three distinct possibilities for the visual signal from breakdown events: a visible signal fading to either side of the location of maximal intensity, a visible signal fading to one side and sharply terminated on the other side of the location of maximal intensity, or no visible signal was present.

In the cases where a visible flash was present during breakdown, the difference between whether the breakdown image fades on both sides or is truncated is assumed to be dependent on the location of the breakdown. If the breakdown occurs within the center cell, the image should fade on both sides before the visible signal is blocked by the irises. If the breakdown occurs on the high-field side of either iris of the center cell, the maximum intensity of the breakdown image should be comparable to breakdowns occurring within the center cell, but the image will be truncated by the iris on one side. If the breakdown occurs outside of the center cell and its irises, which is not expected, a lower-intensity signal that is truncated on one side and fades on the other is expected. These two general cases together provide rough localization of the breakdown events, and open up the possibility of quantitative image analysis for breakdown images.

In the case where no visible flash was present a more quantitative system than what is currently in place is required. The absence of a visible indicator of breakdown could be the result of a breakdown producing light, but occurring very far the center cell, resulting in insufficient light reaching the camera to be seen. It is also possible that the breakdown does not produce any light. A quantitative analysis of the images could look for correlations between breakdown images and measured breakdown parameters,

e.g. peak or integrated current monitor signal, integrated reflected power signal, or duration of rf prior to breakdown initiation.

7.2.3 Testing Summary

Testing of the MIT-PBG structure was conducted in several phases. Initial conditioning of the structure was done at flat-top pulse lengths below 100 ns, before moving on to a flat-top length of 150 ns for Phase 1 of the testing. Phase 1 lasted for approximately three weeks, during which time the structure was seen to process, but operation was limited to less than 70 MV/m at a pulse length of 150 ns because the breakdown probability increased very rapidly above this gradient. This thresholding behavior led to the removal of the structure and repair of a poor connection between the structure and mode launcher. The structure was reinstalled and Phase 2 of the testing began. During Phase 2 of the testing thresholding behavior was again observed, with the limiting gradient decreasing to 65 MV/m at a pulse length of 150 ns. The pressure in the test chamber was also anomalously high during Phase 2 of the testing. This, combined with evidence of another poor connection between the structure and mode launcher, led to the structure being removed a second time, remeasured, and reinstalled with a spacer between the structure and mode launcher to make the joint more reliable. After this final installation Phase 3 of the testing began, during which time an initial threshold gradient of less than 60 MV/m at a pulse length of 150 ns was observed. The testing methodology was varied during Phase 3; both shorter pulse lengths and allowing hundreds of consecutive breakdowns were attempted to push past the decreasing gradient threshold. These efforts resulted in a final limiting gradient prior to the onset of thresholding behavior of approximately 55 MV/m at a pulse length of 100 ns. The combined gradient and pulse length for all three phases of testing are shown in Fig. 7-9 as a function of pulse number. In total Phase 1 lasted approximately 192,000 pulses, Phase 2 lasted only approximately 53,000 pulses, and Phase 3 lasted the remaining approximately 263,000 out of the total of 482,000 pulses seen by the MIT-PBG structure.

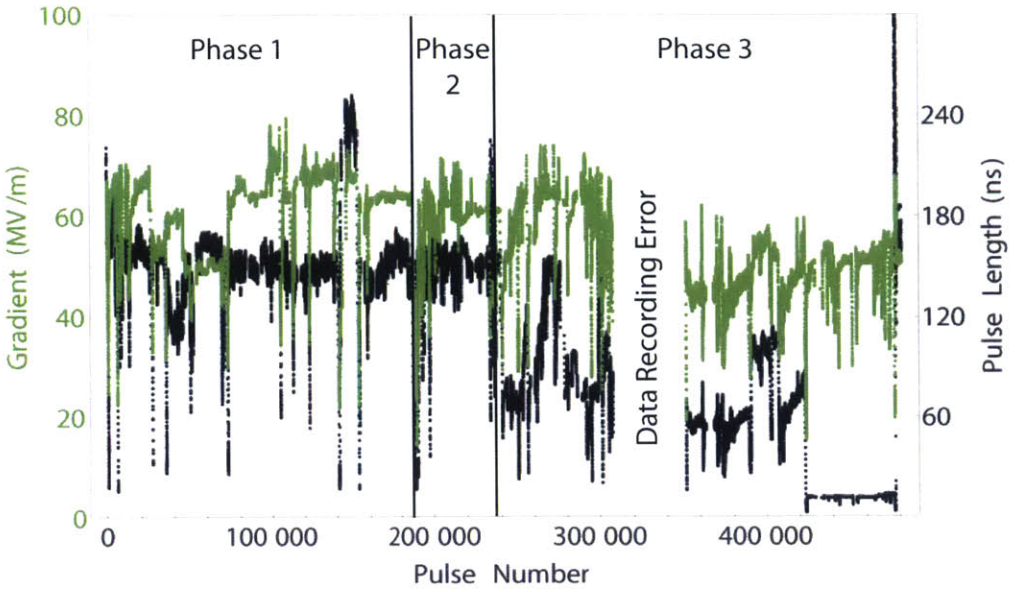

Figure 7-9: Summarized results showing the gradient (green) and pulse length (black) for the duration of PBG structure testing at MIT. A running average over 19 data points has been used for clarity.

7.2.4 Phase 1

The initial processing of the structure during Phase 1 reached a gradient of 64 MV/m at a breakdown probability of 4 breakdowns per pulse per meter of structure for a pulse length of 150 ns, corresponding to a breakdown rate of over 100 breakdowns per hour at 1 Hz. With continued processing this breakdown performance improved to a maximum gradient of 68 MV/m at a breakdown probability of 4.8×10^{-1} per pulse per meter and a minimum breakdown probability of 3×10^{-2} at a gradient of 63 MV/m, both at 150 ns pulse length. This initial processing was very promising; the breakdown rate improved by nearly two orders of magnitude and was at the desired minimum measurable value. Increasing the input power did not, however, result in a predictable increase in the breakdown probability. The results of Phase 1 of testing are shown in Fig. 7-10, with the breakdown probability prior to processing shown in red and the final breakdown probabilities shown in black.

Small increases in input power, sufficient to increase the gradient by less than 5 MV/m, resulted in increases in breakdown probability of more than one order of

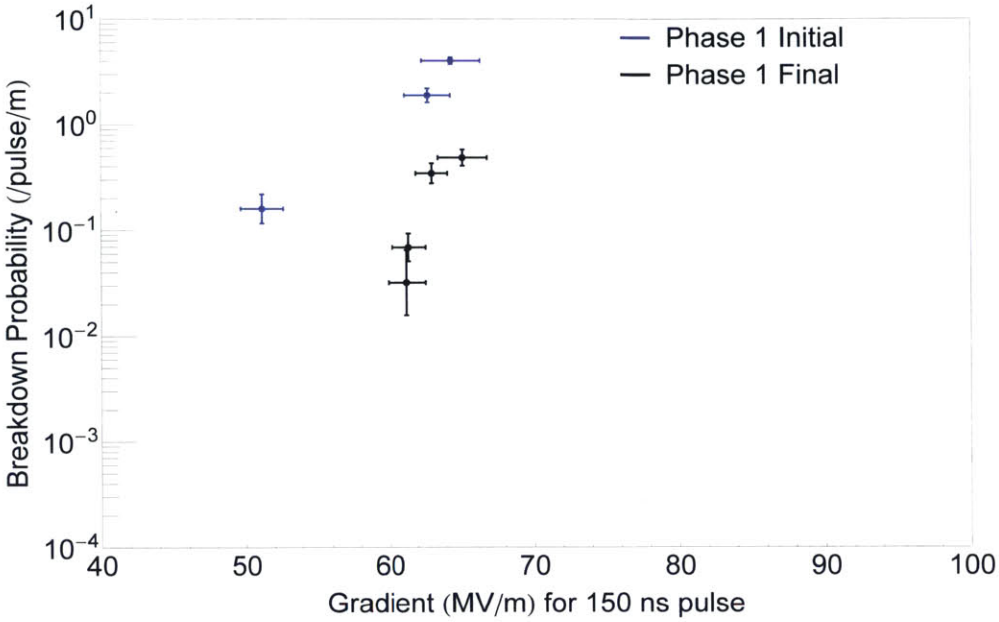

Figure 7-10: Breakdown probability as a function of gradient for Phase 1 of MIT-PBG testing. The initial data is shown in red and the data taken at the end of Phase 1 showing processing is shown in black.

magnitude. This breakdown behavior was also qualitatively different than the behavior seen during the initial processing. Instead of seeing a large number of breakdown initiations (i.e. separate breakdown events) with approximately 1-5 breakdowns per event, above 65 MV/m most breakdowns occurred as chains with 10 or more breakdowns. Typically operator intervention prevented these chains from continuing beyond 10 breakdowns, although testing showed that there was no obvious indication that the chains would stop without intervention. This behavior is referred to here as thresholding.

This thresholding behavior was unexpected. The gradient reached prior to thresholding was much lower than anticipated based on the SLAC testing, and the sharp increase in breakdown probability was not consistent with the processing of other types of structures at MIT. In an effort to determine what was limiting the operation, the structure was removed, cold tested, and disassembled; this ended Phase 1 of the testing. The disassembly of the structure revealed that breakdowns were occurring at the Pearson's rf flange joining the mode launcher and the structure. It

is believed that these breakdowns occurred because the copper gasket in the joint was not compressed uniformly, resulting in an interruption in the surface currents in the input waveguide where it passed through the flange junction. The disassembled structure components were baked at 180 °C for 2 days before being reassembled and reinstalled to begin Phase 2 of the testing.

7.2.5 Phase 2

In order to avoid any gaps in the flange junction during Phase 2 of testing, extra care was taken to ensure that the joint was very tight. The structure was also intentionally operated off-resonance for short periods during all subsequent phases of testing to ensure that all breakdowns were coming from the resonant structure. If breakdowns still occur when the structure is being operated more than 10 MHz off-resonance, at which point essentially zero power couples into the cavities, then these breakdowns can be assumed to come from the structure-launcher joint; no such breakdowns were observed during Phase 2.

After reinstalling the structure there was a brief processing period to return to the prior operating values. After two days of running at a pulse length of 150 ns during Phase 2 the gradient was back to 59 MV/m at a breakdown probability of 0.14, however at this point another power threshold was observed. In order to confirm that the new threshold, which was approximately 5 MV/m lower than during Phase 1, was the result of the fields in the structure and not the result of undetected breakdowns at the structure mode launcher junction the structure was promptly removed a second time. At this time a shim was also fabricated to improve the reliability of the joint between the structure and mode launcher.

After removal the structure was again examined visually and tested on the vector network analyzer. Small shifts in the resonant frequency of approximately 1-2 MHz were observed during this and other tests, however this is likely due to slight variations in assembly of the clamped structure.

7.2.6 Phase 3

Prior to beginning Phase 3 of testing the chamber was baked, with the structure inside, at approximately 140 °C for 2 days to lower the pressure in the chamber. Testing during Phase 3 began with attempts to push the structure past the power threshold observed during Phases 1 and 2. This was done by operating at a much shorter pulse length of approximately 60 ns flattop as opposed to the 150 ns flat-top pulse length used in Phases 1 and 2, then slowly increasing the power until a threshold was found. Power was reduced by approximately 10% from this threshold value, and the pulse length was slowly increased to the previous operating condition of 150 ns flat top. The pulse length was then dropped back to 60 ns flat top and the power level increased again.

Following this cyclic procedure of first increasing the maximum input power and then increasing the pulse energy, the structure returned to a gradient of approximately 65 MV/m at a 150 ns flat top pulse length, but a threshold was observed above this gradient. At this point the structure was allowed to operate with near constant breakdowns to test the theory that more breakdown events would process the structure through the power threshold. After several hours of operating in this condition, the structure was found to have a threshold at an even lower gradient. This was the first sign of hysteresis within the structure, whereby a large number of breakdowns at the gradient threshold brings the threshold down and the structure must be slowly processed back to the original gradient.

To determine the effects of this hysteresis and confirm the breakdown probability, the structure was operated at a consistent power level and pulse length of 100 ns flat top to obtain reliable breakdown probabilities. The shorter pulse length of 100 ns flat top was chosen to reduce the pulse energy and, therefore, reduce the likelihood of creating chains of breakdowns. This operation showed a maximum gradient of 54 MV/m at a breakdown probability of 6×10^{-2} and a minimum breakdown probability of approximately 1×10^{-2} at a gradient of 52 MV/m. Continued testing at 100 ns flat top only resulted in the gradient decreasing, as seen in blue in Fig. 7-11, showing the

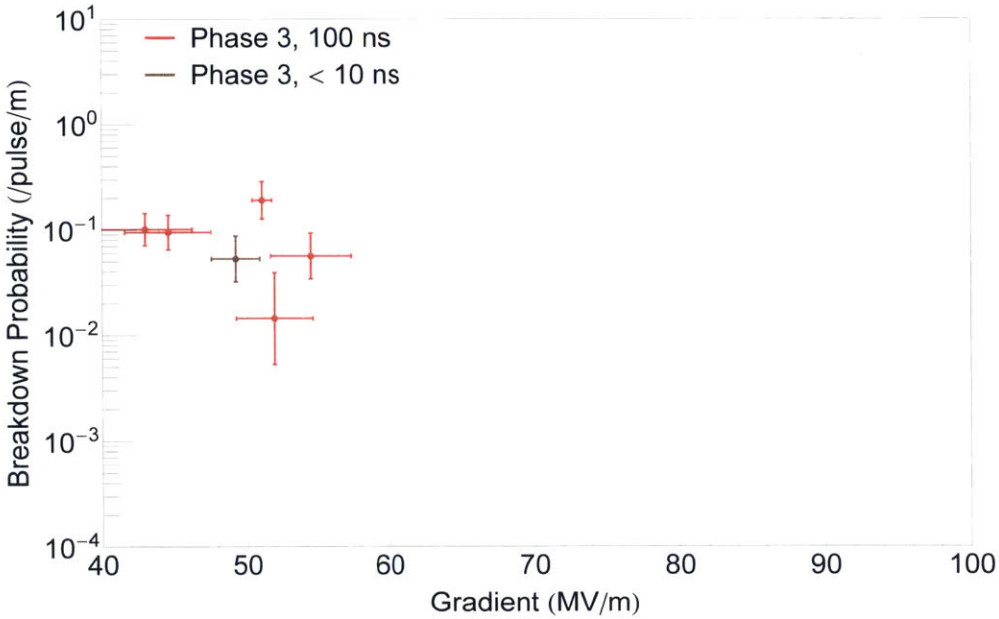

Figure 7-11: Breakdown probability as a function of gradient for Phase 3 of MIT-PBG testing for pulse lengths of 100 ns (blue) and less than 10 ns (brown).

combined breakdown probability versus gradient for Phase 3 of testing. Note that the two data points with larger error bars come from the same day of testing, during which an unknown error resulted in corruption of each saved trace. The data for these days was reconstructed from the manually recorded values, resulting in larger error bars.

After the data shown in Fig. 7-11 was collected, the pulse length was decreased to less than 10 ns flat top to determine if higher gradients and therefore surface electric fields could be supported by the structure for short times. This very short pulse operation showed no increase in gradient relative to the testing immediately prior, however the breakdown probability of 5×10^{-2} per pulse per meter at 49 MV/m was a decrease of one order of magnitude. This data point is shown in brown in Fig. 7-11. This suggests that the limiting factor in the testing was the surface electric field. If pulsed heating was playing a limiting role, the threshold gradient should increase at very short pulse lengths. After confirmation that the structure was indeed limited to gradients well below 60 MV/m after all of the testing, the structure was removed

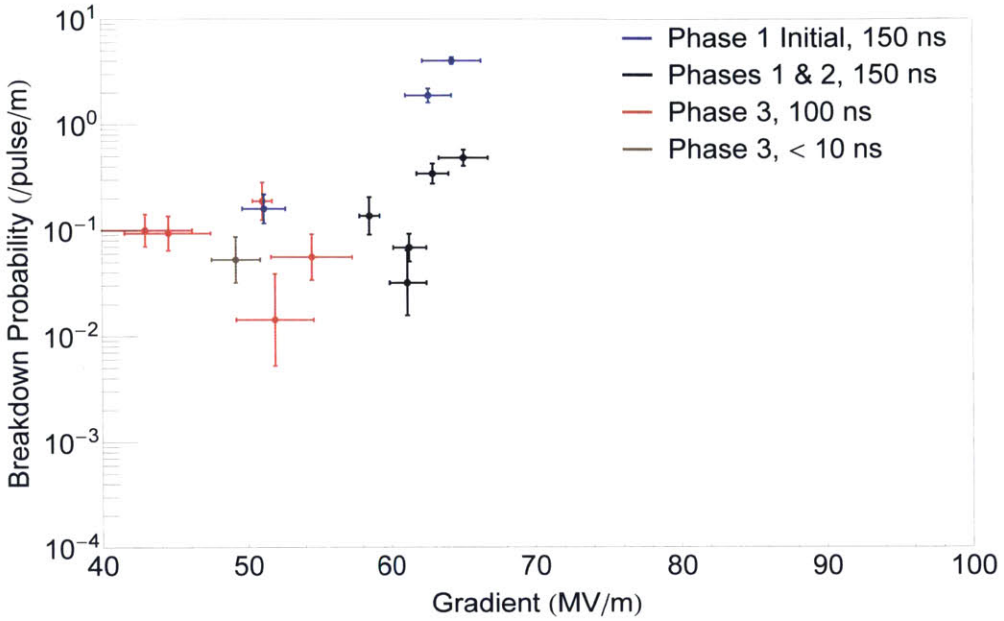

Figure 7-12: Breakdown probability as a function of gradient for all 3 phases of MIT-PBG testing. The data from Phases 1 and 2, both taken at 150 ns, are shown in black. The initial testing during Phase 1 is shown in red, and the two pulse lengths from Phase 3 are shown in blue for 100 ns and brown for less than 10 ns.

from the chamber for final cold testing and autopsy.

The combined results of all three phases of testing are shown as a function of gradient in Fig. 7-12. The data from Phases 1 and 2, both taken at 150 ns, are combined into a single data set, shown in black. The initial testing during Phase 1 is again shown in red, and the two pulse lengths from Phase 3 are shown in blue for 100 ns and brown for less than 10 ns. The regression of the structure from the maximum gradient seen in Phase 1 to the final gradient and breakdown probability, consistent with the initial testing, can be seen.

These combined results can also be plotted as a function of pulsed heating, as shown in Fig. 7-13. The data is again shown with Phases 1 and 2 in black, and Phase 3 in blue and brown for 100 ns and less than 10 ns respectively. These data show that the structure was operated at a modest temperature rise of not more than 80 K. While this temperature is above the predicted limit of 50 K for long-term operation, the total number of pulses seen by the MIT-PBG structure is small compared to the

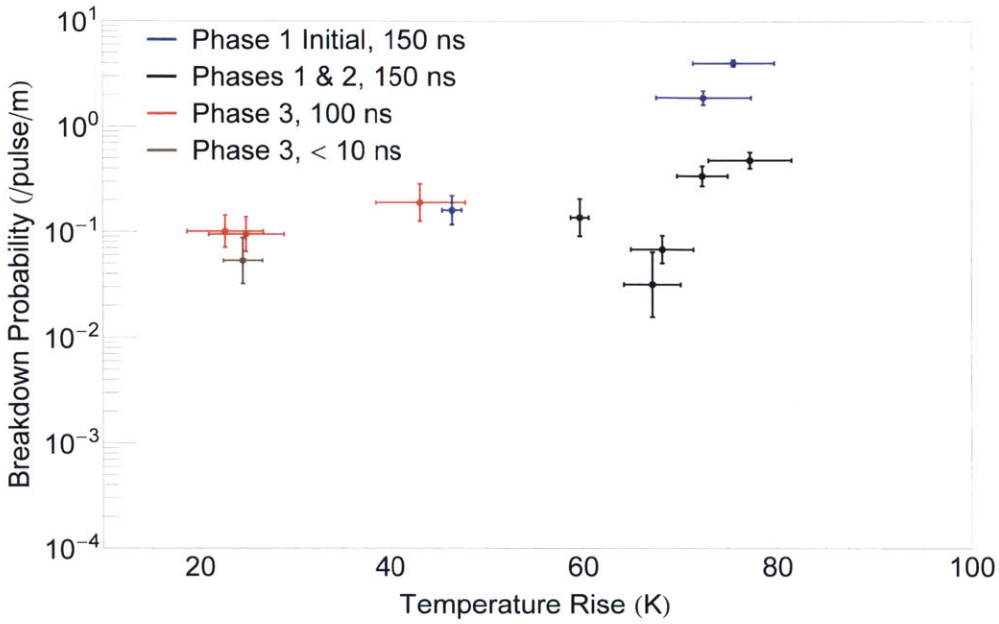

Figure 7-13: Breakdown probability as a function of pulsed heating for all 3 phases of MIT-PBG testing. The data from Phases 1 and 2, both taken at 150 ns, are shown in black. The initial testing during Phase 1 is shown in red, and the two pulse lengths from Phase 3 are shown in blue for 100 ns and brown for less than 10 ns.

SLAC testing, and no pulsed heating damage is expected.

7.2.7 Comparison with Haimson 17 GHz Accelerator Structure

The performance of the MIT-PBG structure can be compared to other accelerator structures tested at 17 GHz at MIT. A comparison with the MIT-DLWG structure will be presented in Sec. 7.3, a 22-cell traveling-wave DLWG linac structure has been tested at MIT by Haimson; the results are shown in [60]. The structure reached a maximum gradient for a pulse length of 160 ns of approximately 70 MV/m while limited to a maximum steady-state breakdown probability of approximately 8×10^{-3} per pulse per meter of structure after 1.2×10^{5} pulses. This is comparable to the performance of the MIT-PBG structure. The resonant ring structure used for the Haimson linac testing also directs incident power away from the structure in the event

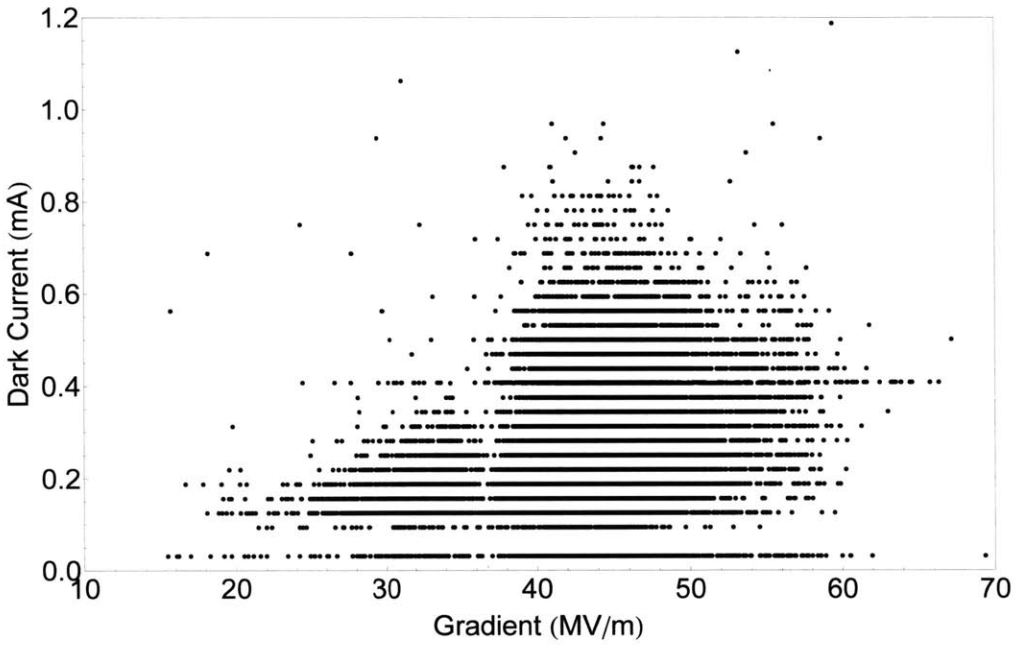

Figure 7-14: Dark current in mA as a function of gradient in MV/m for one day of testing of MIT-PBG structure. A representative sampling of the data is shown.

of a breakdown, preventing the hysteresis behavior seen in the MIT-PBG testing.

7.2.8 Dark Current

The dark current in the MIT-PBG structure was not a useful metric in determining processing. It was not seen to scale with gradient as predicted, as shown in Fig. 7-14. Because dark current is predicted to decrease at a constant gradient during processing, this lack of correlation made it impossible to use dark current in evaluating whether or not the MIT-PBG structure was processing. The scale of the dark current seen in MIT-PBG testing is also much smaller than the scale of the dark current seen in later MIT-DLWG structure testing. This result is consistent with the SLAC PBG-E structure testing, during which no measurable dark current was observed.

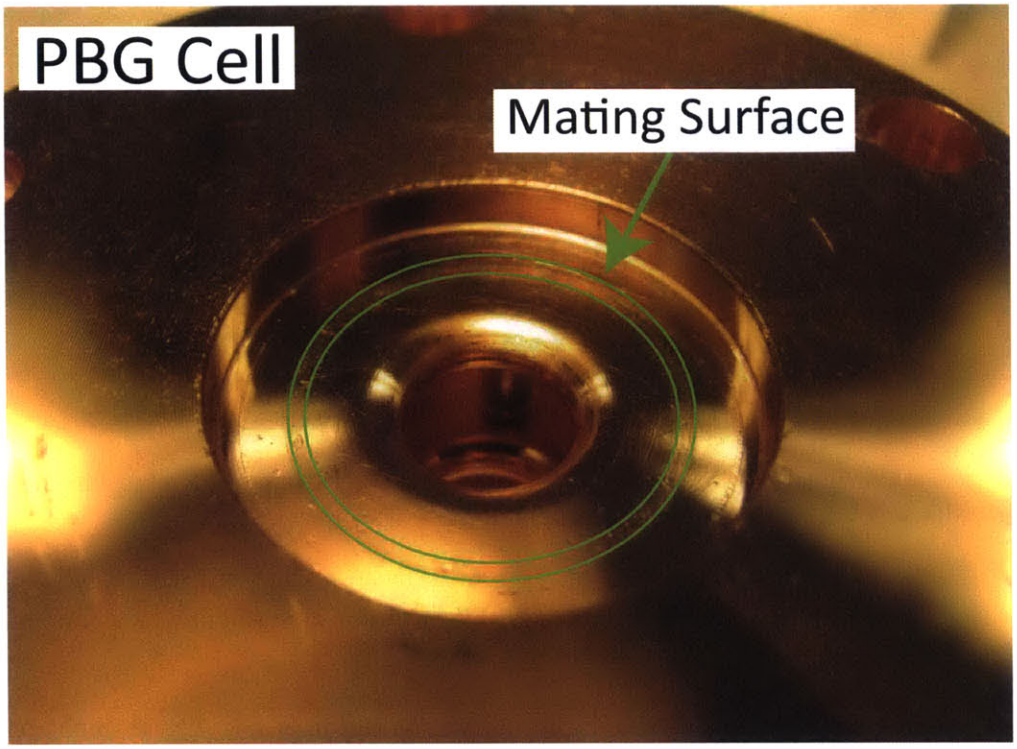

Figure 7-15: An optical microscope image of the mating surface on one side of the 17 GHz PBG cell, showing uniform contact between the coupling cell and the PBG cell, as outlined in green.

7.2.9 Post-Testing Imaging

After the completion of Phase 3 of testing the structure was removed and disassembled for post-testing imaging of the structure. Because the high-field surfaces of the clamped structure can, in general, be well-visualized without cutting the structure, the parts were left intact for post-testing imaging. A Nikon SMZ800 stereo microscope with attached camera was used for post-testing examination of the structure; this microscope is capable of a maximum of 63X zoom.

No significant signs of damage were seen in the post-testing examination of the structure. There are signs of mechanical damage at the mating surfaces between the different cells, as seen in Fig. 7-15. The rings resulting from the mating of the difference cells can be seen at every junction and appear azimuthally uniform, indicating that the structure was evenly clamped with no gaps between the cells.

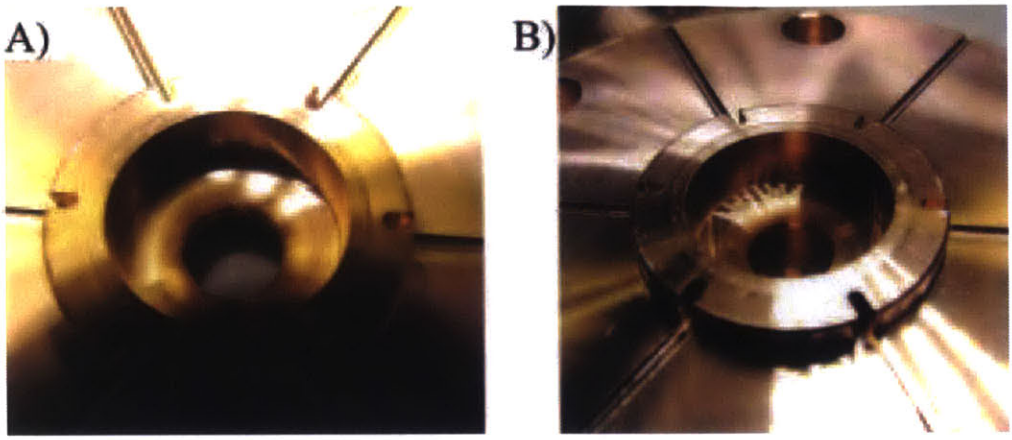

Figure 7-16: Photograph showing post-testing discoloration of the coupling iris, (A), and fillet to cutoff waveguide,(B), in the PBG structure.

Both the coupling iris and the circular fillet terminating the downstream coupling cell look rough and discolored, as seen in the low magnification pictures taken with a digital camera shown in Fig. 7-16. Similar discoloration is not seen in high magnification images of the same surfaces. This does not, however, rule out changes to the surfaces such as an increase or decrease in surface roughness, which can cause similar changes in surface appearance.

Examination of the central cell is more complicated because it is brazed. The surfaces of this brazed cell look in general shinier and cleaner than the coupling cells. The end surfaces of the coupling cells show obvious scratches and tool marks under magnification, as well as some splotches which suggests the possibility of breakdowns at the mating surface between the cells, see Fig. 7-17. Any damage at the mating surface due to breakdowns is minimal, meaning that it was not the limiting factor in performance of the structure. There is also some discoloration on the outer surfaces of the irises themselves, which can be seen in Fig. 7-18 in comparison to an untested iris from the MIT-DLWG structure.

Looking from the upstream side of the cell at the inner surface of the downstream iris (i.e. the surface facing the rods, on which the field is highest), small white spots are visible. These spots are typical of breakdown damage at high surface electric field locations, as evidenced by similar spots seen on the inner surface of the PBG-E

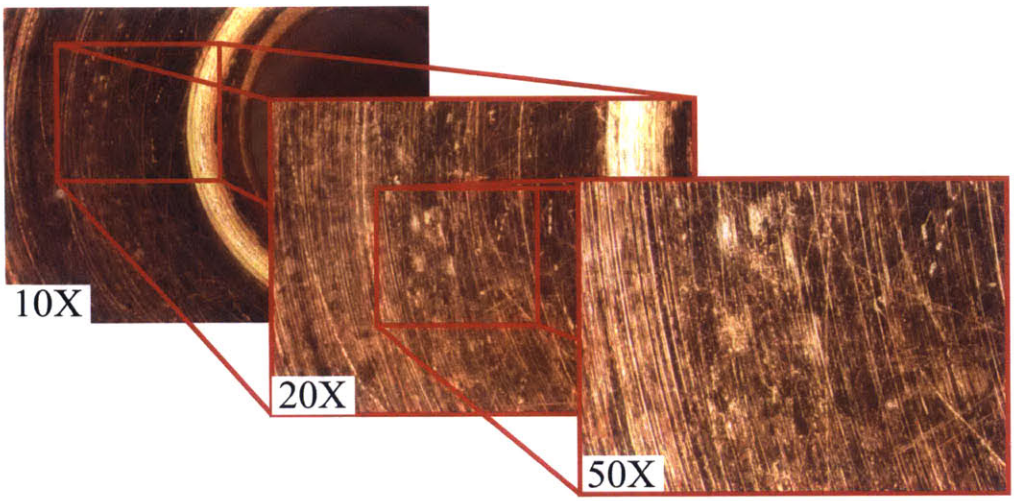

Figure 7-17: A series of optical microscope images at increasing magnification showing the end plate of the upstream coupling cell, showing tooling marks and some possible breakdown damage (splotches). Total magnification for each image is shown in the bottom left.

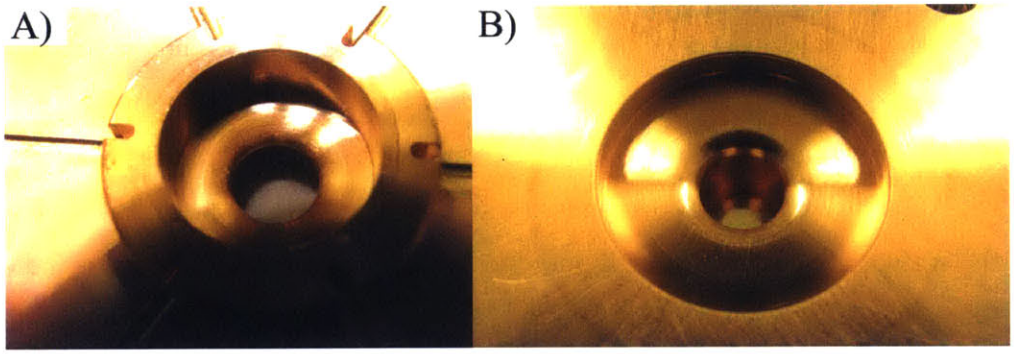

Figure 7-18: An optical microscope comparison of the input coupling iris of the PBG structure after testing, as seen from inside the coupling cell, (A), with an iris on the DLWG structure prior to testing, (B).

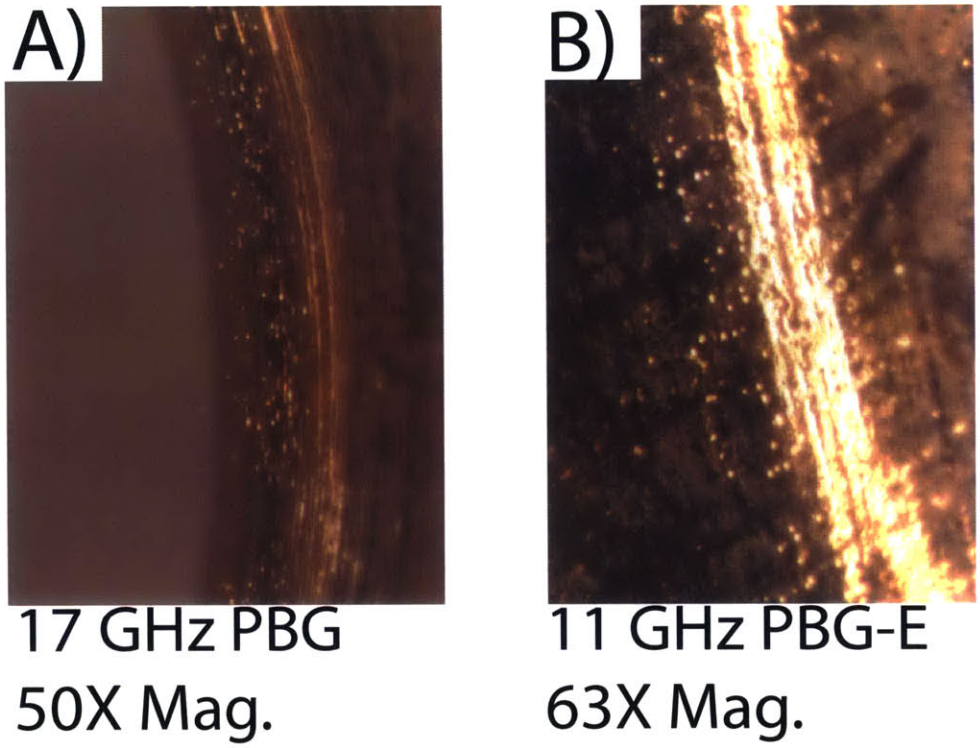

Figure 7-19: A comparison of optical microscope images of one of the high-gradient irises of the 17 GHz PBG (A) and 11 GHz PBG-E (B) structures.

high-field irises. Microscope images of these two irises are compared in Fig. 7-19.

While the breakdown spots seen on the MIT-PBG and SLAC PBG-E irises look similar, the overall surfaces of the two structures look very different. Both structures were specified to have the same surface finish, but the SLAC structure is generally very smooth while the MIT structure shows significant tooling marks. An image of the SLAC structure prior to testing is not available, so it is not clear if the smoothness of the surface is the result of high-power processing of the surface or if it is indicative of the initial surface finish. It is clear, however, that the MIT-PBG structure did not achieve the same post-testing surface seen in the SLAC structure.

In addition to differences in surface finish, the high-field side of the rods of the MIT-PBG structure looks very different from the high-field sides of the rods of the SLAC PBG-E structure. An image of one rod of the MIT-PBG structure at 10X magnification is shown in Fig. 7-20. This image is taken looking through all three

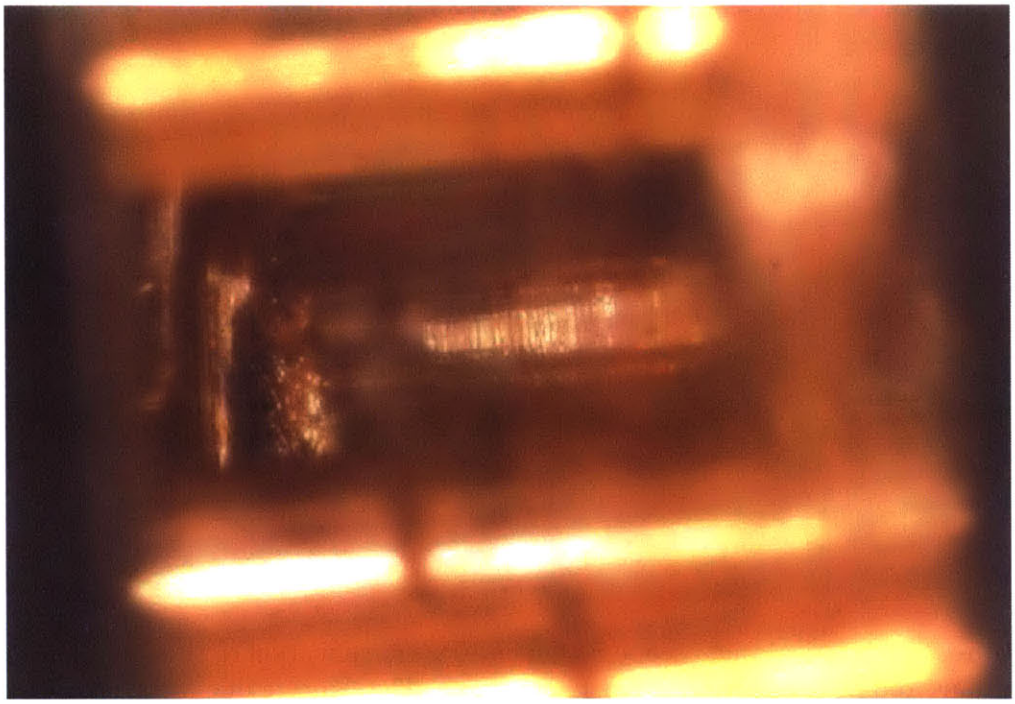

Figure 7-20: Optical microscope image at 10X magnification of the high-field side of an inner rod of the MIT-PBG structure. The image is taken looking through the rods, which creates a foreground blur. No evidence of pulsed heating damage is visible. Some breakdown damage can be seen on the braze material (left).

layers of rods opposite the desired rod, resulting in foreground blur. The machined surface of the rod can, however, still be seen, and no evidence of pulsed heating damage is visible. This is consistent with the low pulsed heating values calculated for the structure testing. Some evidence of breakdown damage in the form of white spots is visible on the braze material on the left of the image.

In contrast to the clear tool marks and generally smooth finish of the MIT-PBG structure, the high-field surface of the rods of the SLAC PBG-E structure shows significant damage. A view of one rod, also at 10X magnification, is shown in Fig. 7-21, with the iris visible at the left of the image. This rod shows significant damage, as evidenced by the smoothness of the top and bottom edges of the rod, which saw very little magnetic field, compared to the roughness in the center where the magnetic field is highest.

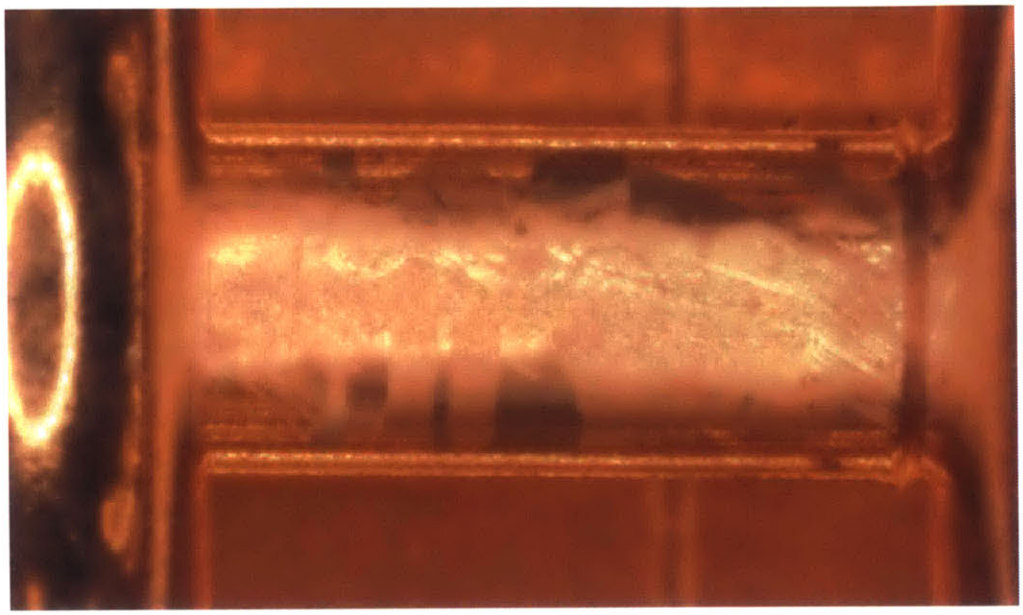

Figure 7-21: Optical microscope image at 10X magnification of the high-field side of an inner rod of the 11 GHz PBG-E structure. The damage due to pulsed heating is clearly visible. One iris is visible on the left of the image.

7.3 DLWG Experimental Results

7.3.1 Testing Methodology

Following the discovery of hysteresis behavior in the testing of the MIT-PBG structure, the testing methodology for the MIT-DLWG structure was modified slightly from the testing methodology for the MIT-PBG structure. In order to avoid regression to lower gradients or higher breakdown rates, the number of consecutive breakdowns in the MIT-DLWG structure was limited to 10 for the duration of testing, with a target of not more than 5 consecutive breakdowns. Because the surface magnetic fields in the DLWG structure are so much lower, there is no concern about pulsed heating in testing this structure.

The MIT-DLWG structure began testing at a flat-top pulse length of 100 ns, as opposed to the 150 ns target for the MIT-PBG structure. This was both because the final testing of the MIT-PBG was conducted at 100 ns, and to limit the pulse energy at high gradients in an effort to minimize consecutive breakdowns. The power in the

structure was increased slowly, keeping the steady state breakdown rate on the order of ten per hour, with the final objective of reaching a maximum gradient of at least 90 MV/m to demonstrate significant improvement over the MIT-PBG structure. The final maximum gradient achievable in the MIT-DLWG structure can be determined in future testing.

7.3.2 Testing Summary

Testing of the MIT-DLWG structure also proceeded in multiple phases. Phase 1 of testing began with the initial conditioning of the structure at a flat-top pulse length of 70 ns. This pulse length was increased to the desired 100 ns flat top after the initial day of conditioning, and the power level in the structure was increased as-tolerated by the limitation on number of breakdowns per hour. The structure reached a gradient of approximately 65 MV/m at a pulse length of 100 ns before breakdowns at the structure-launcher joint were detected. Although the same shim was used as in the final phase of the MIT-PBG testing, the limited mechanical access to the joint, which must be assembled within the chamber, resulted in a poor connection which had to be repaired.

After the poor joint between the structure and launcher was detected, the structure was removed and reinstalled with extra care to ensure a good joint. The structure was quickly reconditioned to 65 MV/m at the beginning of Phase 2 of testing, and no problems with the joint were observed. The structure was then processed at large breakdown probabilities up to a maximum gradient of 87 MV/m at a pulse length of 100 ns. Processing was observed, as both the dark current from the structure measured by the downstream current monitor and the breakdown probability at constant power levels decreased. Note the the upstream current monitor showed zero dark current for the majority of testing, but did show current during breakdown events. Above 85 MV/m a small upstream dark current signal, two orders of magnitude smaller than the downstream signal, was observed. When gradient was increased above 90 MV/m, periods of stable operation were observed before reaching a threshold-like behavior. This does not appear to be a true threshold, as continued operation at a pulse length

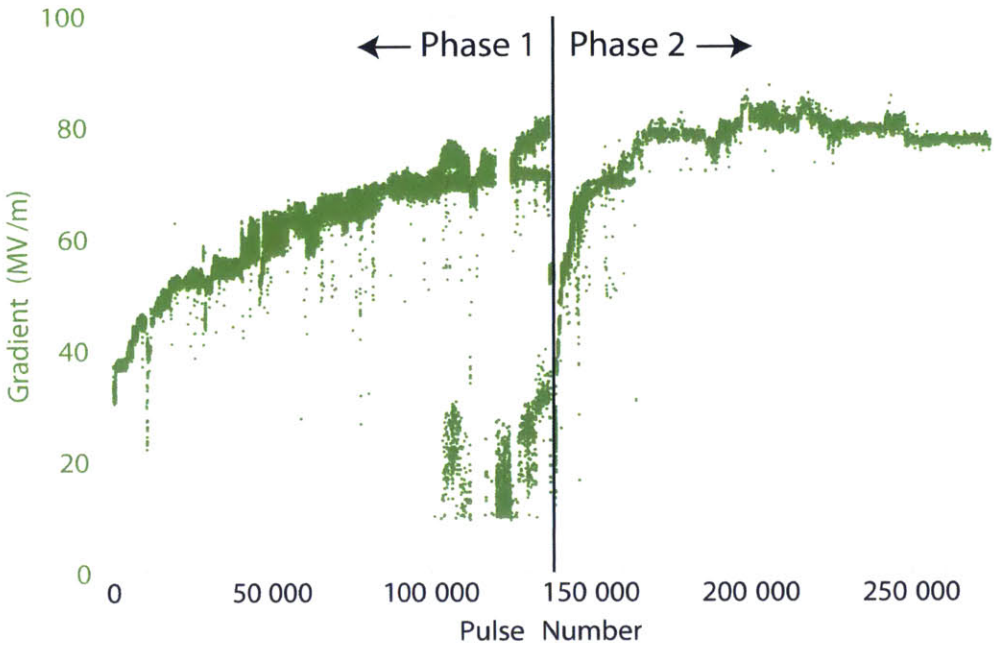

Figure 7-22: Summarized results showing the gradient for the duration of DLWG structure testing at MIT.

of 100 ns at a gradient of 90 MV/m increased the duration of these stable periods of operation at greater than 90 MV/m. The structure may be capable of reaching higher gradients with continued processing. The analyzed gradient versus total pulse number for the combined testing of the MIT DLWG structure is shown in Fig. 7-22, showing the increase in gradient with processing. In total Phase 1 comprised approximately 140,000 pulses. The rapid return to previous operating levels at the start of Phase 2 can be seen from 140,000 to 150,000 pulses into testing. Phase 2 continued for a total of 210,000 pulses, making the total number of pulses seen by the DLWG structure approximately 350,000.

7.3.3 Phase 1

The structure processed readily to a gradient of 65 MV/m at a breakdown probability of 0.63 per pulse per meter for a pulse length of 100 ns. At gradients higher than this small signals on the upstream current monitor, which typically read no dark current signal during non-breakdown operation, were observed just before the end of

the rf pulse. These small upstream current monitor signals were an order of magnitude or more below typical breakdown signals. Correlated with these signals were increases in the power reflected by the structure. This behavior is indicative of arcing or breakdowns at the structure-launcher joint; operating the structure off-resonance found that breakdowns were still occurring, confirming that the joint was contributing to the breakdown rate. The structure had previously been tested off-resonance at low power levels and no breakdowns were observed, indicating that breakdowns at the joint between the structure and launcher only began affecting performance at gradients above 60-65 MV/m for 100 ns pulses.

The structure was operated for a short time longer with a bad joint between the structure and launcher, ultimately reaching a gradient of over 77 MV/m, but with a breakdown rate skewed by the addition of breakdowns at the joint. These breakdowns also served to reduce either or both of the effective power level and effective pulse length in the structure by increasing reflection prior to power coupling into the structure. After the joint was confirmed to be affecting performance, the structure was removed, the reflection was remeasured, and the structure was reinstalled to begin Phase 2 of testing.

7.3.4 Phase 2

During Phase 2 of testing the structure was quickly returned to a gradient of 65 MV/m with only a minimal amount of processing. The power level in the structure was then increased as-tolerated by a maximum breakdown rate of 50 or more per hour during operation at 1 Hz. Although this rate is higher than the desired maximum steady-state breakdown rate, the structure was consistently in a transient condition where a higher breakdown rate can be tolerated. This transient condition was identified by both the instantaneous change in breakdown rate, i.e. time between breakdowns was generally increasing, and the decrease in dark current. The dark current was observed to increase significantly with small increases in input power, but would then decrease as the structure was operated at the same input power level. The increase in gradient at the same relatively large breakdown probability can be seen in Fig. 7-23, where

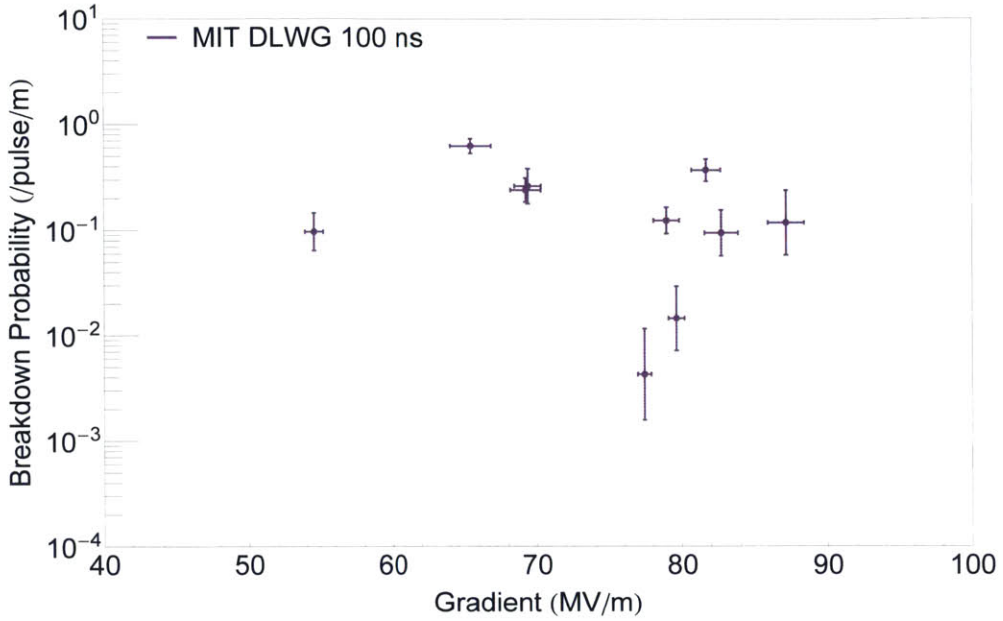

Figure 7-23: Breakdown probability as a function of gradient for the MIT-DLWG structure.

the data from Phase 1 and 2 are shown in purple. Note that this data is combined because the structure is still operating in an un-processed state during both phases, as opposed to measuring a fully- or partially-processed breakdown probability after a maximum gradient has been reached.

This processing was continued to a maximum gradient of 87 MV/m at a pulse length of 100 ns. The dark current as a function of gradient for part of this processing is shown in Fig. 7-24. The data shows a consistent increase in dark current with gradient, as expected for dark current resulting from field emission. At each increase in gradient the dark current starts out at a higher value before stabilizing. This is indicative of the surface improving with processing. This can be seen more clearly in Fig. 7-25, which shows the same data set plotted as a function of the pulse number. This is a representative sampling of the data; the structure saw approximately 40,000 pulses on this day.

This trend of increasing length of stable operation suggests that continued operation of the structure at or near 90 MV/m will result in processing and allow the

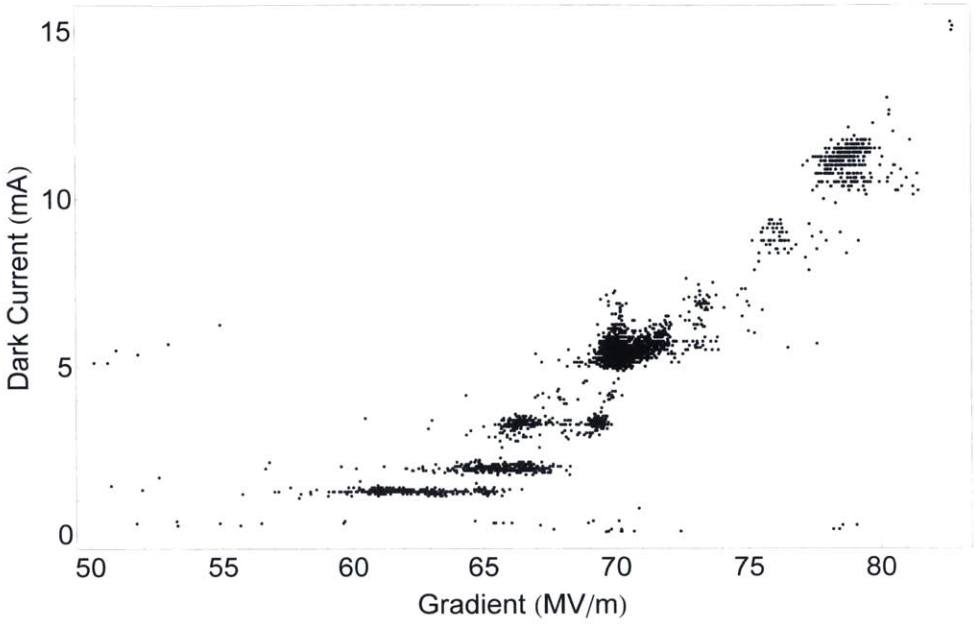

Figure 7-24: Dark current in mA as a function of gradient in MV/m for one day of testing of MIT-DLWG structure. A representative sampling of the data is shown.

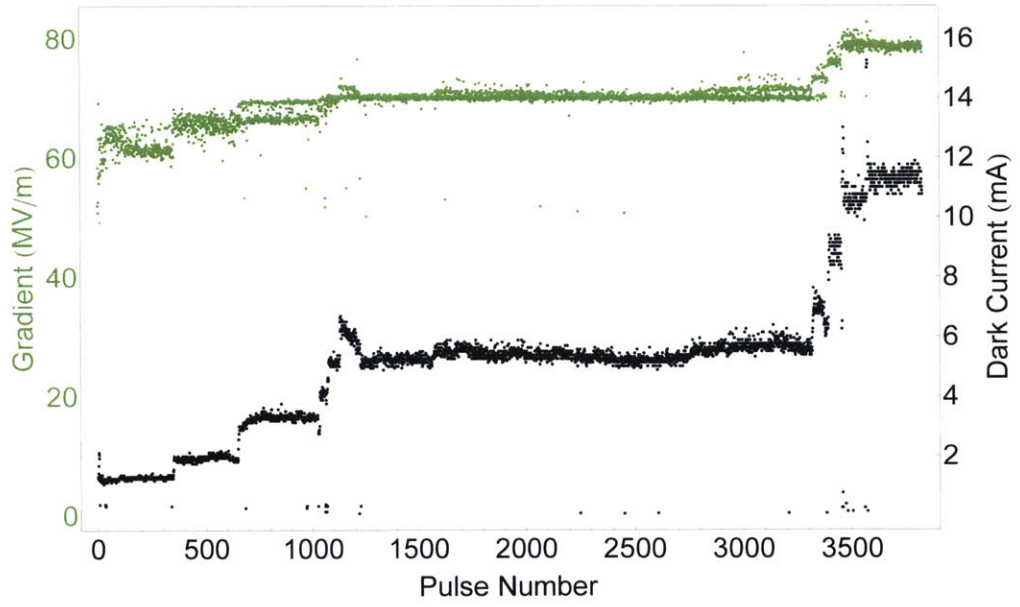

Figure 7-25: Dark current in mA and gradient in MV/m as a function of pulse number for a representative sampling from one day of testing of MIT-DLWG structure.

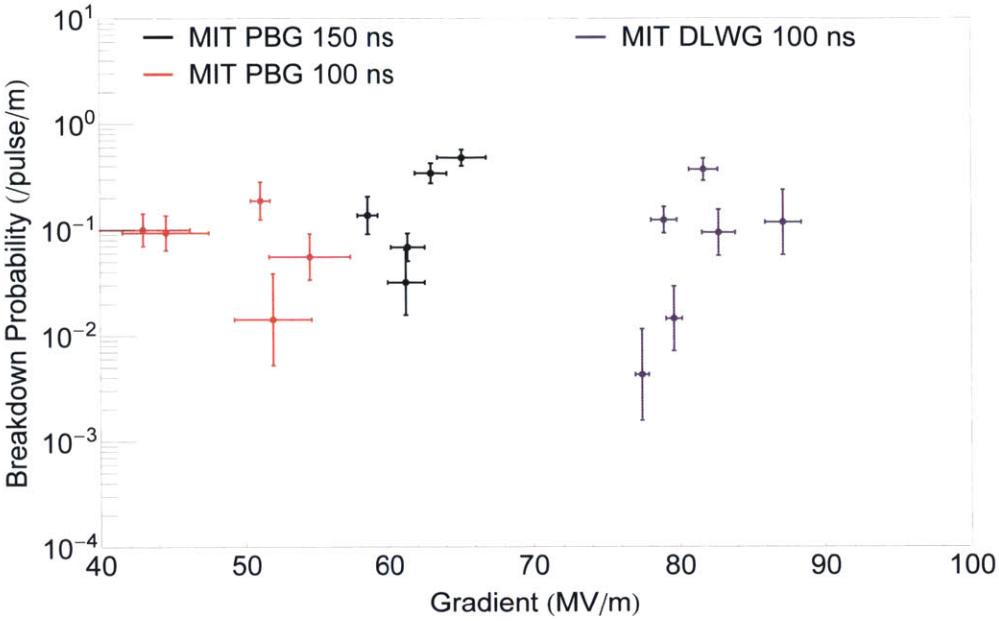

Figure 7-26: Breakdown probability as a function of gradient for the MIT-PBG and MIT-DLWG structures. Only data taken after the initial processing and at pulse lengths of at least 100 ns is shown for both structures.

gradient to be further increased. Continued operation at 87 MV/m should also decrease the breakdown probability and dark current at that gradient as the structure processes. Evidence of this processing can be seen in the multiple data points around 80 MV/m with a decreasing breakdown probability, as well as the data points at approximately constant breakdown probability and increasing gradient, as shown on Fig. 7-23.

The performance of the MIT-DLWG is shown relative to the MIT-PBG structure in Fig. 7-26. Only data taken after the initial processing and at pulse lengths of at least 100 ns is shown for both structures. This indicates that the MIT-DLWG structure both demonstrated lower breakdown probability at a higher gradient, and reached a higher maximum gradient, than the MIT-PBG structure.

7.3.5 Post-Testing Imaging

Final post-testing microscope images of the MT-DLWG structure are not available, however, digital camera images taken before and after testing show only small changes in the surfaces. A comparison of the input coupling cell before and after is shown in Fig. 7-27. The only apparent change is a ring of discoloration just radial of the iris aperture. This ring overlaps the location where the maximum surface electric field on that surface is expected, and appears to the naked eye as a change in reflectivity of the surface. This may be a visual indication of processing affecting the surface roughness. Note that, because this is a coupling cell, the expected surface electric field here is much lower than what is expected in the central cell. The coupling cells are, however, made to a rougher surface finish than the high-gradient cell, and these lower surface fields could still produce breakdowns or processing in the coupling cells.

A post-testing image of the central high-gradient cell of the DLWG structure is shown in Fig. 7-28. Some minor breakdown damage may be present around the iris, however no significant damage is visible.

7.4 Second MIT PBG Structure Experimental Results

Following the testing of the MIT-DLWG structure, the cylindrical central cell of the DLWG structure was removed and a new brazed PBG central cell was installed for testing. This structure, using the same waveguide pieces and coupling cells which were used in the MIT-DLWG testing, is referred to as MIT-PBG-2.

7.4.1 Testing Methodology

The testing of the MIT-PBG-2 structure followed the same general testing methodology used in the DLWG structure. The number of consecutive breakdowns in the MIT-PBG-2 structure was limited to 10 for the duration of testing, with a target of not more than 5 consecutive breakdowns. Because of the high surface magnetic fields

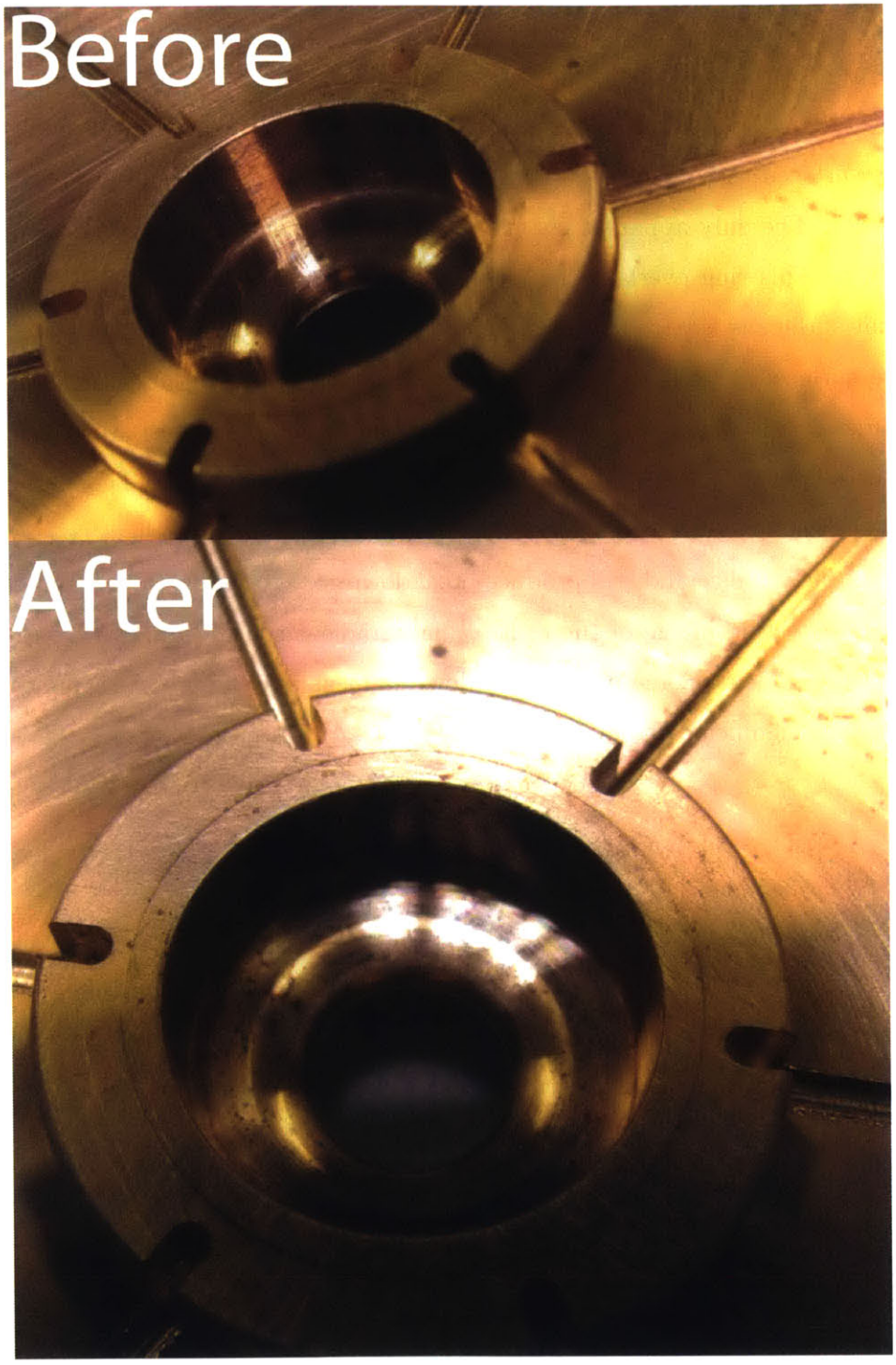

Figure 7-27: Before (above) and after (below) digital camera images of the DLWG input coupling cell. A small change in the surface at the location of highest surface electric field in the cell.

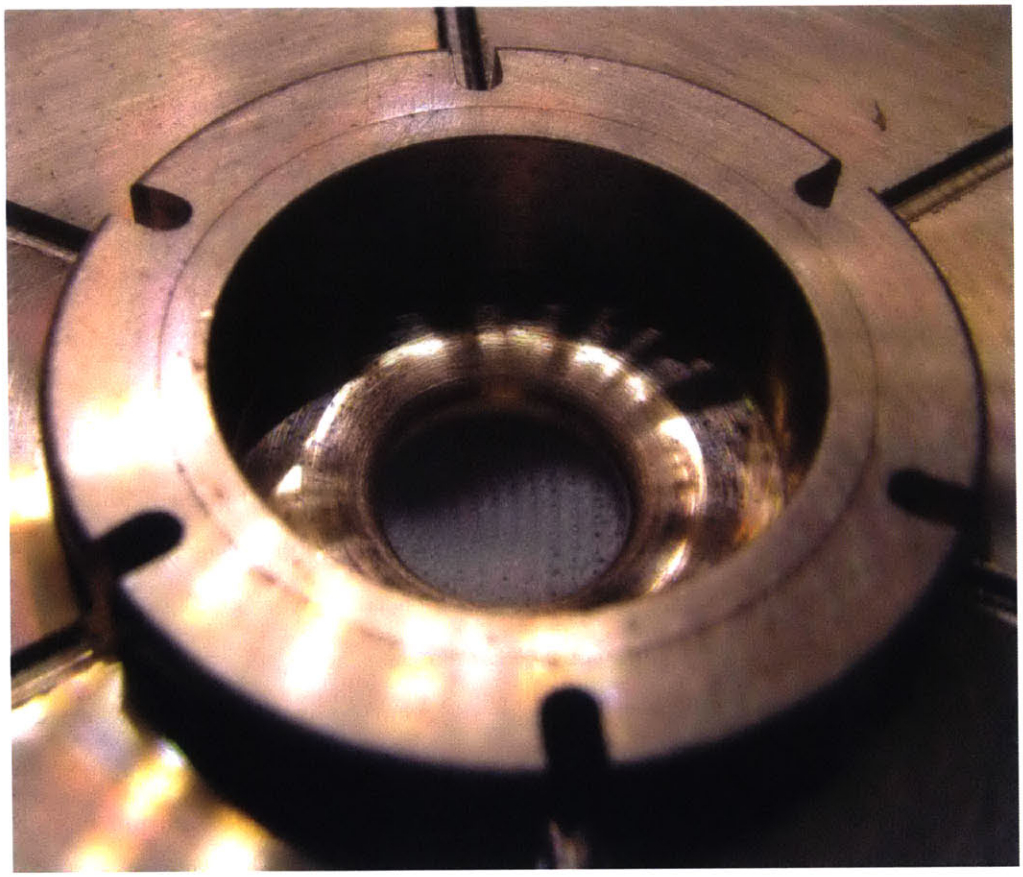

Figure 7-28: Post-testing image of the central cell of the MIT-DLWG structure. Some minor breakdown damage may be present on the iris, but no significant surface damage is visible.

present in the PBG structure, the MIT-PBG-2 structure was limited to a maximum surface temperature rise of 120 K; this is the same constraint used in the testing of the first MIT PBG structure.

Testing of the MIT-PBG-2 structure was conducted entirely at a flat-top pulse length of 100 ns. As in the MIT-DLWG structure testing, this serves to limit the pulse energy to avoid consecutive breakdowns. For the MIT-PBG-2 structure this shorter pulse length also allows higher gradients to be reached for the same temperature rise. Given this pulse length, the maximum allowed gradient for the MIT-PBG-2 structure is 90 MV/m.

7.4.2 Testing Results

Testing of the MIT-PBG-2 structure proceeded in a single phase, with no problems at the joint between the structure and mode launcher observed. Processing of the structure proceeded extremely quickly, with the structure ultimately reaching the maximum allowed gradient of 90 MV/m in fewer than 50,000 pulses. This is in contrast to the MIT-PBG structure, which saw nearly 500,000 pulses and never reached 90 MV/m, and the MIT-DLWG structure which took over 300,000 pulses to reach a gradient of 90 MV/m. Very few total breakdowns were observed during this processing, and almost all of those breakdowns occurred in groups of fewer than five events. The gradient, temperature rise, and total number of breakdowns during testing can be seen in Fig. 7-29. It is expected that, if the temperature limit was relaxed, the structure would achieve higher gradients at the same pulse length without any limiting behavior due to breakdowns.

The MIT-PBG-2 structure reached a maximum gradient of 89 MV/m at pulse length of 100 ns and a breakdown probability of 1.09×10^{-1} per pulse per meter of structure. This breakdown probability was consistent throughout the duration of processing the structure from approximately 65 MV/m to the maximum gradient of 89 MV/m. This processing was achieved in approximately 50,000 pulses and represents two days of structure testing. During processing the power is increased such that the breakdown probability remains relatively constant; if the probability is too high the

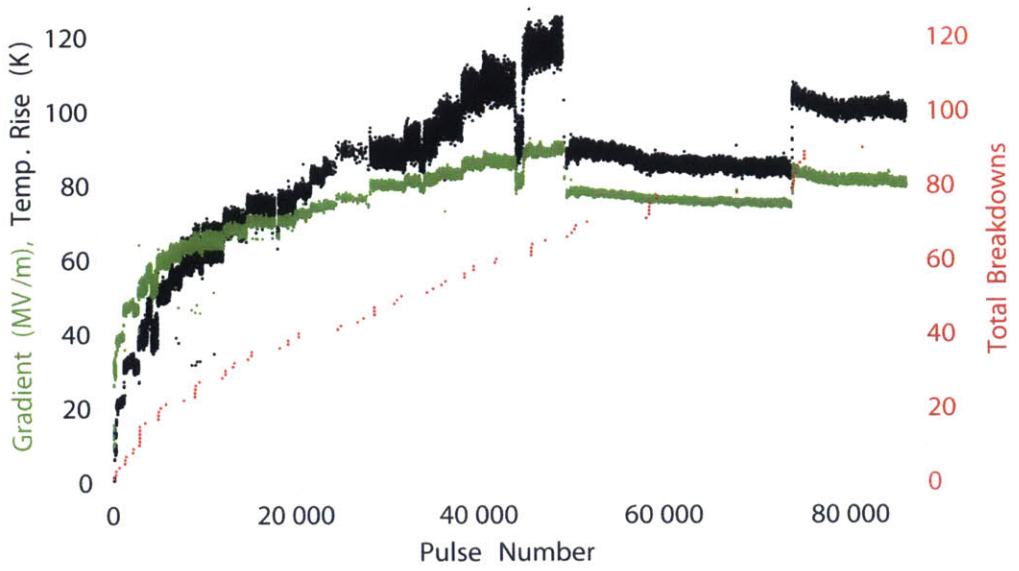

Figure 7-29: Summarized results showing the gradient (green), temperature rise (black), and total number of breakdowns (red) for the MIT-PBG-2 testing. Note the extremely low breakdown rate even during initial processing.

structure may be damaged and if the probability is too low the structure does not process efficiently. This processing can be seen in Fig. 7-30 as the series of data points at constant breakdown probability of 1.09×10^{-1} per pulse per meter of structure. The initial processing to 65 MV/m happened very quickly and is not shown on Fig. 7-30.

Once the maximum gradient was confirmed, the power was reduced to begin collecting statistics to determine the breakdown probability at gradients below the maximum processed value. Because the overall breakdown probability in the PBG-2 structure is low, it is more difficult to obtain a sufficient range of breakdown probabilities without going above the allowed gradient. This necessitates longer periods of operation at a fixed gradient, as seen in Fig. 7-29 above 50,000 pulses. The minimum breakdown probability was 3.2×10^{-2} per pulse per meter of structure at a gradient of 76 MV/m and a pulse length of 100 ns. This is nearly identical to the breakdown probability of 3.3×10^{-2} per pulse per meter of structure at a gradient of 81 MV/m and a pulse length of 100 ns obtained later in testing. This suggests that the structure has not reached a final steady-state breakdown probability, and more testing is

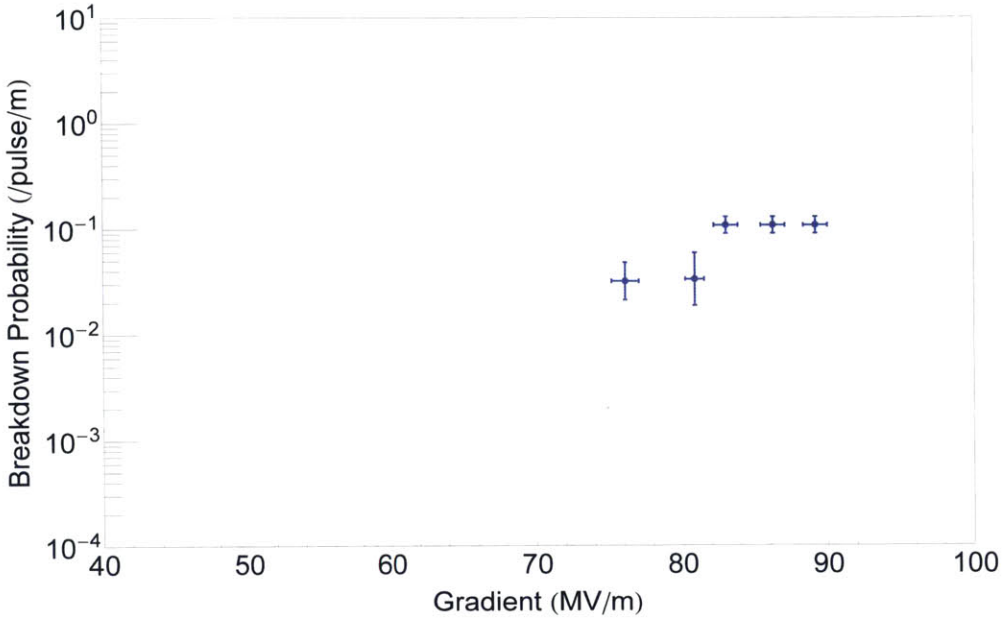

Figure 7-30: Breakdown probability as a function of gradient for the MIT-PBG-2 structure.

required to determine the final performance of the structure.

One possible explanation for the rapid processing of the MIT-PBG-2 structure is the use of the coupling cells from the MIT-DLWG structure. These cells were already processed up to a gradient of 90 MV/m during the MIT-DLWG testing, and the post-testing imaging shown in Sec. 7.3.5 did show minor surface changes as a result. This does not explain why the original MIT-PBG structure did not reach the same final gradient as the MIT-DLWG and MIT-PBG-2 structures, however it does suggest that smoother surface finishes on the coupling cells may reduce processing time in future testing. Given the reduced repetition rate of MIT testing relative to SLAC testing, decreasing the number of pulses required for processing would be a major improvement for structure testing at MIT.

7.4.3 Post-Testing Imaging

Because the MIT-PBG-2 structure is currently under test, no post-testing imaging is available.

7.5 Comparison With SLAC Data

The breakdown probabilities as functions of gradient for the MIT-PBG, MIT-DLWG, MIT-PBG-2, SLAC PBG-R, SLAC PBG-E, and SLAC DLWG structures are shown in Fig. 7-31. Only pre-hysteresis data is shown for the MIT-PBG structure, while for the MIT-DLWG structure only data taken after the structure returned to high-gradient operation during Phase 2 is shown. Because of the limited amount of data available for the MIT-PBG-2 structure, all data for that structure is shown. The SLAC data is only shown for a flat-top pulse length of 150 ns, as this is the shortest pulse length tested at SLAC. Because of the change in frequency, however, the number of rf periods, which may be more relevant to the breakdown probability than the total pulse length, is the same between a 150 ns pulse at 11.4 GHz and a 100 ns pulse at 17.1 GHz.

The MIT-PBG structure performed anomalously poorly as compared to both the PBG-R structure on which it was based and the DLWG and PBG-2 structures tested at MIT. The reason for this performance is not clear. Given that both the MIT-DLWG structure and MIT-PBG-2 structure performed much closer to the SLAC PBG-R structure, and did not reach a fundamental limit in gradient during testing, it is likely that the performance of the MIT-PBG structure is not representative of high-gradient structure testing at 17 GHz. The MIT-DLWG and MIT-PBG-2 structures do represent significant improvements in structure preparation, assembly, and testing methodology at MIT, all of which could contribute to the improved performance of these structures. The hysteresis and overall decreasing performance of the MIT-PBG structure suggest that the testing methodology used for that structure negatively affected results. Using the improved methodology developed for the MIT-DLWG structure could improve the final results for testing of an additional PBG structure at MIT.

Further testing of the MIT-PBG-2 should continue to show improvements in achievable gradient and breakdown probability. Both the MIT-DLWG structure and the MIT-PBG-2 structure have seen fewer than 10^6 pulses, which is an order of mag-

nitude fewer pulses than in typical testing at SLAC. Breakdowns are assumed to be a necessary step in rf processing, i.e. the structure must see a large number of breakdowns prior to being fully processed. Provided that the hysteresis observed in the MIT-PBG testing can be avoided, additional breakdowns should continue to process the MIT-DLWG structure.

It is important to note that, while the MIT-PBG structure is based on the SLAC PBG-R structure, there is no evidence that the MIT-PBG structure suffered the same catastrophic damage early in testing that limited the performance of the PBG-R structure. The hysteresis behavior seen in the MIT-PBG structure did result in a lower final gradient, but this decrease in performance was gradual and fundamentally different than the PBG-R damage, which occurred on the rods and prior to taking significant usable data on the structure.

7.6 Conclusion

Testing of the MIT-PBG structure showed a maximum achievable gradient below 70 MV/m. The maximum achievable gradient decreased with additional testing of the structure, suggesting permanent damage to the surface during testing. Damage of this type was observed in the SLAC PBG-R testing as a result of extremely high surface temperature rise early in the conditioning of the structure. No such temperature rise was seen in the MIT-PBG structure. Additionally the limitation in gradient persisted even to very short pulse lengths, suggesting that the limiting factor was related to the instantaneous fields in the structure and not pulsed heating, which depends on pulse length as well. Post testing examination of the structure showed some signs of breakdown damage, but clearly indicated no significant pulsed heating damage in the MIT-PBG structure as compared to the SLAC PBG-E structure. It is therefore likely that the reduced performance of the MIT-PBG structure is the result of either a problem with the structure as-fabricated (i.e. present prior to starting high-power testing) or a problem with the testing methodology. This means that it is unlikely that the poor performance is representative of the optimal performance of a PBG

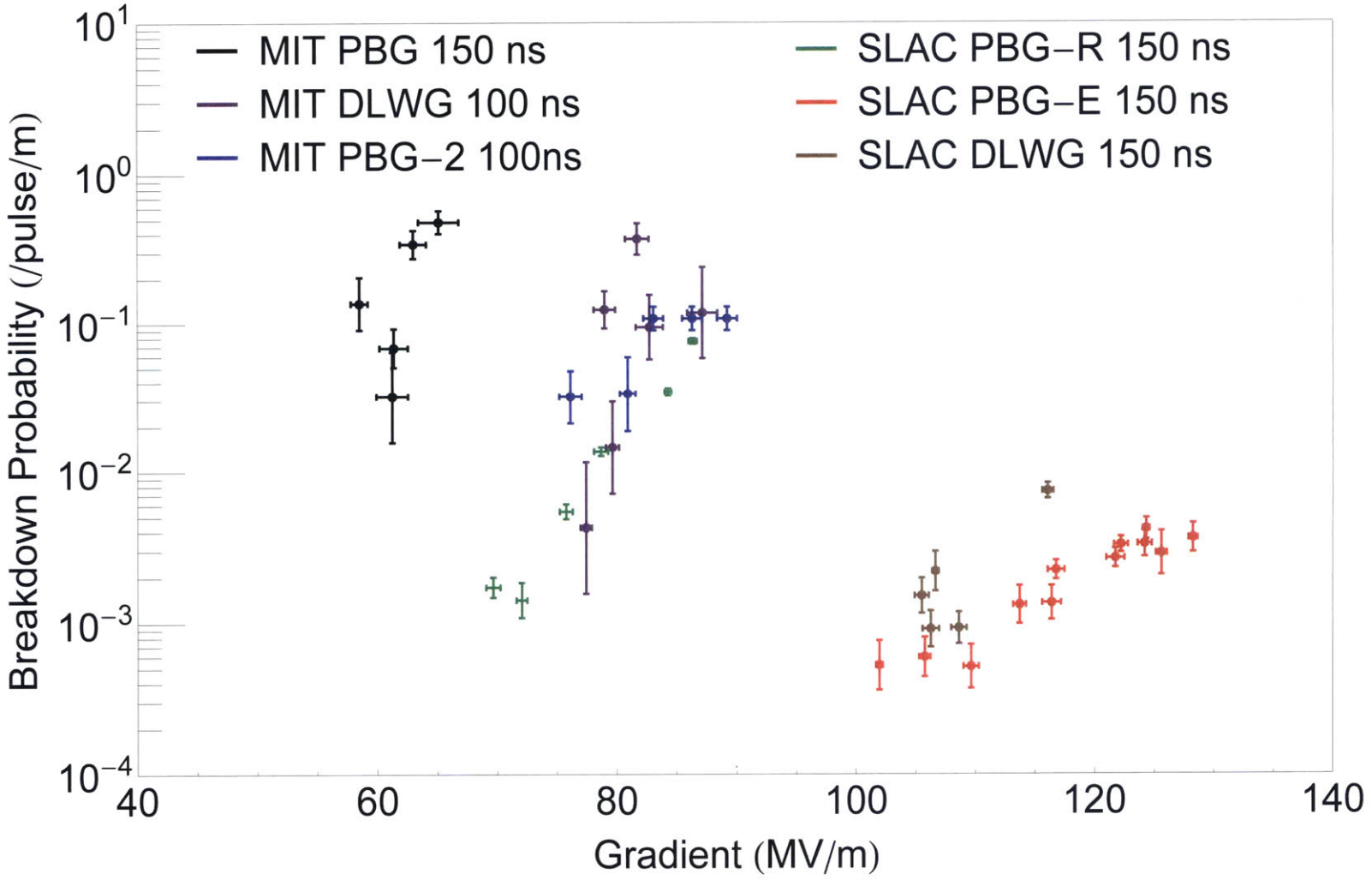

Figure 7-31: Breakdown probability as a function of gradient for MIT-PBG, MIT-DLWG, SLAC PBG-R, SLAC PBG-E, and SLAC DLWG structures. For the MIT-PBG structure only pre-hysteresis data is shown, and for the MIT-DLWG structure only data after the return to high-gradient operation in Phase 2 is shown.

structure at 17 GHz.

Following the testing of the MIT-PBG structure, a DLWG structure was tested at MIT using the same fabrication techniques, but with improvements to surface preparation after fabrication, structure assembly, and testing methodology. This structure reached a gradient of approximately 90 MV/m and continued to show improvements in achievable gradient and breakdown probability throughout testing. This suggests that the limiting factor in the performance of the MIT-PBG structure was specific to that structure, and not a fundamental aspect of structure fabrication and testing at MIT.

To verify this belief that the results obtained during testing of the MIT-PBG structure were anomalous, a second PBG structure, MIT-PBG-2, was tested. This structure reused the coupling cells from the MIT-DLWG testing, and reached a maximum gradient of 90 MV/m at a pulse length of 100 ns with very minimal processing. At this gradient and pulse length the surface temperature rise in the MIT-PBG-2 structure was 120 K, which is the maximum temperature rise allowed in the structure according to the testing methodology. Continued operation of the MIT-PBG-2 structure at lower gradients and the same pulse length of 100 ns showed both a decrease in breakdown probability with gradient as expected, and continued processing of the structure. Current results show that the MIT-PBG-2 structure performed comparably to the SLAC PBG-R structure, and that continued testing of the MIT-PBG-2 structure may improve upon this performance. The performance of the MIT-PBG-2 structure is also comparable to the performance of the MIT-DLWG structure, suggesting that PBG structures are viable candidates for future accelerator applications requiring high-gradient, low breakdown probability operation with wakefield damping.

Chapter 8

Discussion and Future Work

8.1 Summary of Results

Significant contributions to the analysis of wakefields in photonic band-gap structures have been made. Through the use of particle-in-cell simulation codes, wakefield damping in the traveling-wave PBG structure tested at MIT has been confirmed. The damping of the wakefields was found to be well-predicted by the quality factor of the respective modes from eigenmode simulations. It was found that multiple dipole modes were needed in eigenmode simulation to accurately predict the total wakefield in the structure. The PBG structure was also shown to damp wakefields relative to an undamped disc-loaded waveguide structure.

As part of an ongoing program to conduct testing on the breakdown probability of single-cell standing-wave high-gradient accelerator structures, an improved PBG structure was tested at 11 GHz at SLAC. This structure used the information obtained from a previous test of a round-rod PBG structure at SLAC (SLAC PBG-R) to improve the overall performance of the structure through the use of elliptical rods and an improved testing methodology; this improved structure is designated SLAC PBG-E.

The PBG-E structure was fabricated by collaborators at SLAC, and cold test results showed good agreement with simulation in both frequency and field profile. The structure reached gradients and breakdown probabilities comparable to those

reached by an undamped disc-loaded waveguide structure, SLAC DLWG, also tested at SLAC. Post-testing cold tests showed a small decrease in Q, and SEM imaging of the structure showed pulsed heating damage on the high-field sides of the inner rods. This damage was qualitatively different than the damage seen on the SLAC PBG-R structure. The SLAC PBG-E structure was also able to operate at similar breakdown probabilities for the same gradient at the beginning and end of testing, indicating that, unlike in the case of the PBG-R structure, the pulsed heating damage did not irrevocably alter the performance of the structure.

Subsequent to the SLAC PBG-E testing, a single-cell standing-wave PBG structure was designed and built for high-gradient testing at 17 GHz at MIT. This structure, designated MIT-PBG, was based on the SLAC PBG-R design, with modifications to allow for easier fabrication and better diagnostic access to the structure. Cold test of the structure once again showed good agreement of the experimental reflection and field profile with simulation. The MIT-PBG structure was installed and tested in three phases. Testing showed a threshold gradient, above which the breakdown probability was too high to operate, at a much lower value than predicted by the SLAC testing. This maximum gradient was also found to decrease as testing progressed. Post-testing imaging of the structure showed no indication of pulsed heating damage, in agreement with the predicted temperature rise during testing. Some breakdown damage was observed, but no significant changes in the structure as a result of the testing were present.

In order to provide a baseline for the MIT-PBG structure a disc-loaded waveguide structure, designated MIT-DLWG, was built at MIT. The MIT-DLWG structure shared components with the MIT-PBG structure wherever possible, and was fabricated using the same techniques. The structure preparation prior to installation, as well as the process of assembly and the testing protocol, were all improved for the MIT-DLWG structure relative to the MIT-PBG structure. Similarly good agreement between cold test and simulation was found for the MIT-DLWG structure. High-power testing of the MIT-DLWG structure proceeded smoothly, with the structure easily reaching gradients much larger than those seen by the MIT-PBG structure.

This is assumed to mean that there was a problem unique to the MIT-PBG structure itself, and not a fundamental problem with the testing at MIT.

This assumption was confirmed via testing of a second PBG structure at MIT, designated MIT-PBG-2. This structure was identical in design to the original MIT-PBG structure and reused the coupling cells and associated components from the MIT-DLWG structure, only replacing the high-gradient central cell. The MIT-PBG-2 structure processed very quickly, reaching the maximum allowed gradient of 89 MV/m for a 100 ns pulse length in fewer than 50,000 pulses. This gradient and pulse length correspond to a peak surface temperature rise of approximately 120 K. No thresholding behavior or significant increase in breakdown probability were seen at high gradients, and the gradient was only limited by the pulsed heating. The breakdown probability of the MIT-PBG-2 structure was comparable to the PBG-R structure tested at SLAC and the DLWG structure tested at MIT, suggesting that PBG structures are viable candidates for future accelerators even at higher frequencies.

8.2 Discussion of Relevance

The simulation of wakefield damping in PBG structures using a PIC code is a significant advance. Previous simulation work assumed that only a single dipole mode was relevant and that the Q of the mode as predicted by eigenmode simulations was an accurate measure of wakefield damping. The use of a PIC code confirmed that eigenmode Q values are appropriate measures of damping, allowing for simple estimates of damping in future designs. The use of a PIC code also indicated that eigenmode simulations must look for and include multiple dipole modes within the dipole band to accurately predict damping.

Demonstration of high-gradient, low-breakdown-probability testing of the PBG-E structure at SLAC was a ground breaking step in the advancement of PBG structures for future collider applications. While the PBG-R structure showed that it is possible for a structure with wakefield damping to operate at high gradients, it could

not do so at an acceptable breakdown probability. Proving that a structure could operate simultaneously at high gradient, low breakdown probability, and with wake-field damping makes the PBG-E structure a viable candidate for future colliders. This testing also showed that the methodology used in processing structures with high surface magnetic fields is important. It also showed that PBG structures can be modified to reduce surface magnetic fields while still operating at high fields. This technique has since been used in designs for superconducting PBG structures.

Testing of the breakdown performance of single-cell high-gradient structures at 17 GHz provides a unique opportunity to investigate the physics of breakdowns in accelerator structures. No other comparable test facility is currently available, making these experiments unique. While testing of the MIT-PBG structure did not show the results expected based on the SLAC testing, the structure also did not show damage as a result of pulsed heating. This, combined with the promising results of the MIT-DLWG structure, suggests that future testing of PBG structures at 17 GHz will provide useful comparisons to PBG structure testing at 11 GHz.

While the PBG structure inherently provides a much different ratio of surface magnetic field to gradient, the surface temperature rise caused by this magnetic field is a frequency-dependent quantity. That means that testing at higher frequencies has the potential to reveal differences in breakdown physics depending on surface magnetic fields versus actual temperature rise in a way that testing various geometries at the same frequency does not. Testing at higher frequency also provides the potential for investigating whether it is the pulse length or number of rf cycles during the pulse that affects breakdown probability.

In addition to these frequency-dependent benefits, the actual test stand at MIT provides significant opportunities for investigating the specifics of breakdowns. Because the chamber allows optical access to the inner surfaces of a PBG structure, a variety of diagnostics are available to investigate breakdowns, including the amount and location of light emitted during a breakdown, the spectrum of that light, and changes in the high-field surfaces in-situ. While these diagnostics were not available for use in the testing presented here, these experiments confirmed that the chamber

and associated rf diagnostics required work properly, allowing future work to focus on implementing more novel diagnostic techniques.

8.3 Future Work

8.3.1 Continued MIT-DLWG Structure Testing

Although the MIT-DLWG structure is currently removed, the structure could be re-installed and testing should be continued. At a pulse length 100 ns flat top, the maximum achievable gradient and subsequent fully-processed breakdown probabilities at lower gradients should be determined. After 100 ns flat top operation is completed, longer pulse lengths with higher pulsed heating should also be tested. These data would provide important reference points for comparison both with future PBG structures tested at MIT and with DLWG structures tested at SLAC and CERN.

8.3.2 Continued MIT-PBG-2 Structure Testing

Currently the MIT-PBG-2 structure has only been tested at a single pulse length. Testing at multiple pulse lengths allows the affects of pulsed heating to be separated from the affects of peak surface electric fields; this is a critical step in PBG structure testing and should be completed. After testing at multiple pulse lengths subject to a maximum pulsed heating of 120 K has been completed, the maximum gradient sustainable in the structure can be determined at 100 ns pulse length. This maximum-gradient testing will also serve to investigate the lifetime of the structure as a function of gradient.

Bibliography

[1] S. Chatrchyan et al. Observation of a new boson at a mass of 125 gev with the CMS experiment at the LHC. *Physics Letters B*, 716(1):30 – 61, 2012.

[2] G. Aad et al. Observation of a new particle in the search for the standard model higgs boson with the ATLAS detector at the LHC. *Physics Letters B*, 716(1):1 – 29, 2012.

[3] W. D. Kilpatrick. Criterion for Vacuum Sparking Designed to Include Both rf and dc. *Review of Scientific Instruments*, 28:824–826, October 1957.

[4] JW Wang and GA Loew. Field emission and rf breakdown in high-gradient room-temperature linac structures. *Proc. Joint School RF Engineering for Accelerators*, 1997.

[5] V.A. Dolgashev. In *Proceedings of IEEE Particle Accelerator Conference 2003, Portland, Oregon, 2003*, pages 1267–1269. IEEE, Piscataway, NJ, 2003. SLAC-PUB-10123.

[6] S.V. Kuzikov and M.E. Plotkin. Theory of thermal fatigue caused by rf pulsed heating. *International Journal of Infrared and Millimeter Waves*, 29(3):298–311, 2008.

[7] Brian J. Munroe, Alan M. Cook, Michael A. Shapiro, Richard J. Temkin, Valery A. Dolgashev, Lisa L. Laurent, James R. Lewandowski, A. Dian Yeremian, Sami G. Tantawi, and Roark A. Marsh. High power breakdown testing of a photonic band-gap accelerator structure with elliptical rods. *Phys. Rev. ST Accel. Beams*, 16:012005, Jan 2013.

[8] E.I. Smirnova. *Novel Photonic Band Gap structures for accelerator applications.* PhD thesis, Massachusetts Institute of Technology, 2005.

[9] Evgenya I. Smirnova, Ivan Mastovsky, Michael A. Shapiro, Richard J. Temkin, Lawrence M. Earley, and Randall L. Edwards. Fabrication and cold test of photonic band gap resonators and accelerator structures. *Phys. Rev. ST Accel. Beams*, 8:091302, Sep 2005.

[10] E. I. Smirnova, A. S. Kesar, I. Mastovsky, M. A. Shapiro, and R. J. Temkin. Demonstration of a 17 GHz, high-gradient accelerator with a photonic-band-gap structure. *Phys. Rev. Lett.*, 95:074801, Aug 2005.

[11] R. A. Marsh, M. A. Shapiro, R. J. Temkin, E. I. Smirnova, and J. F. DeFord. Measurement of wakefields in a 17 GHz photonic bandgap accelerator structure. *Nuclear Instruments and Methods in Physics Research Section A: Accelerators, Spectrometers, Detectors and Associated Equipment*, 618(1-3):16 – 21, 2010.

[12] R. A. Marsh, M. A. Shapiro, R. J. Temkin, V. A. Dolgashev, L. L. Laurent, J. R. Lewandowski, A. D. Yeremian, and S. G. Tantawi. X-band photonic bandgap accelerator structure breakdown experiment. *Phys. Rev. ST Accel. Beams*, 14:021301, Feb 2011.

[13] Gregory A Loew and JW Wang. Rf breakdown studies in room temperature electron linac structures. In *13th Int. Symp. on Discharges and Electrical Insulation in Vacuum, Paris, France*, 1988.

[14] W.J. Brown, S. Trotz, K.E. Kreischer, M. Pedrozzi, M.A. Shapiro, and R.J. Temkin. Experimental and theoretical investigations of a 17 GHz rf gun. *Nuclear Instruments and Methods in Physics Research Section A: Accelerators, Spectrometers, Detectors and Associated Equipment*, 425(3):441 – 459, 1999.

[15] W. J. Brown, S. E. Korbly, K. E. Kreischer, I. Mastovsky, and R. J. Temkin. Low emittance electron beam formation with a 17 GHz rf gun. *Phys. Rev. ST Accel. Beams*, 4:083501, Aug 2001.

[16] C. Adolphsen. Normal-conducting rf structure test facilities and results. In *Particle Accelerator Conference, 2003. PAC 2003. Proceedings of the*, volume 1, pages 668–672 Vol.1, May 2003.

[17] H. H. Braun, S. Döbert, I. Wilson, and W. Wuensch. Frequency and temperature dependence of electrical breakdown at 21, 30, and 39 ghz. *Phys. Rev. Lett.*, 90:224801, Jun 2003.

[18] A. Grudiev, S. Calatroni, and W. Wuensch. New local field quantity describing the high gradient limit of accelerating structures. *Phys. Rev. ST Accel. Beams*, 12(10):102001, Oct 2009.

[19] D.P. Pritzkau. *RF Pulsed Heating*. PhD thesis, Stanford University, 2001.

[20] David P. Pritzkau and Robert H. Siemann. Experimental study of rf pulsed heating on oxygen free electronic copper. *Phys. Rev. ST Accel. Beams*, 5:112002, Nov 2002.

[21] Lisa Laurent, Sami Tantawi, Valery Dolgashev, Christopher Nantista, Yasuo Higashi, Markus Aicheler, Samuli Heikkinen, and Walter Wuensch. Experimental study of rf pulsed heating. *Phys. Rev. ST Accel. Beams*, 14:041001, Apr 2011.

[22] J. Norem, Z. Insepov, and I. Konkashbaev. Triggers for rf breakdown. *Nuclear Instruments and Methods in Physics Research Section A: Accelerators, Spectrometers, Detectors and Associated Equipment*, 537(3):510 – 520, 2005.

[23] K Nordlund and F Djurabekova. Defect model for the dependence of breakdown rate on external electric fields. *Physical Review Special Topics-Accelerators and Beams*, 15(7):071002, 2012.

[24] A. S. Pohjonen, F. Djurabekova, K. Nordlund, A. Kuronen, and S. P. Fitzgerald. Dislocation nucleation from near surface void under static tensile stress in cu. *Journal of Applied Physics*, 110(2):–, 2011.

[25] High Frequency Structure Simulator, Ansoft Corporation, http://www.hfss.com.

[26] E.A. Nanni. *A 250 GHz Photonic Band Gap Gyrotron Amplifier.* PhD thesis, Massachusetts Institute of Technology, 2013.

[27] Carl A. Bauer, Gregory R. Werner, and John R. Cary. Origin and reduction of wakefields in photonic crystal accelerator cavities. *Phys. Rev. ST Accel. Beams*, 17:051301, May 2014.

[28] R. A. Marsh, B. J. Munroe, M. Shapiro, and R. J. Temkin. In *Proceedings of the 23rd Particle Accelerator Conference, Vancouver, Canada, 2009.* IEEE, Piscataway, NJ, 2009. WE6RFP081.

[29] R.A. Marsh. *Experimental Study of Photonic Band Gap Accelerator Structures.* PhD thesis, Massachusetts Institute of Technology, 2009.

[30] E. I. Simakov, W. B. Haynes, S. S. Kurennoy, J. F. O'Hara, E. R. Olivas, and D. Yu. Shchegolkov. WEPPP035. In *Proceedings of IPAC2012, New Orleans, Louisiana, USA*, pages 2801–2803, 2012.

[31] Computer Simulation Technology Particle Studio, CST Computer Simulation Technology AG, http://www.cst.com.

[32] Min Hu, Brian J. Munroe, Michael A. Shapiro, and Richard J. Temkin. Calculation of wakefields in a 17 ghz beam-driven photonic band-gap accelerator structure. *Phys. Rev. ST Accel. Beams*, 16:022002, Feb 2013.

[33] K. L. F. Bane, P. B. Wilson, and T. Weiland. Wake fields and wake field acceleration. *AIP Conference Proceedings*, 127(1):875–928, 1985.

[34] Perry B. Wilson. Introduction to wake fields and wake potentials. *AIP Conf.Proc.*, 184:525–564, 1989.

[35] Thomas P. Wangler. *Principles of RF linear accelerator.* John Wiley & Sons, Inc, 1998.

[36] B. W. Zotter and S. A. Kheifets. *Impedances and Wakes in High-Energy Particle Accelerators.* World Scientific, 1997.

[37] T Weiland and Bruno W Zotter. Wake potentials of a relativistic current in a cavity. oai:cds.cern.ch:124656. wakefield of a relativistic current in a cavity. *Part. Accel.*, 11(CERN-ISR-TH-80-36. ISR-TH-80-36):143–151. 22 p, 1980.

[38] B Zotter and K Bane. Transverse mode in periodic cylindrical cavities. oai:cds.cern.ch:1307879. Technical Report CERN-ISR-TH-80-25. ISR-TH-80-25, CERN, Geneva, Jul 1980.

[39] J Gao. Analytical formulae for the wakefields produced by the nonrelativistic charged particles in periodic disk-loaded structures. *Nuclear Instruments and Methods in Physics Research Section A: Accelerators, Spectrometers, Detectors and Associated Equipment*, 447(3):301 – 308, 2000.

[40] G. Dome. Wake potentials of a relativistic point charge crossing a beam-pipe gap: An analytical approximation. *Nuclear Science, IEEE Transactions on*, 32(5):2531 –2534, oct. 1985.

[41] E. Keil. Diffraction radiation of charged rings moving in a corrugated cylindrical pipe a model of radiation losses in an electron ring accelerator. *Nuclear Instruments and Methods*, 100(3):419 – 427, 1972.

[42] J. Haimson. Absorption and generation of radio-frequency power in electron linear accelerator systems. *Nuclear Instruments and Methods*, 33(1):93 – 106, 1965.

[43] M. Chodorow, E. L. Ginzton, W. W. Hansen, R. L. Kyhl, R. B. Neal, and W. K. H. Panofsky. Stanford high-energy linear electron accelerator (mark iii). *Review of Scientific Instruments*, 26(2):134–204, 1955.

[44] Mathematica 8, Wolfram Research, http://www.wolfram.com.

[45] V.A. Dolgashev, S.G. Tantawi, C.D. Nantista, Y. Higashi, and T. Higo. In *Proceedings of the 2004 Linear Accelerator Conference, Lübeck, Germany, 2004*, pages 766–768. DESY, Hamburg, 2004.

[46] V.A. Dolgashev, S.G. Tantawi, C.D. Nantista, Y. Higashi, and T. Higo. In *Proceedings of the 21st Particle Accelerator Conference, Knoxville, 2005*, pages 595–599. IEEE, Piscataway, NJ, 2005.

[47] V.A. Dolgashev, S.G. Tantawi, C.D. Nantista, Y. Higashi, and T. Higo. In *Proceedings of the 2007 Particle Accelerator Conference, Albuquerque, New Mexico*, pages 2430–2432, 2007.

[48] V.A. Dolgashev, S.G. Tantawi, Y. Higashi, and T. Higo. In *Proceedings of the 11th European Particle Accelerator Conference, Genoa, 2008*, pages 742–744. EPS-AG, Genoa, Italy, 2008.

[49] Valery Dolgashev. Recent studies of rf breakdown physics in normal conducting cavities. *AIP Conference Proceedings*, 1299(1):274–279, 2010.

[50] V.A. Dolgashev, S.G. Tantawi, Y. Higashi, and B. Spataro. Fr105. In *Proceedings of the 25th International Linear Accelerator Conference LINAC10, Tsukuba, Japan*, pages 1043–1047, 2010.

[51] Valery Dolgashev, Sami Tantawi, Yasuo Higashi, and Bruno Spataro. Geometric dependence of radio-frequency breakdown in normal conducting accelerating structures. *Applied Physics Letters*, 97(17):171501, 2010.

[52] V.A. Dolgashev, Z. Li, S.G. Tantawi, A.D. Yeremian, Y. Higashi, and B. Spataro. Mopc071. In *Proceedings of the 2011 International Particle Accelerator Conference, San Sebastian, Spain*, pages 241–243, 2011.

[53] V.A. Dolgashev, S.G. Tantawi, A.D. Yeremian, Y. Higashi, and B. Spataro. Thpea060. In *Proceedings of the 1st International Particle Accelerator Conference: IPAC'10, Kyoto, Japan*, 2010.

[54] Christopher Nantista, Sami Tantawi, and Valery Dolgashev. Low-field accelerator structure couplers and design techniques. *Phys. Rev. ST Accel. Beams*, 7:072001, Jul 2004.

[55] B. Spataro, D. Alesini, V. Chimenti, V. Dolgashev, Y. Higashi, M. Migliorati, A. Mostacci, R. Parodi, S.G. Tantawi, and A.D. Yeremian. High-power comparison among brazed, clamped and electroformed x-band cavities. *Nuclear Instruments and Methods in Physics Research Section A: Accelerators, Spectrometers, Detectors and Associated Equipment*, 657(1):88 – 93, 2011.

[56] L. C. Maier and J. C. Slater. Field strength measurements in resonant cavities. *Journal of Applied Physics*, 23(1):68–77, 1952.

[57] C.W. Steele. A nonresonant perturbation theory. *Microwave Theory and Techniques, IEEE Transactions on*, 14(2):70 – 74, feb 1966.

[58] K.B. Mallory and R.H. Miller. On nonresonant perturbation measurements (correspondence). *Microwave Theory and Techniques, IEEE Transactions on*, 14(2):99 – 100, feb 1966.

[59] David M. Pozar. *Microwave Engineering*. John Wiley & Sons, Inc, 2004.

[60] J. Haimson and B. Mecklenburg. Design features and initial rf performance of a gradient hardened 17 ghz tw linac structure. *AIP Conference Proceedings*, 1086(1):464–469, 2009.